Energy Flows in Deep Inelastic Scattering at HERA

Philip Bernard Kaziewicz
University College London

submitted to the
University of London
for the degree of
Doctor of Philosophy *in*
November 1995

Abstract

The transverse hadronic energy flow has been measured in DIS events detected in the 1993 and 1994 running periods at **ZEUS** on the **HERA** ring. The flow has been measured in Q^2 and y bins throughout the kinematic range available at **HERA** for diffractive and non-diffractive events. The flow measurement has been made using the **ZEUS** calorimeter with special attention paid to the very forward region of the component: this is the region which maps to the $\gamma^* p$ central region at low x and low Q^2, the region where an energy flow measurement is considered to be an unambiguous signal for the presence of BFKL dynamics.

In the measurement of these flows, a geometric unfolding procedure rather than a bin-to-bin correction has been developed. Various sources of experimental systematic error are discussed and their effects estimated. The level of transverse energy flow is found to be generally well described by the colour dipole model but not by the matrix element parton shower simulation. The shape of the transverse energy flow in the current jet region at low x and low Q^2 is not well described by any model used.

An unambiguous signal for BFKL dynamics has not been found in this analysis mainly as a result of uncertainties in parton fragmentation.

Acknowledgments

A big "ta" to the following people whose help at one time or another has been vital, directly or indirectly, to the production of this thesis:

T.Jones, T.Haas, M.Lancaster, R.Saunders, K.Long, J.Shulman, A.Doyle, N.Brook, J.and S.Butterworth, G.Feild, D.Miller, P.Newman, D.Kant, A.Wilson, T.Mavroidis, S.Robertson, W.Matthews, J.Ward, Sid, Tom, J.Tompkins, C.Williams, PPARC, the HERA staff, and many others who, if I've forgotten to mention them, my apologies.

An especially large "ta" to all the members of my family who've made all of this possible and to Vick who knows how much larger the thanks should be.

Phil Kaziewicz 17.11.95.

Contents

1 HERA and the ZEUS Detector **9**

1.1 Introduction 9

1.2 **HERA** 9

1.2.1 The injection system 10

1.2.2 Design parameters 11

1.3 **ZEUS** 11

1.3.1 The VXD 15

1.3.2 The CTD 15

1.3.3 The UCAL 17

1.3.4 The luminosity monitors 21

1.3.5 The SRTD 21

1.3.6 The C5 counter 22

1.3.7 The C4 collimator 22

1.3.8 The veto wall. 22

1.3.9 The **ZEUS** trigger system 22

2 Deep Inelastic Scattering at HERA **25**

2.1 The kinematics of the *ep* interaction 25

2.2 Triggering and event selection 31

2.2.1 The triggering of DIS events 31

2.2.2 Electron finding 32

2.2.3 Reconstructing the kinematic variables 34

2.2.4 Event preselection 35

2.2.5 DIS background rejection 36

3 QCD Models and Motivation 43
3.1 The quark-parton model 43
3.2 QCD corrections to the QPM 44
  3.2.1 The DGLAP picture 45
  3.2.2 The BFKL picture 47
3.3 The MEPS model 48
3.4 The colour dipole model 50
3.5 Hadronisation 51
3.6 Summary 52

4 Extraction of the Far-Forward $\mathbf{E}_T$ Flows 53
4.1 Introduction to energy flows 53
4.2 Principle of correcting detector observation 54
4.3 Measuring energy flow in the forward region. 55
  4.3.1 The observed energy flow. 55
4.4 Detector simulation at angles $\theta < 10^\circ$ 59
  4.4.1 Geometry description 60
  4.4.2 Interactions in dead material 63
  4.4.3 Response to particles outside the geometrical acceptance . . . 64
4.5 Corrections to the observed energy. 68
  4.5.1 Low energy background. 68
  4.5.2 Energy asymmetry. 70
  4.5.3 Cerenkov effect in wavelength shifter bars. 73
  4.5.4 Timing and imbalance cuts. 76
4.6 Geometric unfolding. 87
4.7 Systematic errors. 90
  4.7.1 Errors on the observed energies. 90
  4.7.2 Errors on the geometric unfolding. 91
  4.7.3 Energy correction factors. 93
4.8 Hadronic E_T flow measured in 1993 DIS data. 96

5 Energy flows throughout phase space. 99

5.1 Motivation and method 99

5.1.1 Systematic error checking 103

5.2 Diffractive events 104

5.2.1 Description 104

5.2.2 Diffractive energy flows 106

5.3 Results of the 1994 analysis 109

5.4 Comparison of 1993 and 1994 results 114

5.5 Energy flows versus x 115

6 Altering the conventional model 119

7 Conclusions 127

Chapter 1

HERA and the ZEUS Detector

1.1 Introduction

In 1991 **HERA**, the world's first electron-proton collider, was commissioned. The first *ep* interactions were observed by two detectors, **ZEUS** and **H1**, in May 1992. For a longer beam lifetime, electrons were replaced by positrons for most of the running period of 1994.

The analyses presented in this thesis have come from data collected by the **ZEUS** detector in the 1993 and 1994 running periods.

1.2 HERA

The construction of the *Hadron Elektron Ring Anlage* (**HERA**) began in April 1984 with work done by members of an international collaboration.

The site chosen was close to the *Deutsches Elektronen Synchrotron* (**DESY**) laboratory in Hamburg, Germany. By August 1987 the 6.34km beam tunnel had been finished and in the autumn of 1990, the electron ring, equipped with normal magnets, and the proton ring, equipped with superconducting magnets, were commissioned.

Machine tests continued with the separate acceleration of the electrons and protons until October 1991, when one bunch of electrons was collided with one bunch of protons and *ep* luminosity was achieved at a collider for the first time ever.

1.2.1 The injection system

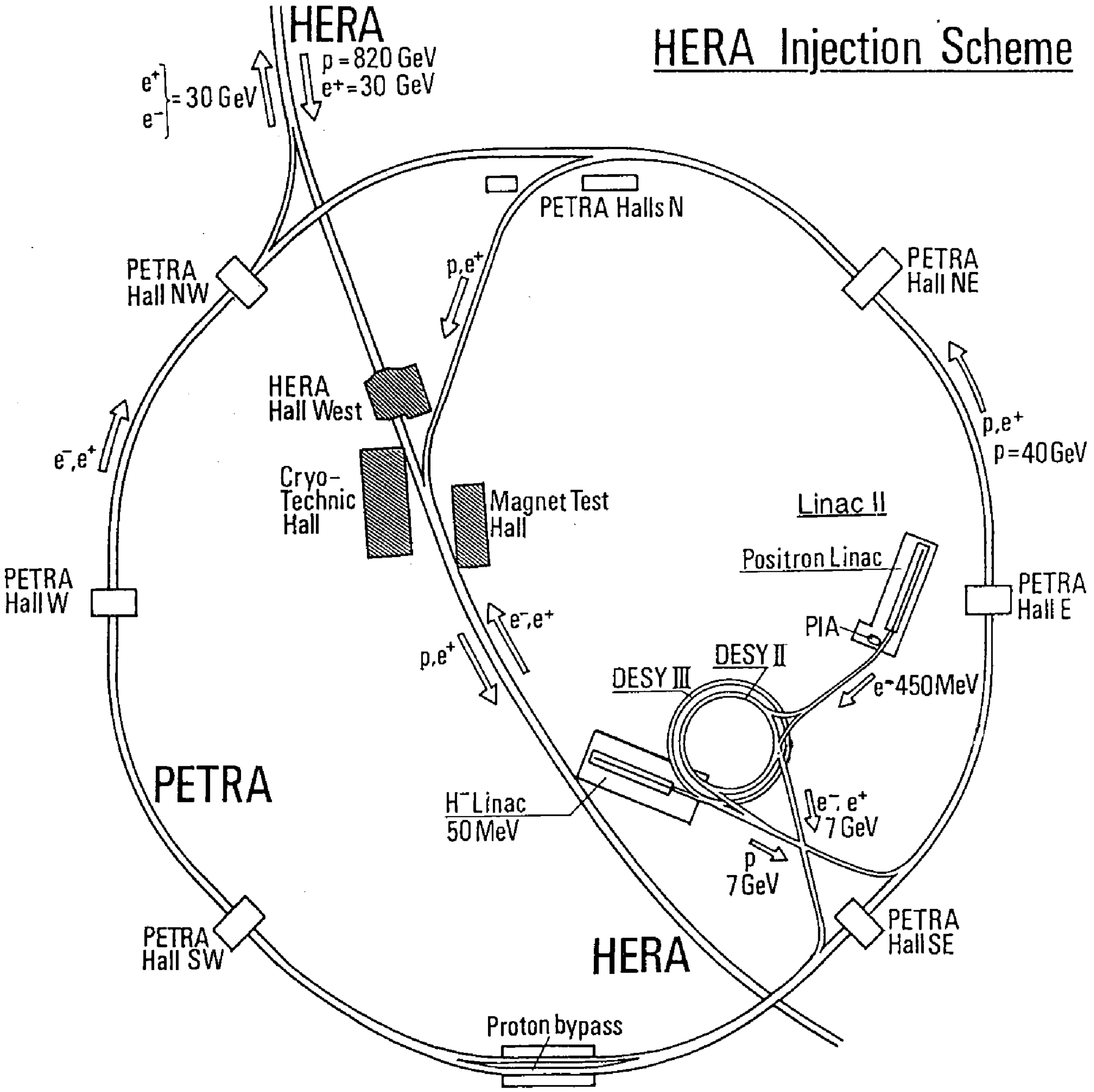

Figure 1.1: *The* **HERA** *injection system.*

Protons are accelerated as H^- ions in the proton linear accelerator (**LINAC**) to an energy of 50MeV. These are in turn accelerated to 7.5GeV by the **DESY-III** proton synchrotron and finally to 40GeV in the **PETRA** storage ring. At this energy, they are injected into **HERA** where they are accelerated to the design operating energy of 820GeV.

Electrons and positrons are accelerated by **LINACs I & II** to 220 and 450MeV respectively. They are transferred to **DESY-II** for further acceleration to 7.5GeV; then **PETRA** accelerates these to 12GeV at which point they are injected into **HERA**. The final stage of acceleration gives them an energy of 26.7GeV (1993) / 27.52GeV (1994).

1.2.2 Design parameters

Design value	electrons		protons
Injection energy	14GeV		40GeV
Beam energy	30GeV		820GeV
Particles per bunch	3.5×10^{10}		1.0×10^{11}
Number of bunches	210		210
Centre of mass energy		314GeV	
Current	60mA		160mA
Luminosity		$1.5 \times 10^{31}\text{cm}^{-2}\text{s}^{-1}$	
Bunch distance		28.8m	
Bunch crossing time		96ns	
Bunch length (1σ)	7.8mm		110-150mm
Bunch width	0.3mm		0.32mm
Beam height	0.04mm		0.1mm
Energy loss per revolution	70.38MeV		~ 0
Filling time	15min		20min

Eventually, using the designed specific luminosity, 100pb^{-1} per year is expected. In 1992, the **ZEUS** experiment collected 30nb^{-1}. This had increased to 540nb^{-1} in 1993 and by 1994 the integrated luminosity collected by **ZEUS** was 3.2pb^{-1}. For 1995 running, a luminosity 15pb^{-1} is expected.

During 1993 running, 84 paired bunches were filled for each beam. An additional 10 unpaired electron bunches and 6 unpaired proton bunches were filled to study backgrounds. Mean currents in both beams were typically around 10mA. In 1994, 153 bunches were paired with an additional 15 unpaired electron bunches and 17 unpaired proton bunches. Electron beam currents were $\approx$ 20mA and proton currents were often in excess of 40mA. [1, 2]

1.3 ZEUS

A letter of intent from the **ZEUS** collaboration [3] and the technical proposal for the **ZEUS** detector [4] were received by the directorate of **DESY** in 1985 and 1986 respectively. The detector was approved in November 1986 and **ZEUS** was allocated the south experimental hall of **HERA**.

There are over 500 physicists in the collaboration and about the same number of technical staff who come from over 50 institutes in 11 different countries: the UK, the USA, Canada, Germany, Israel, Italy, Japan, Poland, the Netherlands, Russia and Spain.

Final installation of the detector was completed in the autumn of 1991 following extensive testing of prototypes and the core components of **ZEUS** were operational for the first running period in 1992. Upgrades in the detector including the addition of new components have happened during each of the shutdown periods since then.

The **ZEUS** detector is a multi-purpose magnetic detector and in 1994 consisted of the active components listed in table 1.1 (refer also figure 1.2).

Detector Name	Acronym	Purpose	Detector Type
Vertex detector	VXD	Measurement of primary vertex position	Drift chamber filled with dimethylether
Central tracking detector	CTD	3D track reconstruction and $\frac{dE}{dx}$ measurement	Cylindrical drift chamber filled with Ar, CO_2, C_2H_6
Uranium calorimeter	(U)CAL F/B/RCAL	Energy measurement of leptons/hadrons	Depleted Uranium/ Plastic scintillator sampling calorimeter
Luminosity monitor	LUMI	Luminosity measurement and detection of photoproduction $e^{\pm}$ and radiative γ	Lead scintillator calorimeter with Si pads
Hadron-Electron separator	HES	Identify electrons within dense jets	Silicon pads
Backing calorimeter	BAC	Containment of particles escaping CAL. Shower tail catcher.	Fe yoke absorber with Al proportional tubes
Leading proton spectrometer	LPS	Detect remnant particles	6 Si detectors in roman pots
Veto wall	VETO	Veto interactions away from interaction region	Fe wall with 2 scintillator plates either side
Muon chambers	F/B/RMUO	Muon detection	Streamer tubes with planar drift chambers for FMUO
Transition radiation det.	TRD*	Particle identification	4 chambers, polypropylene fibres and Xe filled chambers
Small angle rear tracking detector	SRTD*	Improve pos^n measurement of charged particles entering RCAL	Scintillator strips in two planes
Forward/Rear tracking det.	F/RTD*	3D track reconstruction	3(FTD),1(RTD) drift chambers
The C5 counter	C5	Veto interactions away from interaction region	Si detector

Table 1.1: *List of the active* **ZEUS** *components in 1994. Refer to the text for detector performances. The status of the components marked "*" is also described.*

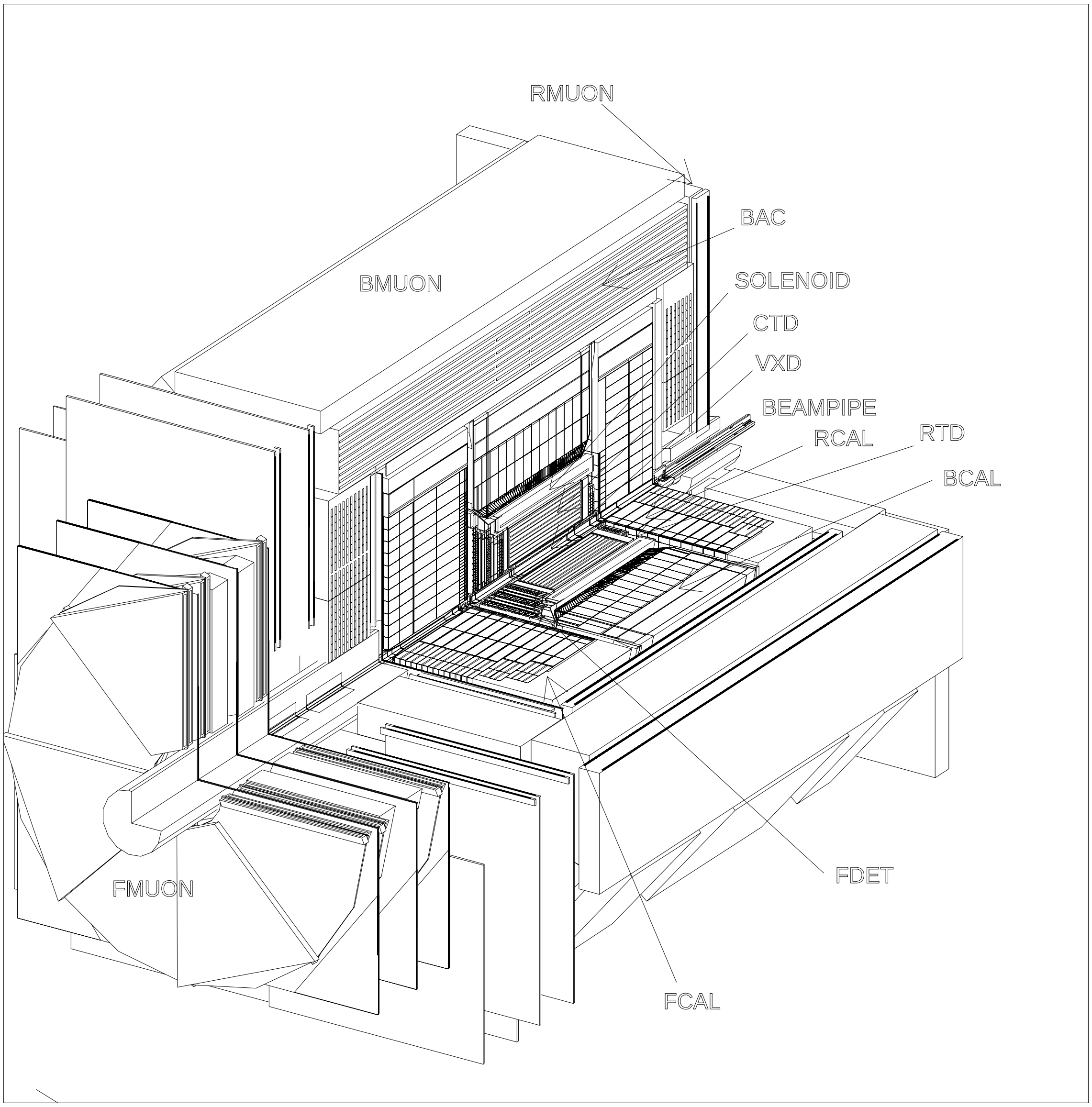

Figure 1.2: *View of* **ZEUS** *as shown by the detector simulation program* GEANT *[6] using* **ZEUS** *geometry description version* NUM12V1*.*

The RTD and SRTD were not operational in the 1993 running period. Implementation of the SRTD occurred in 1994.

The collective term for the FTD and the TRD components which are sandwiched together is the FDET. This has recently been fully installed and will be tracking particles during the 1995 running period but was not available for 1993 or 1994 data analyses.

Parts of the detector essential for the analyses presented in this thesis are described in more detail below. A more complete description of **ZEUS** is available in [5].

The coordinate system of **ZEUS** is defined as a right-handed system with the origin at the nominal interaction point (NIP) of **ZEUS**. The Z-axis points in the direction of the incoming proton, also known as the forward direction, i.e. towards the FCAL. The Y-axis points upwards and the X-axis towards the centre of the **HERA** ring. The proton beam polar angle is 0° and the electron beam polar angle is 180°.

1.3.1 The VXD

The vertex detector is a cylindrical drift chamber whose inner radius is 10.9cm and outer radius is 15.9cm surrounding the NIP of ZEUS. It is divided azimuthally into 120 drift cells, each cell therefore occupying 3° in azimuth.

Each cell contains 12 sense wires lined up between the inner and outer radii. These alternate between 13 field wires and 25 drift wires are placed on each side of this plane. All of the wires are parallel to the beam axis. The entire detector is filled with dimethylether (DME) gas to provide a slow drift velocity which gives accurate particle time resolution.

The VXD operates in a magnetic field of 1.43T which is provided by a superconducting SOLENOID. This sits radially between the CTD and the BCAL.

The VXD has a design performance of $\frac{\sigma(p)}{p} \approx 9 \times 10^{-4} p$ (when used in conjunction with the CTD) and an error on the primary vertex radius of $\sim 50\mu$m.

1.3.2 The CTD

The central tracking detector is the main component of **ZEUS** used for the tracking of charged particles. It surrounds the VXD and its outer radius is 85cm. It also operates in the 1.43T magnetic field provided by the superconducting SOLENOID. The polar angle coverage of the CTD is $15 < \theta < 164°$ (θ is the polar angle from the **ZEUS** NIP with respect to the proton beam direction).

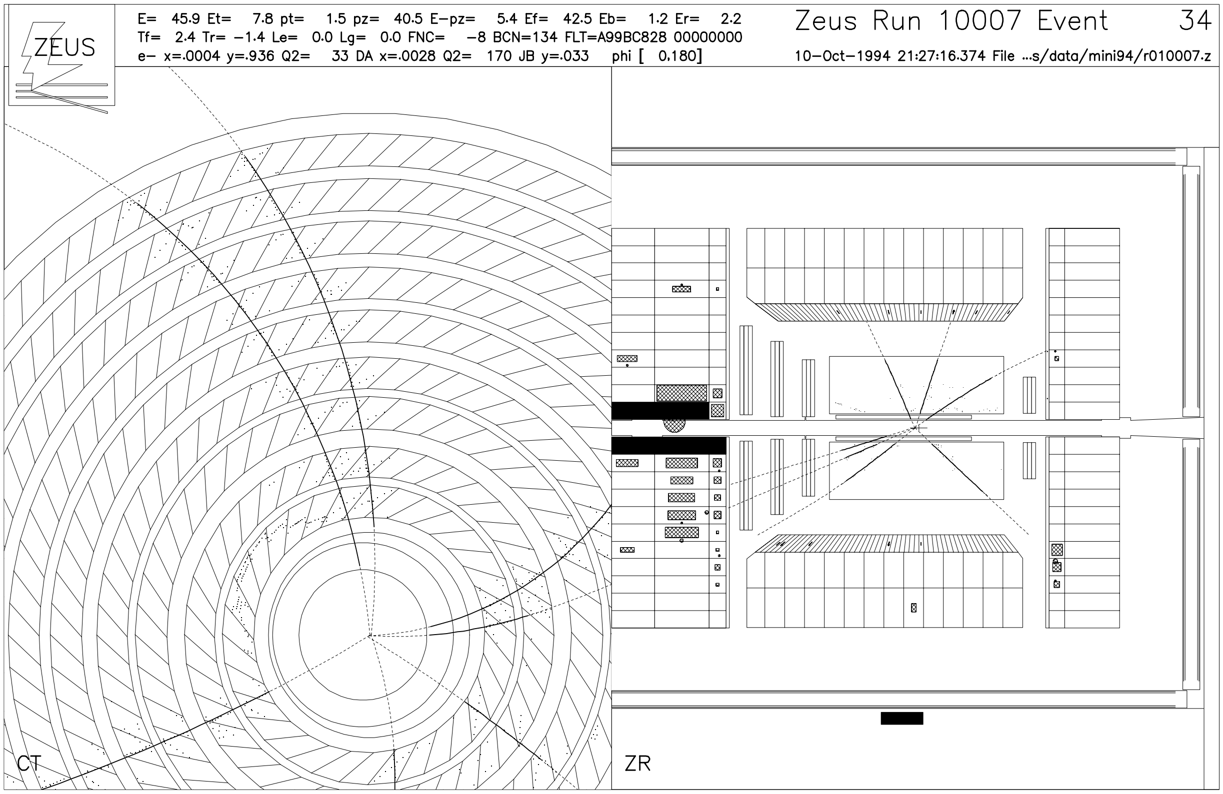

Figure 1.3: *Part of the* CTD *as drawn by the event-display program* LAZE *[9]. Each of the* CTD *cells contains eight sense wires evenly-spaced down the centre of the cell.*

The CTD consists of 4608 sense wires grouped into 8-wire cells. An azimuthal distribution of angled cells forms a *superlayer* and there are 9 such superlayers in the chamber as indicated in figure 1.3.

The sense wires in the CTD are kept at voltages between 1.26kV and 1.31kV. These wires are separated by ground wires (0V) and planes formed by the sense and ground wires alternate with planes formed by field-shaping wires which are maintained at voltages between 1.63 and 2.74kV [10].

Odd-numbered superlayers are known as *axial* superlayers and have their wires parallel to the CTD axis. The even-numbered superlayers, known as *stereo* superlayers, have their wires at a small angle ($\sim 5°$) to the chamber axis.

Two methods are used to determine the Z-position of a track element. The Z-by-timing method exploits the time difference of a signal arriving at the two ends of a wire [13] whereas the Z-by-stereo method takes advantage of the even-numbered superlayers. Signals on axial superlayers, when projected onto the end of the chamber, can be aligned to form a track. Hits from the same track in the stereo layers, however, are rotated due to the stereo angle. An extrapolation of this projection along the Z of the chamber until the track matches that from an axial layer gives the Z-position of that track [7]. The Z-by-timing method alone achieves a Z position resolution of 4.5cm but is by far the faster system (several nanoseconds versus several hundred milliseconds). The Z-by-stereo method achieves Z position resolution of $\approx$ 2mm.

A $50\% Ar, 50\% C_2H_6$ mix was the designed gas for the CTD. However, mainly for safety reasons, the mixture used to fill the CTD for 1993 and 1994 running was $85\% Ar, 5\% C_2H_6, 10\% CO_2$ [11]. A slight increase in the proportion of C_2H_6 to CO_2 has been made for the 1995 run period.

In 1994 running, the CTD had achieved a tracking resolution of 180μm and $\frac{\sigma(p_T^2)}{p_T^2} \approx (0.005)^2 p_T^2 \pm (0.016)^2$ [12].

1.3.3 The UCAL

The most important part of **ZEUS** for the analyses to be presented in this thesis is the uranium calorimeter. The calorimeter contains electromagnetic and hadronic calorimeter sections. A large effort was made to make the energy resolution as good as possible. It was seen that such a calorimeter must have equal responses to both the electromagnetic and hadronic deposits ($e/h = 1$, where e and h are the responses for electrons and hadrons). Such a calorimeter is said to be *compensating*.

Electromagnetic showers are produced by incident electrons, positrons and photons and their nature is well-understood [14]. Hadronic showers, on the other hand, cannot be analytically described. They can contain both hadronic *and* electromagnetic components even though the showers are hadron-initiated. The proportion of these components varies from one shower to another even if the incident energy is the same.

The **ZEUS** collaboration decided upon a calorimeter constructed using depleted uranium ^{238}U as an absorber [15]. A plastic scintillator was chosen as the readout material and by varying the relative thickness of alternating layers of absorber and scintillator (the "sandwich"), full compensation can be achieved over a very wide range of energies [5].

Construction

The UCAL is divided into three parts corresponding to different ranges of polar angle coverage: the forward calorimeter (FCAL), the barrel calorimeter (BCAL) and the rear calorimeter (RCAL).

The energy which the calorimeter is required to absorb is a function of the polar angle. It ranges from approximately the proton energy (820GeV) in the forward direction to the electron energy (27GeV) in the rear. The mean particle energies are somewhat lower, however, and a simulation of 1000 typical deep inelastic scattering events using the physics generator ARIADNE and detector simulator GEANT (both described in later chapters) reveals the particle energy spectrum of figure 1.4.

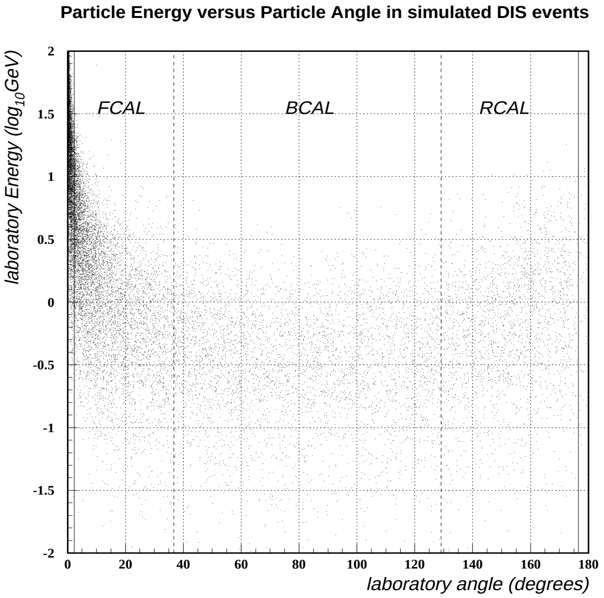

Figure 1.4: *Monte Carlo simulation of energy deposits in the* **ZEUS** *calorimeter for 1000 DIS events.*

Because of this angular dependence, the FCAL has a depth of 7 absorption lengths, λ, the BCAL has a depth of 5λ and the RCAL a depth of 4λ. Much higher jet energies can be contained with the surrounding BAC.

The polar angle coverage of the FCAL is $2.3 < \theta < 36.7^\circ$. It is divided into 23 vertical modules numbered with increasing X. Each module has a width of 20cm. Each of these modules is in turn segmented into 20 x 20cm towers numbered with increasing Y [51]. One module is divided up into three sections in Z, an inner electromagnetic part (FEMC) and two hadronic parts (FHAC1 and FHAC2). The FEMC part is further subdivided into four 20 x 5cm sections. Each of the sections is called a calorimeter *cell.* (The central module has a 20 x 20cm hole in the middle to accomodate the **HERA** beam-pipe.)

The polar angle coverage of the RCAL is $129.1 < \theta < 176.5^\circ$. The structure of the RCAL is very similar to that of the FCAL except that REMC is subdivided into two 20 x 10cm cells instead of four. The RCAL has only one hadronic section.

The BCAL covers the angles between the FCAL and the RCAL. It contains 32 wedge-shaped modules and, in a similar way to the FCAL, has an electromagnetic part, BEMC, and two hadronic parts, BHAC1 and BHAC2. Each of these modules has 14 towers with the EMC part containing four cells per tower.

All of the calorimeter towers are made with a sandwich of alternate layers of 3.3mm-thick depleted uranium and 2.6mm-thick plastic scintillator. This thickness provides an e/h ratio of 1.00 ± 0.02 in the energy range 10 to 100GeV [16, 17].

Charged particles traversing the scintillator produce light which travels by internal reflection to wavelength shifters. The light is converted to a longer wavelength by wavelength shifters and travels to the photomultipliers (PMTs) at the back of the tower. An electrical signal is produced by these and passed out of the detector. There are two PMTs for each cell (one at each side in X) as indicated in figure 1.5. This provides some redundancy and an indication of the X-position of a deposit.

Performance

To take advantage of the high resolution achievable by the calorimeter, an accurate calibration must be performed. An ongoing procedure is the determination of the calibration for all of the calorimeter channels.

The principal method for this is the use of the naturally-occuring radiation from the depleted uranium (energy $\approx$ 2.3MeV). In combination with this, a point-like ^{60}Co source can be moved parallel to each scintillator's plate position. The variation of calorimeter response to this is stable at the level of a few percent [18].

Modules from the RCAL and FCAL have been calibrated at **CERN** using test-beams with various particles at known energies. The results from these tests show that there is a linear response of the calorimeter to incident energy at the level of $\sim 1\%$. The energy resolution is found to be $17.5\%(\pm 1\%)/\sqrt{E}$ for electrons and $35\%(\pm 2\%)/\sqrt{E}$ for hadrons and the time resolution better than 1ns for $E > 15$GeV. At lower energies, this resolution is somewhat degraded by noise [16].

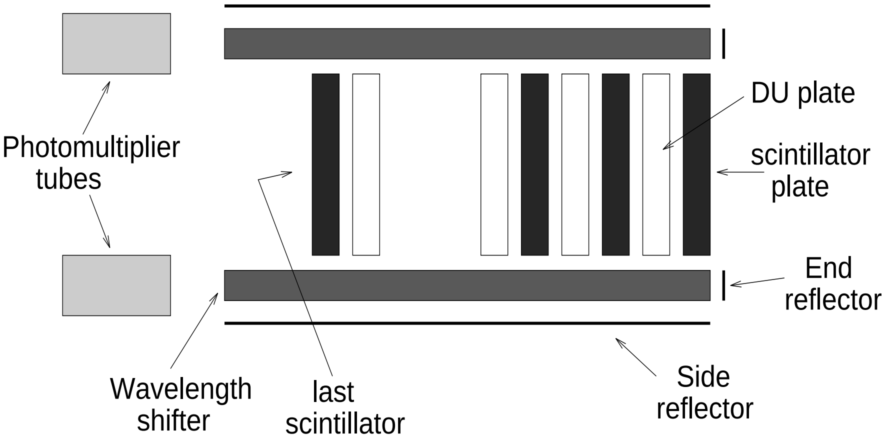

Figure 1.5: *Schematic top-view of an* FCAL *tower. Particles are incident on the right-hand face.*

1.3.4 The luminosity monitors

Two small lead-scintillator calorimeters are placed at -34.7m (LUMI-e) and -106.0m (LUMI-γ) from the NIP. These form the luminosity monitors which serve two important roles.

Firstly, the luminosity provided by **HERA** is measured based upon the Bethe-Heitler process $ep \rightarrow e'p\gamma$ where a photon is emitted by the electron at very low angles [19].

The cross-section for this process is high and very well known. A signal detected in either of the luminosity monitors whose energy sum is that of the incoming electron is a detection of this process.

Secondly, the two monitors serve as tagging devices for collisions occuring at very low Q^2 (photoproduction processes) and for initial state bremsstrahlung in neutral current deep inelastic scattering events (ISR-DIS).

In tagged photoproduction, a signal is encountered in the LUMI-e monitor with no corresponding signal in the LUMI-γ detector. In ISR-DIS events, no signal is encountered in the LUMI-e monitor but the emitted photon is seen in the LUMI-γ detector.

Both of the LUMI detectors have been designed with an energy measurement resolution of $0.16/\sqrt{E}$.

1.3.5 The SRTD

The small angle rear tracking detector (SRTD) aims to improve the calorimeter energy resolution for single particles and jets by recognising particles showering in the dead material in front of the RCAL and correcting for the energy lost.

The SRTD covers an area of 68cm × 68cm around the beam-pipe (minus the beam pipe hole) and sits at $Z = -1.46$m.

It consists of two planes of scintillator strips, each plane sectioned into four 24cm × 44cm pieces. The strips have a 1cm width and are arranged either in the X or the Y directions, the X and Y-strips being alternately positioned along the Z direction. There are 272 strips in total which are read out via light fibres and photomultipliers. Each of the planes is 0.5cm thick and they are separated by a support plane which reduces cross-talk.

The SRTD can achieve a position resolution of 5mm in X and Y.

1.3.6 The C5 counter

The C5 counter, so called because it is attached to **HERA** collimator number 5, is a lead plate sandwiched between two scintillator plates within the beam-pipe. It is placed perpendicular to the beams at $Z = -315$cm with an inner radius of which varies from 12mm to 30mm depending on whether the collimator is "closed" or "open".

The counter measures the rate of interactions produced by the beam, gives information about the beam shapes and helps to reduce the proton-beam-gas background. It has a time resolution of $\sim$ 1ns.

1.3.7 The C4 collimator

Collimators and absorbers are used to reduce the synchrotron radiation emitted from the beams. This protects the central parts of the detector from high radiation rates.

Although these devices are not detectors, **HERA** collimator number 4 is found to be especially important in the analyses presented in this thesis. Since this collimator sits in the beam-pipe hole of the FCAL at a Z of 220cm, it is found that forward-going particles can shower and scatter from it. This scattered energy can often be detected by the calorimeter.

A much more thorough description of the C4 collimator is contained in section 4.4.1.

1.3.8 The veto wall.

The veto wall is an 87cm-thick Fe wall placed around the beam-pipe at $Z = -7.5$m. Two planes of scintillator counters are attached to either side. The veto wall detects and absorbs particles from proton-beam-gas collisions and veto-triggers such an event if hits are detected on both sides of the wall.

1.3.9 The ZEUS trigger system

There exist two major constraints on experiments using the **HERA** beams. Firstly, the beam-crossing interval is only 96ns. Secondly, there is a very high background to signals which is associated with beam particles colliding with residual gas in the beam-pipes. The combination of effects leads to a signal in the region of 100kHz, of which only $\sim 2-3$Hz are interesting *ep* events.

A multi-layered trigger system at **ZEUS** helps to remove this background whilst keeping *ep* events [20].

- The first-level trigger (FLT) reduces the signal to $\sim$ 1kHz. Since most components cannot make a useful trigger decision in the 96ns beam crossing interval, data from components is "pipelined". The CAL, for example, uses a switched capacitor array to pipeline its (analogue) data whereas the CTD uses a digital pipeline to store its hit information which is already digitised. A "sub-trigger" decision can be made by each component participating in the FLT within 5μs (96ns$\times$52, the beam crossing interval times the pipeline length). Such a decision from each of the components is passed to the global first level trigger (GFLT) where an overall decision is made. An example is the use of the CTD to pattern-recognise whether or not an event has produced a primary vertex in the expected region. If such a vertex has been found then the CAL can be used to add an $|E_T|$ cut. Further clustering information from the analogue calorimeter can be extracted. The GFLT then decides which events are likely to be *ep* interactions. At the end of this stage, approximately 98% of the events passed are background events.

- The second-level trigger (SLT) reduces the input from the FLT ($\sim$ 1kHz) to $\sim$ 100Hz and has 1ms to make a decision. As with the FLT, sub-triggers from components are passed to the global trigger (GSLT) where an event decision is made. Since the time allowed for the decision to be made is much longer than in the FLT, charged particle tracking, better vertex position determination, muon, jet and scattered electron finding is used in the event decision.

- The GSLT sends events which have passed its criteria to the event builder (EVB). This collects all the data from the various components for these events, merges the data into a ZEBRA bank [21] , reformats this according to the ADAMO package [22] and sends it to the next trigger stage. (ZEBRA and ADAMO are software packages which manage data structures.)

- The third level trigger (TLT) is a farm of very fast processors which view the event as a whole. The TLT can use more elaborate vertex fitting and track finding algorithms than there is time for at the SLT stage. The final rate after the decision of the TLT is $\sim$ 5Hz. After a positive decision, all the data from an event is put on to the mass storage devices.

Once the events have been passed from the TLT, software is run which fully reconstructs the events using information from all available components. The subset of these events which correspond to neutral current deep inelastic scattering events, those events useful for the analyses presented in this thesis, can then be selected using other criteria described in the next chapter.

Chapter 2

Deep Inelastic Scattering at HERA

2.1 The kinematics of the *ep* interaction

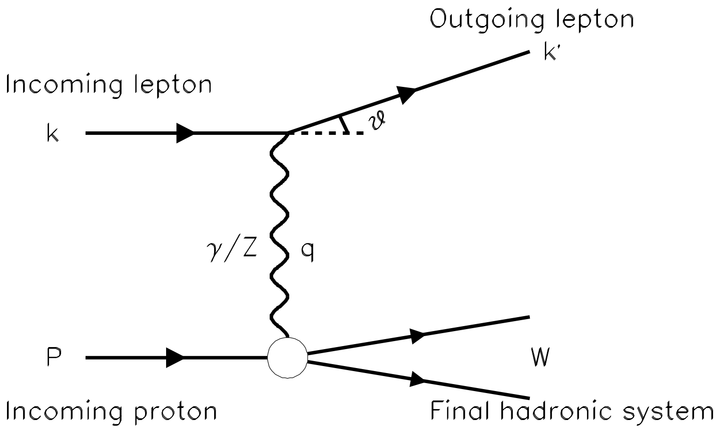

Figure 2.1: *Inelastic neutral current ep scattering*

Although there are many interesting areas of physics at **HERA**, only that of deep inelastic scattering (DIS) will be covered in this thesis. Deep inelastic scattering involves a high momentum transfer ($> 1\text{GeV}^2$) from the lepton to the proton. This momentum is carried by an exchanged virtual boson.

The analysis contained in this thesis is not concerned with charged-current (CC) DIS interactions where the incoming lepton becomes a scattered neutrino as a result of the exchange of a virtual $W^{\pm}$ boson.

All other DIS interactions are of the neutral current (NC) type where the type of the scattered lepton is identical to that of the incoming lepton. Such NC interactions are the result of the exchange of a virtual photon (γ^{*}) or virtual Z^{0} boson between the lepton and the participating parton within the proton.

The neutral current scattering process $e(k) + p(P) \rightarrow e(k') + \mathit{anything}$ is represented to first order by figure 2.1. This is the representation given by the quark-parton model (QPM) and does not include any quantum-chromodynamic corrections. These corrections are discussed in the next chapter.

Since the final state of a NC interaction is not affected by the type of exchanged boson, this text will refer to the vitual photon as meaning either the γ^{*} or Z^{0}. Few events initiated by a Z^{0} exchange are expected in the data sample used in the analyses presented in this thesis because of the suppression factor associated with the propogator $(\frac{1}{q^2+M_Z^2})$ [42].

During 1993 running, **ZEUS** collected $538\mathrm{nb}^{-1}$ of $e^{-}p$ collisions of those which **HERA** provided and a further $287\mathrm{nb}^{-1}$ of $e^{-}p$ collisions during the first month of running in 1994. For the remainder of the 1994 run period, **ZEUS** collected $2.9\mathrm{pb}^{-1}$ of $e^{+}p$ collisions [1].

The change in lepton type does not affect the final-state of the NC DIS process. Henceforth, the incoming and scattered lepton will be referred to as the incoming and scattered electron.

In the following analyses, $180\mathrm{nb}^{-1}$ of the DIS events seen in 1993 and $2.0\mathrm{pb}^{-1}$ of the $e^{+}p$ DIS events in 1994 have been used. Not all the data has been used since, as will be seen later, the measurement of energy flows is dominated by the systematic (as opposed to the statistical) errors.

The kinematics of the DIS process is described by the following variables:

- s, the centre of mass energy squared.

$$s = (k + P)^2 = (E_e + E_p)^2 - (\underline{p}_e + \underline{p}_p)^2 \approx 4E_eE_p \qquad (2.1)$$

  where E_e,E_p and $\underline{p}_e$,$\underline{p}_p$ are the energies and three momenta of the incoming electron and proton respectively when their rest masses are ignored.

- Q^2, the negative of the squared 4-momentum transfer carried by the virtual photon.

  $$Q^2 = -q^2 = -(k-k')^2 = -(E_e - E'_e)^2 + (\underline{p}_e - \underline{p}'_e)^2 = 4E_eE'_e \sin^2(\frac{\theta}{2}) \tag{2.2}$$

  ($\theta_e = 180^\circ - \theta$ in **ZEUS** coordinates.)

- $x(0 \leq x \leq 1)$, the Bjorken scale variable.

  $$x = \frac{Q^2}{2q.P} \tag{2.3}$$

  In the QPM, x can be interpreted as the fraction of the proton's momentum carried by the struck parton.

- W^2, the square of the centre-of-mass energy of the $\gamma^* p$ system $\equiv$ the square of the hadronic final state's invariant mass.

  $$W^2 = (P+q)^2 = P^2 + q^2 + 2q.P = M^2 - Q^2 + \frac{Q^2}{x} \approx Q^2(\frac{1-x}{x}) \approx \frac{Q^2}{x} \tag{2.4}$$

  where M is the rest mass of the proton. The last approximation is valid at low x.

- $y(0 \leq y \leq 1)$, the variable which describes the energy transfer to the hadronic final state in the proton rest system.

  $$y = \frac{q.P}{k.P} = \frac{Q^2}{2x(k.P)} \tag{2.5}$$

Now since

$$2k.P = (k+P)^2 - k^2 - P^2 = s - m_e^2 - M^2 \tag{2.6}$$

where m_e is the rest mass of the lepton, Q^2, s, x and y are related by the equation

$$Q^2 \approx sxy \tag{2.7}$$

To a very good approximation at **HERA** the proton rest mass can be neglected, since the hadronic masses W^2 involved are much bigger than the proton mass. Since the beam energies of the electron and proton are known, only two of the kinematic variables are independent.

An additional variable to consider is θ_h. In the QPM approximation, θ_h is the scattering angle of the struck parton. It can be found using the above variables [23] as follows:

$$\cos\theta_h = \left(\frac{Q^2(1-y) - 4y^2E_e^2}{Q^2(1-y) + 4y^2E_e^2}\right) \tag{2.8}$$

Also, it is useful to introduce the quantity *rapidity* which is defined for each particle by its energy and momentum components:

$$\eta = \frac{1}{2}\ln\left(\frac{E + p_{para}}{E - p_{para}}\right) = \ln\left(\frac{E + p_{para}}{p_{perp}^2 + M^2}\right) \tag{2.9}$$

where M is the rest mass of the particle.

Rapidity has a useful quality: when a longitudinal boost from the laboratory frame to another frame is performed upon particles, their relative rapidities remain the same. It is Lorentz invariant.

Ignoring the masses of the particles, rapidity approximates to the quantity *pseudorapidity* which is related to the polar angle of the particle by

$$\eta \approx \ln\left(\frac{2p_{para}}{p_{perp}}\right) = -\ln\tan\left(\frac{\theta}{2}\right) \tag{2.10}$$

At **ZEUS**, $\theta = 0$ is in the direction of the FCAL from the nominal interaction point (NIP), the event's primary vertex, when the trajectory of the incident proton is extrapolated. With this definition, the following table can be constructed:

θ_h	η	Where in **ZEUS**?
0	$+\infty$	incident proton direction
180	$-\infty$	incident electron direction
90	0	perpendicular to the colliding beams
2.3	3.9	bottom face of FCAL

At **HERA**, the incoming electron energy in 1994, E_e, was 27.52GeV and the incoming proton energy, E_p, was 819.9GeV. From the above equations, $s = 90264.5$ GeV^2($\sqrt{s} = 300$GeV). Using these numbers, it is possible to construct the following table which gives the scattering angles and energies when collisions occur in various parts of the kinematic phase-space available at **HERA**. (All angles are quoted relative to the proton direction). Note the proximity of the electron scattering angle to that of the struck quark jet at low x and Q^2.

Position in phase-space	Q^2	x	y	W	E'_e	θ_e	θ_h
Low-x, low-Q^2	6	9.5E-5	0.7	251	8.3	179.2	176.0
High-x, low-Q^2	6	1.7E-3	0.04	60	26.4	179.8	85.1
Low-x, medium-Q^2	40	6.3E-4	0.7	251	8.3	174.9	169.7
High-x, medium-Q^2	40	1.1E-2	0.04	60	26.4	178.4	39.1
Low-x, high-Q^2	500	7.9E-3	0.7	250	8.3	108.7	144.7
High-x, high-Q^2	500	1.4E-1	0.04	58	26.4	160.1	11.5

An example of a NC DIS event which has been reconstructed in **ZEUS** by the software package ZEPHYR [31] is shown in figure 2.1.

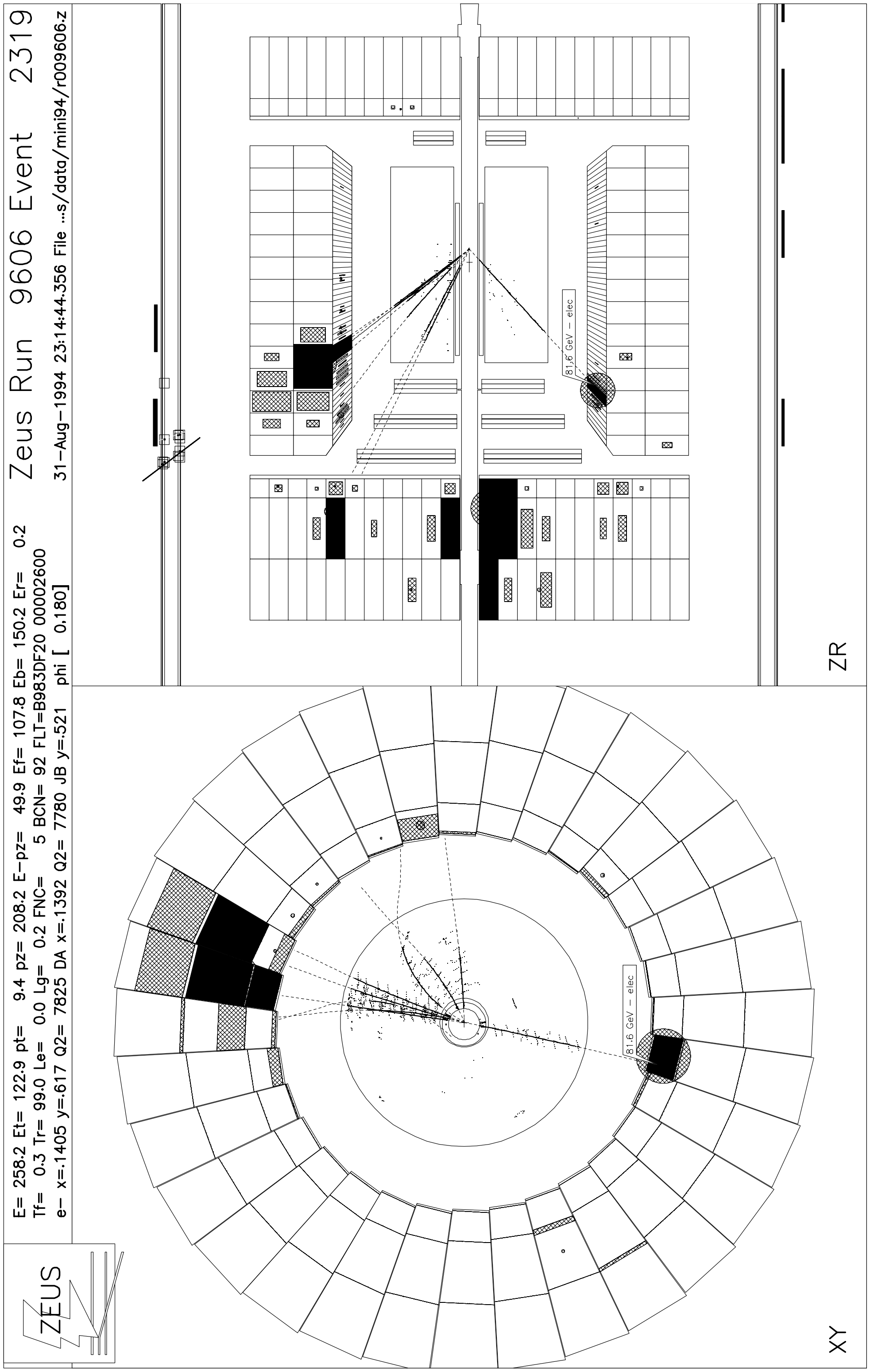

Figure 2.2: *A high-Q^2 NC-DIS event as seen in* **ZEUS**. *The scattered electron has been labelled.*

2.2 Triggering and event selection

2.2.1 The triggering of DIS events

The trigger system described in the previous chapter reduces beam-gas backgrounds considerably. From the set of events which this trigger system provides, a subset, corresponding to neutral current DIS events, is required.

The obvious signatures for NC-DIS events are as follows:

1. An isolated electromagnetic cluster is deposited in the calorimeter (possibly matched with an isolated track originating from the interaction region). The basic trigger criterion is therefore an isolated energy deposit (i.e. not within a jet) in the EMC section of the BCAL or RCAL. An isolated deposit in the EMC section of the FCAL only is not considered to be sufficient. This is the first indication of the presence of a scattered electron. The energy of this cluster must be above some threshold to reduce the background from calorimeter noise and photons produced from non-DIS events. The thresholds chosen are $E(BCAL)_{EMC} > 5\text{GeV}$ or $E(RCAL)_{EMC} > 2\text{GeV}$.

2. Studies have shown that the proportion of beam-gas events within a sample can be significantly reduced by employing a calorimeter timing cut [20]. This calorimeter time is the average time for the first energy deposits to signal in the calorimeter after the interaction has occured. An event is flagged as *ep* if $|\text{RCAL time}| < 8\text{ns}$ and $|\text{FCAL time} - \text{RCAL time}| < 12\text{ns}$ (see figure 2.3). A purer sample of events is selected with a tightening of this cut. DIS events are selected only if the latter time difference is $< 8\text{ns}$.

3. The transverse momentum in a neutral current DIS event must be balanced. From conservation of momentum, the k_T of the struck quark jet(s) must equal the k_T of the scattered electron. In a charged current event, the scattered lepton is a neutrino which is not seen in the detector. Detected transverse momentum is therefore not balanced. Neutral current DIS events are triggered if missing $k_T < 9\text{GeV}$.

4. The quantity $E - p_z$, also known as δ, is an important kinematic variable in the recognition of NC-DIS events. It is defined in the next section. For triggering

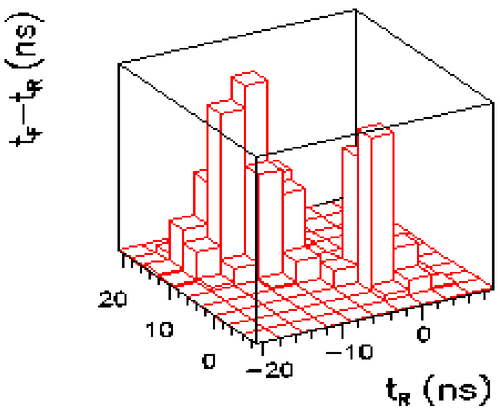

Figure 2.3: *Calorimeter times for beam-gas background events (larger spike) and ep physics events (smaller spike to the right).*

purposes, the TLT requires a $\delta > 20$GeV to qualify an event as NC-DIS. A tighter cut is made later to provide an even purer NC-DIS sample.

Monte Carlo studies have shown that the **ZEUS** trigger system, whilst reducing the number of input events by $10^4 - 10^5$ times, accepts 97% of DIS events.

2.2.2 Electron finding

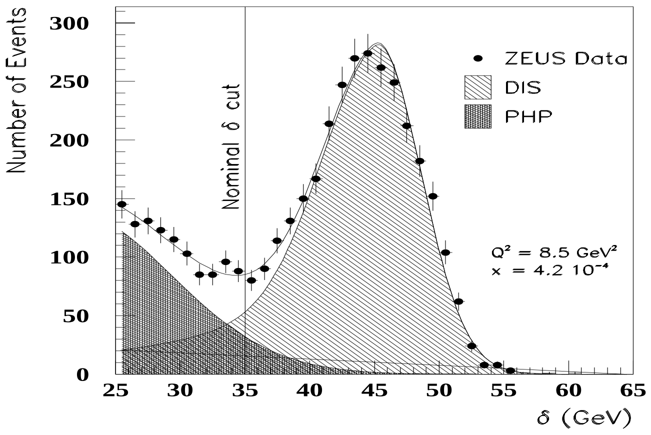

Figure 2.4: *The δ distribution of DIS and photoproduction events. Beam-gas background events (not shown) are contained in a large peak towards $\delta = 0$.*

Finding the scattered electron and measuring its energy is necessary for recognizing and selecting NC DIS events.

Presently, there are 4 electron finders used at **ZEUS**. All four are used in the setting of DST bits, described in section 2.2.4, but only two are used in this analysis. The preferred finder in 1994, due to the purity with which electrons are found, is the algorithm SINISTRA [24]. This finder is based on a cone-algorithm which groups candidate calorimeter cells into clusters. It subsequently uses neural network-based pattern recognition techniques to select the most probable scattered electron cluster.

The other electron finder used, and the main one used in the 1993 analysis, is an algorithm which groups electromagnetic deposits in the calorimeter into islands. Islands are energy-weighted surfaces derived from isolated groups of electromagnetic cells. This electron finder is called EEXOTIC [26].

The main and most important source of background to DIS events is that of photoproduction where, in general, the scattered electron disappears through the rear beam-hole and another particle is identified in its stead [27].

A useful experimental variable, δ, is defined as

$$\delta = E - p_z = \sum_i (E_i - p_{zi}) \tag{2.11}$$

which is calculated with respect to the incoming electron direction. The summation is over all calorimeter cells and includes the energy deposit of the "found" electron. For fully-contained events, energy-momentum conservation requires that $\delta = 2E_e \approx 54\text{GeV}$. The loss of particles through the forward beam-hole has only a small effect on δ but the loss of the scattered electron reduces δ significantly. This can occur if the scattered electron continues down the RCAL beam-pipe without interacting with the calorimeter. Additionally, the electron finder may not be able to recognise the calorimeter cluster which correctly contains the scattered electron.

The value of δ cannot be significantly higher than $2E_e$ for genuine ep events (plus a small amount ($\sim$ 3GeV) to account for the measurement error caused by the finite resolution of the calorimeter). Higher values are indicative of events triggered by cosmic muons passing through the detector. The 1993 DIS sample collected by **ZEUS** for the structure function F_2 analysis [38] has a δ distribution which is shown in figure 2.4.

At high Q^2, the scattered electron has a high energy and angle. It is likely to have caused an isolated signal in the BCAL and may have made a track in the CTD. Such electrons are easily found by the finding algorithms. At low Q^2 and low x, the less-energetic scattered electron can overlap with deposits made by the struck-quark current jet. It is much more difficult to isolate these electrons and the purity of the algorithms diminishes. This reduces the acceptance of DIS events, defined as those events found in a kinematic region divided by those produced in that region. The lower the acceptance of a region, the greater the chance of a quantity derived for that region being inaccurate.

2.2.3 Reconstructing the kinematic variables

To obtain the kinematics of an event, four parameters can be used: the scattered electron energy, E'_e, the scattered electron angle, θ (as defined in equation 2.2), the QPM struck quark angle, θ_h and the energy contained in the jet formed by the struck quark, F.

However, only two of the kinematic variables are independent. Therefore, the experimental determination of them can in principle be derived from two of these parameters. There are many ways to combine the two parameters to reproduce the kinematic variables. Those methods used in this analysis are described here and are derived fully in [23].

- Using the electron variables:

$$\begin{aligned} y_{el} &= 1 - \frac{E'_e}{2E_e}(1-\cos\theta), && (2.12)\\ Q^2_{el} &= 2E_eE'_e(1+\cos\theta) \qquad \text{and} && (2.13)\\ x_{el} &= \frac{E_e}{E_p}\left(\frac{E'_e(1+\cos\theta)}{2E_e - E'_e(1-\cos\theta)}\right) && (2.14)\end{aligned}$$

- Using the Jaquet-Blondel method:

$$\begin{aligned} y_{JB} &= \frac{\sum_i(E_i - p_{zi})}{2E_e}, && (2.15)\\ Q^2_{JB} &= \frac{(\sum_i p_{xi})^2 + (\sum_i p_{yi})^2}{1-y_{JB}} \qquad \text{and} && (2.16)\\ x_{JB} &= \frac{Q^2_{JB}}{s.y_{JB}} && (2.17)\end{aligned}$$

where the sum runs over all calorimeter cells.

- Using the "double-angle" method:

$$y_{DA} = \frac{\sin\theta(1-\cos\theta_h)}{\sin\theta_h+\sin\theta-\sin(\theta+\theta_h)}, \tag{2.18}$$

$$Q^2_{DA} = 4E_e^2\left(\frac{\sin\theta_h(1+\cos\theta)}{\sin\theta_h+\sin\theta-\sin(\theta+\theta_h)}\right) \quad \text{and} \tag{2.19}$$

$$x_{DA} = \frac{E_e}{E_p}\left(\frac{\sin\theta_h+\sin\theta+\sin(\theta+\theta_h)}{\sin\theta_h+\sin\theta-\sin(\theta+\theta_h)}\right) \tag{2.20}$$

Kinematic resolution

Using the components installed for the 1993 analysis, the best method throughout phase-space for reconstructing the kinematic variables is the double-angle method [23]. With the addition of the SRTD, the 1994 analysis uses the electron method for all events with $x_{el} < 10^{-3}$. This mixed method of reconstruction will be denoted $x_{mix}, Q^2_{mix}, y_{mix}$. Figure 2.6 shows the resolution of both reconstruction methods as determined from a Monte Carlo simulation. The details of the simulation are discussed in the following chapters.

2.2.4 Event preselection

Before the main body of an event's data is loaded onto an analysis machine, the event header is scanned. To save a great deal of time, a scheme has been developed which allows a user to select whether or not an event is used, prior to its loading. Using information collected online, certain flags are set or reset in the event header which depend on particular conditions found in the event. The flags are known as the DST (data summary tape) selection bits.

For 1993 data, only events which had bit 14 set were analysed further. Bit 14 is defined in 1993 data as the so-called "JDIS" or "golden" DIS bit. This is set only when all of the following criteria are satisfied:

- The δ of the event is greater than 35GeV
- Either EEXOTIC or SINISTRA finds a scattered electron with $E'_e > 5$GeV
- The electron is found outside the "Box-cut" (see section 2.2.5) of 16cm. The "Box-cut" refers to a square on the face of the FCAL centred at the beam-pipe centre. Since the purity and efficiency of the electron finders are very low

within this square, events whose only electron is "found" in this region are removed.

- $y_{JB} > 0.02$ to ensure that the event has deposited sufficient energy in **ZEUS** to reconstruct the event
- The cosmic muon rejection routine, based on event topology (see also section 2.2.5, does not disallow the event
- The beam-halo rejection routine, also based on event topology, does not disallow the event
- The routine, which removes events triggered by random calorimeter PMT noise (sparks), does not disallow the event

For 1994 data, the full release of the SRTD software took place after the setting of the DST bits. Therefore, a "loose" selection of events is used and then the new software is run which takes advantage of this component. Each event from 1994 is firstly selected when both bits 9 and 11 are set. Bit 9 is set in 1994 data set when any of four available online electron finders believes it has found an electron with $E'_e > 4$GeV. Bit 11 is set in 1994 data when the event passes a loose δ cut (> 25GeV) .

To make sure that the relevant **ZEUS** components were in a state sufficient for the accurate reconstruction of event qualities, a data quality routine is called. This routine removes $\sim 20\%$ of 1994 events.

2.2.5 DIS background rejection

Since only NC DIS events are wanted for the analysis of energy flows, much care is taken in the event selection. Major sources of background exist to these events, even after triggering and preselection; notably, beam-gas and photoproduction. Moreover, only events whose kinematic variables can be adequately reconstructed are selected.

For an event to be classified as NC DIS, it must pass the following criteria:

1. Event primary vertex cuts are made in an effort to reduce beam-gas background events. Both the 1993 and 1994 analyses use events only when $-50 <$ vertex $Z < +40$cm and vertex radius $R < 8.5$cm. The 1994 analysis uses a tighter vertex $Z < +25$cm to remove any satellite events[1] since the simulation of their contribution is inadequate. Typically, 5% of events are removed by these cuts [29].

2. A tighter calorimeter timing cut is used than that in the DIS trigger. For both the 1993 and 1994 analyses, the event is accepted if $|$RCAL time$| < 3$ns and $|$FCAL time $-$ RCAL time$| < 8$ns. These cuts remove beam-gas background events. Approximately 5% of events triggered by the DIS trigger and preselected in 1994 are removed by this cut.

3. To reduce the beam-gas background, photoproduction background and cosmic muon events, a tighter cut is made on δ. Only events with $35 < \delta < 60$GeV are accepted. The lower limit of 35GeV removes photoproduction and beam-gas background events. The upper limit of 60GeV removes events which cannot have been the result of an ep collision; for example that of a cosmic muon passing through **ZEUS**.

4. The scattered electron must be found by the main electron finder (EEXOTIC or SINISTRA) where $E'_e > 10$GeV (to enhance purity). In addition, a "box cut" is placed on the position of this electron. In 1993 data, the event is allowed to pass if $|X_{el}| > 16$cm and $|Y_{el}| > 16$cm measured from the centre of the beam hole in the RCAL. In 1994 data, with the addition of the SRTD, the box cut is reduced to 13cm.

5. The resolution of certain kinematic quantities becomes poor at the extremes of the **HERA** phase-space [23]. Additionally, photoproduction background becomes significantly higher at very high values of y. Of course, photoproduction background also increases with a decrease in measured Q^2. The following broad kinematic cuts are made on the DIS events: $y_{JB} > 0.04$, $y_{el} < 0.95$, $Q^2_{DA} > 10\text{GeV}^2$(1993), $Q^2_{mix} > 6\text{GeV}^2$(1994).

---

[1] A satellite event is an ep interaction at the **HERA** energy between the leading pilot bunch of one beam and a colliding bunch of the other beam. The electron pilot bunch interactions constitute the majority of these events which are perfectly acceptable for physics analysis.

6. Initial state radiative DIS events are characterised by a low energy photon being detected by the LUMI-γ monitor. High energies in this monitor distort the reconstruction of kinematic variables and are removed. Only events with $E(\text{LUMI}\gamma) < 5$GeV are accepted.
7. A certain class of events, *diffractive* events, which are discussed in section 5.2, are isolated from the other NC DIS events. In the 1993 analysis, a cut is made on events which have no energy at $\eta > \eta_{max} = 1.5$. In the 1994 analysis, the diffractive events are separated by a cut on x_{pom} (defined in section 5.2 and roughly proportional to $\eta_{max}) < 10^{-2}$.
8. A call is made to a muon rejection algorithm [28] which looks at various components and the event topology to establish whether the event trigger is due to a cosmic muon which has passed through the detector. These account for $\sim 0.1\%$ of triggered DIS events.
9. Compton QED events can fool the DIS trigger. Such events are characterised by very little activity in the detector. If 1 or 2 isolated electromagnetic condensates are found in the calorimeter but nothing further, the event is classified as a Compton event. About 0.8% of events are of this type.
10. The LUMI monitors set flags when electron and proton bunches have collided. If both flags are set, an *ep* interaction has occured. Non-*ep* events which pass the DST selection cuts account for $\sim 1\%$ of events.

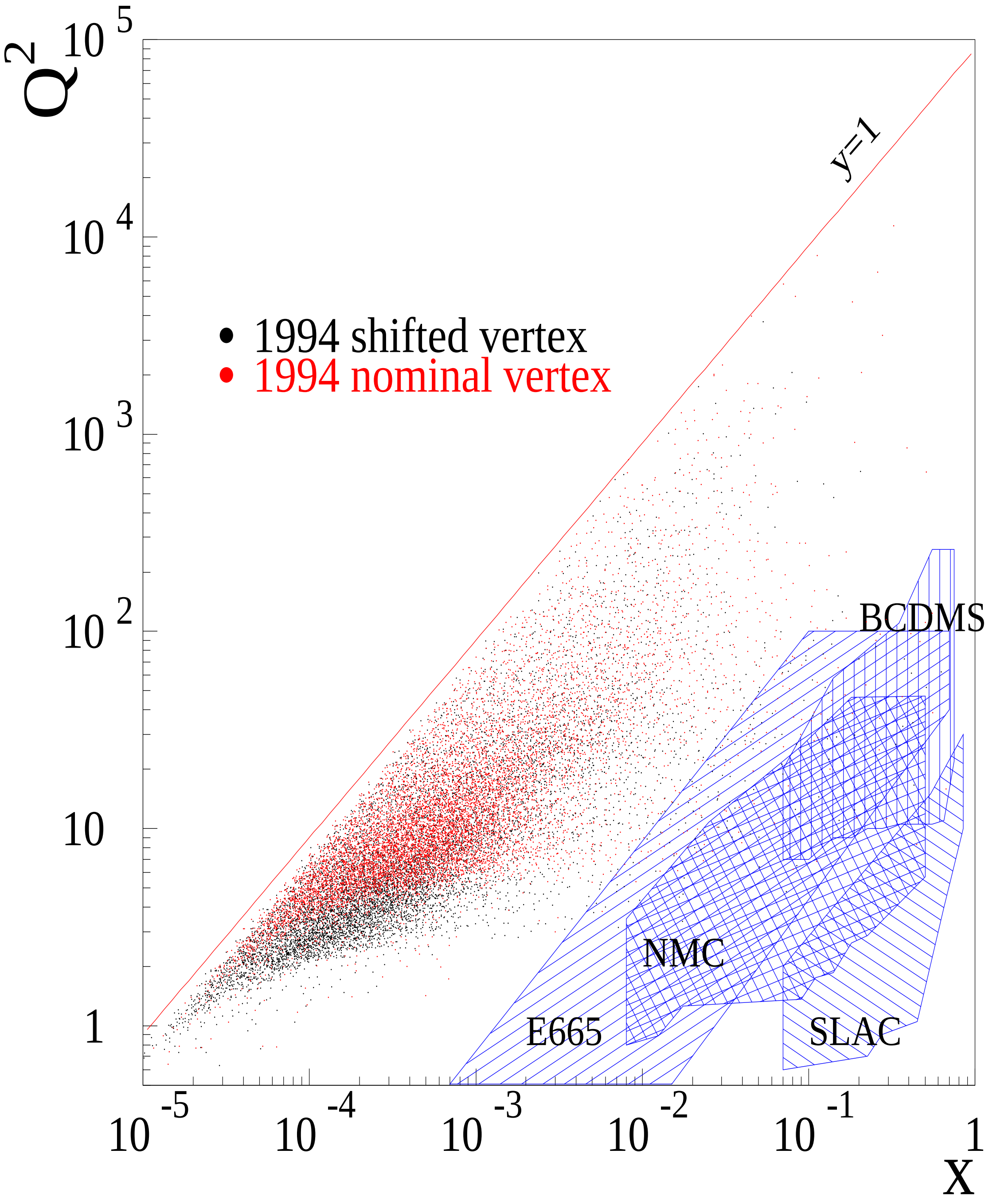

Figure 2.5: *The kinematic distribution of reconstructed NC DIS events in 1994 data. The shifted vertex points refer to* $32nb^{-1}$ *[2] of ep interactions at a primary vertex of* $Z \approx +65cm$*. Shown also are the kinematic ranges of some earlier experiments. Plot extracted from [25].*

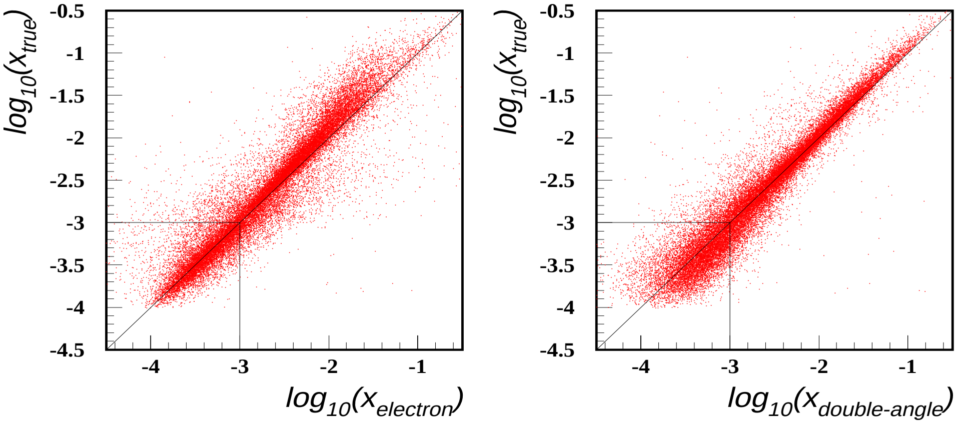

Figure 2.6: *The electron and double-angle methods of reconstructing* x_{bj}*. Note the improvement of the electron method over the double-angle method for* $x < 10^{-3}$*. The 1994 analysis takes advantage of this.*

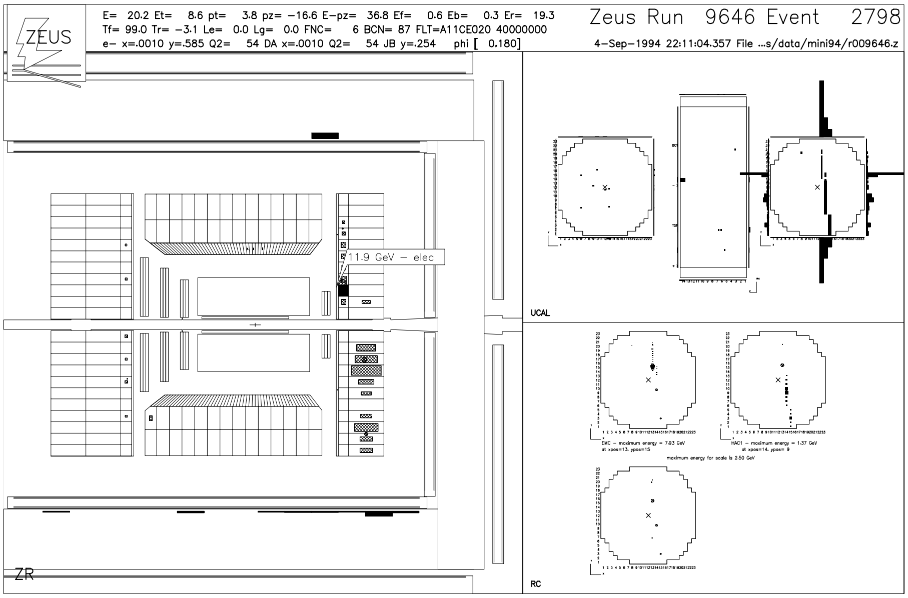

Figure 2.7: *A candidate for a cosmic muon event. The muon has passed through the electromagnetic and hadronic sections of the* RCAL*. The resulting deposits have fooled an electron finder.*

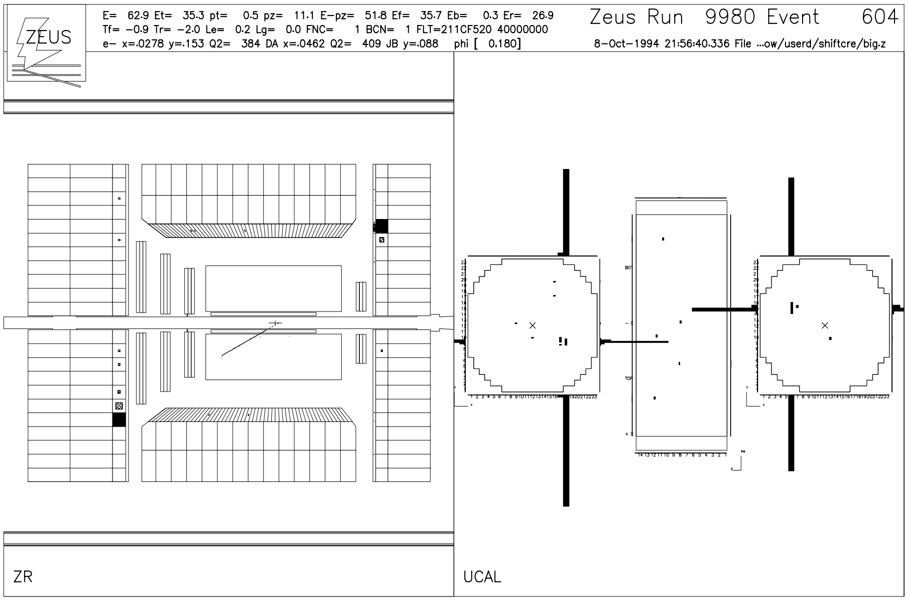

Figure 2.8: *A candidate for a Compton QED event. The two deposits in the calorimeter are the e^- and γ, a track indicates which is the e^-.*

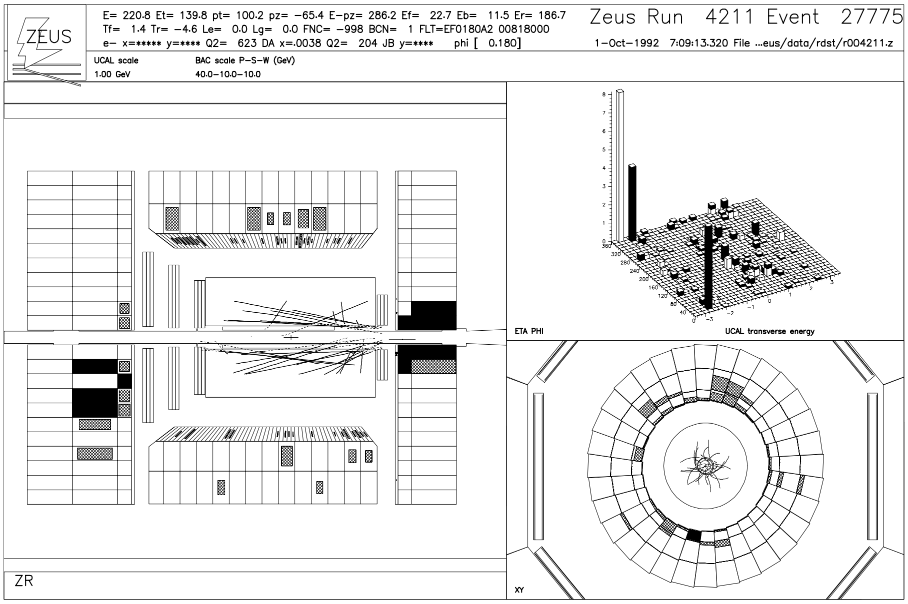

Figure 2.9: *A typical beam-gas event. Instead of the electron and proton beams colliding, a proton has collided with a nucleus of the residual gas in the beam-pipe.*

Chapter 3

QCD Models and Motivation

3.1 The quark-parton model

The quark parton model (QPM), introduced in the previous chapter, gives the simplest description of the partonic DIS process. Although this model is an approximation, it is very useful for studying the basic scattering process. DIS in the QPM is viewed as the scattering of a single valence or sea quark which carries a momentum-fraction x of the proton's momentum P. It neglects all QCD radiation and corresponds to the zeroth order expansion in the QCD coupling constant α_s.

In the QPM model, the partonic final state contains two coloured objects, the scattered quark and the proton remnant. The cross-section for the process is proportional to the densities of partons within the proton and the proton remnant is considered a spectator.

In the $\gamma^* p$ centre of mass system (hadronic CMS or HCM), these two coloured objects lie in the $+Z$ and $-Z$ directions, each of them having an energy $W/2$. This strict subdivision of phase-space is only applicable in the QPM picture.

When the partonic final state hadronises, there are two main jets of hadrons. One is associated with the struck quark which hadronises to form the current jet. The other is associated with the proton remnant.

This hadronisation, when coupled with other, non-perturbative, effects such as the intrinsic (or primordial) k_T of partons within the proton, destroys the simple picture. Fragmentation produces a continuous chain of hadrons between these jets leaving them with no clean separation. This region is called the *central* region.

3.2 QCD corrections to the QPM

Quantum chromodynamics (QCD) is the field theory of strong interactions. In this theory, spin-$\frac{1}{2}$ quarks (q) which are bound together by massless, spin-1 bosons called *gluons* (g) make up the proton. In other words, QCD adds the concept of gluons to the QPM which contains only quarks.

A less approximate approach to the description of DIS events involves the addition of QCD corrections to the QPM. In first order QCD, two final-state partons are produced. These basic QCD processes are QCD Compton scattering (QCDC), figure 3.1b, and boson-gluon fusion (BGF), figure 3.1c.

(a) O(α) QPM vertex

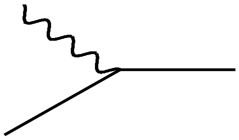

(b) O($\alpha\alpha_s$). QCD correction q → gq

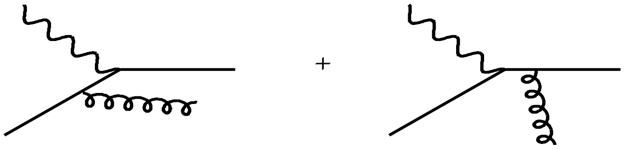

(c) O($\alpha\alpha_s$). QCD correction g → q$\bar{\text{q}}$

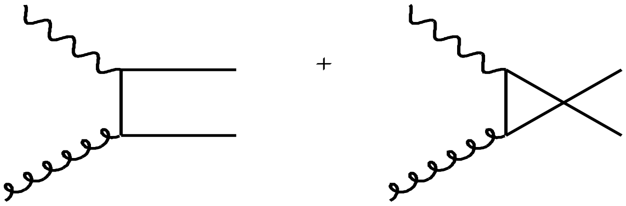

Figure 3.1: *Lowest order QED and the addition of lowest order QCD corrections to the DIS vertex.*

In the simple QPM, the quantity F_2, one of the proton structure functions, is defined as

$$F_2(x) = \sum_f e_f^2 x(q_f(x) + \bar{q}_f(x)) \tag{3.1}$$

where the sum runs over all quark flavours. e_f is the electrical charge of a quark of flavour f and the $q, \bar{q}$ are the parton distribution functions for quarks and antiquarks of momentum fraction x. In other words, $q_f(x)dx$ represents the probability of finding a quark of flavour f carrying a fraction of the four-momentum of the proton between x and $x + dx$.

With first-order QCD corrections, there is the addition of an energy scale dependence (Q^2) on F_2 and the inclusion of a gluon distribution term. The effective parton distributions evolve in both x and Q^2 [33].

Recently, measurements by both the **ZEUS** [38] and **H1** [39] detectors have shown a steep rise in F_2 at low-x. Analyses of these results using both detectors' measurements show that the gluon distibution is the dominant contributor to this rise [40] [41]. The growth of gluon density at small x is due to gluon radiation and can be represented by figure 3.2 [34].

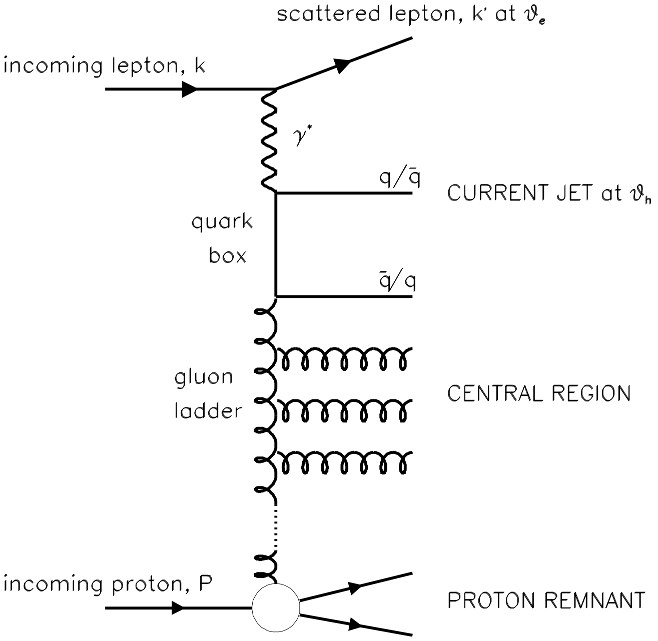

Figure 3.2: *The "gluon ladder" representation of NC DIS at low x_{bj}*

3.2.1 The DGLAP picture

A set of equations, the Dokshitzer-Gribov-Levin-Altarelli-Parisi equations [61], can determine the Q^2 evolution of the quark densities based upon the QCD corrections

$(q \rightarrow gq, g \rightarrow q\bar{q})$ from any reference point (x, Q_0^2). The evolution is based on terms $\ln(Q^2)$ of a QCD expansion.

$$\frac{dq_i(x,Q^2)}{d\log Q^2} = \frac{\alpha_s}{2\pi}\int_x^1 \frac{dy}{y}\left(q(y,Q^2).P_{qq}\left(\frac{x}{y}\right) + g(y,Q^2).P_{qg}\left(\frac{x}{y}\right)\right) \tag{3.2}$$

$$\frac{dg(x,Q^2)}{d\log Q^2} = \frac{\alpha_s}{2\pi}\int_x^1 \frac{dy}{y}\left(\sum_i q_i(y,Q^2).P_{gq}\left(\frac{x}{y}\right) + g(y,Q^2).P_{gg}\left(\frac{x}{y}\right)\right) \tag{3.3}$$

where $i = 1...2n_f$ for all quarks and anti-quarks of flavours 1 to n_f.

The first term on the right-hand side of equation 3.2 states that a quark of momentum fraction x can originate from a parent quark of momentum fraction y where $y > x$. The probability for this to occur is proportional to $\alpha_s \cdot P_{qq}(x/y)$. The second term states that a quark of momentum fraction x can originate from a parent gluon of momentum fraction y, $y > x$. This has a probability proportional to $\alpha_s \cdot P_{qg}(x/y)$.

These P_{ij} are known as the *splitting functions.* By setting $z = (x/y)$ they are, to leading order, defined as:

$$\begin{aligned}
P_{qq}(z) &= \frac{4}{3}\left(\frac{1+z^2}{1-z}\right) \\
P_{qg}(z) &= \frac{1}{2}\left(z^2 + (1-z)^2\right) \\
P_{gq}(z) &= \frac{4}{3}\left(\frac{1+(1-z)^2}{z}\right) \\
P_{gg}(z) &= 6\left(\frac{1-z}{z} + \frac{z}{1-z} + z(1-z)\right)
\end{aligned} \tag{3.4}$$

The following can be concluded from these equations:

- There is a singularity in P_{qq} which is due to the emission of soft gluons. This is cancelled when virtual gluon diagrams are included into the process.

- There is an increase in the density of gluons at small x. This leads to an increase in the presence of $q\bar{q}$ pairs at small x. This can be seen from

$$\begin{aligned}
P_{gg} &\overset{x\rightarrow 0}{=} 6/z \\
P_{gq} &\overset{x\rightarrow 0}{=} 4/3z
\end{aligned}$$

Using these equations, the uncorrected QPM picture of the NC DIS interaction is altered.

The DGLAP picture calculates the gluon ladder (figure 3.2) using a leading logarithmic approach [42]. In other words, each branch of the gluon ladder is calculated independently by assuming that, going "up" the ladder, each successive gluon branch has more k_T than the previous one. The highest k_T is associated with the topmost gq vertex which is $\sim Q$. The link between this assumption and the ability to calculate each separate branch is known as the Weisaker-Williams approximation.

This "strong-ordering" in the k_Ts of the gluon ladder, which also orders the opening angles of the gluon emitted at each branch, is coupled to a strong-ordering of the momentum-fractions: going up the ladder, the effective interaction x is lower at each gluon vertex from energy-momentum conservation.

The virtual photon couples to the topmost quark which has been constructed by a $g \rightarrow q\bar{q}$ creation. This topmost quark is considered a sea quark of the proton. The effective x of the event is defined at the $\gamma^* q/\bar{q}$ vertex.

3.2.2 The BFKL picture

At the very low values of x obtainable at **HERA**, the DGLAP equations with leading order splitting functions are expected to become unreliable [23]. The splitting functions require higher order corrections and the DGLAP equations become less useful. At such low values of x, powers of $\ln(1/x)$ become dominant in the QCD expansion due to "soft" gluon emission and associated virtual gluon corrections.

An alternative parton density evolution equation has been developed by Balistsky, Fadin, Kuraev and Lipatov [43], the so-called "BFKL" equation, which is designed explicitly for this low-x region. The equation resums these logarithms to leading order in $\alpha_s \ln(1/x)$.

It makes two characteristic predictions, namely the $x^{-\lambda}$ growth of the gluon density $xg(x, Q^2)$ with $\lambda \approx 0.5$ and the relaxation of the strong-ordering of the transverse momenta, k_T, of the gluons along the ladder.

As mentioned earlier, the proton structure function F_2 and the gluon density have been seen by both detectors to rise sharply at low-x. However, this strong rise might be mimicked by mechanisms using the conventional (DGLAP) evolution equations [44]. It is not an unabiguous signal for the presence of BFKL dynamics.

However, the relaxation of the strong k_T-ordering and the resultant enhancement of the transverse energy level in the central region between the current jet and the proton remnant in DIS events at **HERA** may yield more conclusive results for the presence of BFKL dynamics [45].

3.3 The MEPS model

Using QCD perturbation theory, the matrix elements for the QCD correction processes QCDC and BGF have been exactly calculated to $O(\alpha_s)$ (recently to $O(\alpha_s\alpha_s)$).

The $O(\alpha_s)$ calculation has been included in the current generators available, including LEPTO.

An exact description of parton emissions is thus available to the generators up to a limit when very soft and collinear parton emissions give rise to divergences in this calculation. These can be partly cancelled by higher-order corrections and partly absorbed into the parton density functions.

In the MEPS model, a cutoff is imposed to avoid this divergent region. This is done by requiring that $\frac{m_{ij}^2}{W^2} > y_{cut}$ where m_{ij} is the invariant mass of the produced parton pair. In practical terms, it is preferable to keep the cutoff as low as is feasible to retain as large a region of analytically-calculable phase-space as possible. It should be smaller than any experimental jet resolution so that no observable jet emission is lost.

Beyond this cutoff, a parton shower approach is used to model the almost-collinear emissions. This is a DGLAP-based approximation for low-angle gluon emission to all orders in perturbation theory.

In DIS, the struck quark can emit gluons both before and after the photon vertex. The emissions prior to the interaction are known as initial state and those after as final state. The gluons emitted can further emit partons. These cascade and become initial and final state parton showers.

The initial state shower, in “chronological” order, consists of a set of partons, close to mass-shell ($\approx$ 1GeV), one or more of which may initiate a cascade. The partons are predominantly gluons as inferred from the DGLAP splitting funtions. In each branch of this cascade, one of the daughters continues towards the hard interaction vertex ($\gamma^* q/\bar{q}$) with an increased spacelike virtuality, while the other is on mass-shell or aquires a timelike virtuality (in which case it will develop a timelike shower of its own). The initial state shower is a spacelike shower. It is ordered up the parton ladder in increasing Q^2, decreasing energies (decreasing x) and increasing average opening angles as per the DGLAP representation.

The final state shower is characterised by a timelike quark (the struck quark) showering into daughters which have decreasing off-shell masses. At each branch of the shower, the opening angles decrease as well as the energies.

This strict separation of the initial and final state parton cascades is a feature of the MEPS model. It is an artificial separation and no interference between the two showers is taken into account.

The parton shower approximation is leading-logorithmic, using the DGLAP evolution equations and so-called Sudakov form-factors [36]. The evolution equations give the contribution from the real diagrams as represented by the gluon ladder diagram, whereas the form-factors sum the virtual corrections and unresolvable real diagrams. The use of these form-factors limits the emission.

A final cutoff is applied to the parton showering model which is mainly used to avoid collinear or infrared singularities.

The parton shower approximation is improved with the enforcement of a QCD coherence condition, which is not inherent in the leading- logarithmic approach, and use of a running α_s. The coherence corresponds to infrared singularities and serves to reduce gluon emission at certain angles due to destructive interference.

While all generators used to compare with the analyses which follow use the splitting-functions of the DGLAP equations to describe the leading-order processes of parton showering, the implementation of the coherence and running α_s vary greatly from one generator to another.

The parton showering incorporated into the MEPS model uses the DGLAP evolution equations to the collinear limit. This is an assumption of the model and means that MEPS explicitly uses conventional dynamics in an attempt to reproduce the qualities of a DIS event.

LEPTO6.1 is a software incorporation of the matrix-element-parton-shower (MEPS) model [35]

3.4 The colour dipole model

ARIADNE is the computational realisation of the colour-dipole model (the CDM) [37]. Versions 4.03 and 4.06 have been used to analyse data collected in 1993 and 1994 respectively.

In the basic version of the CDM, QCD radiation of quarks and gluons is described by a chain of radiating colour dipoles. In the case of, for example, emission of a gluon from a $q\bar{q}$ system, three coloured objects are produced: a quark, antiquark and gluon. Further gluon emission from this state is treated as emission of two independent dipoles where the transverse momentum of the second gluon is smaller than that of the first. The resulting state continues the emission process, with the k_T of the emitted gluons decreasing at each stage.

This leads to a kinematical constraint for the allowed emission angle of each gluon and corresponds to the strong angular ordering used by the parton shower model.

In the DIS process, the CDM does not distinguish between an initial and final-state cascade, unlike the parton shower model. All emission is described by radiation from the colour dipole formed by the struck quark and the proton remnant.

Emission of wavelengths shorter than the size of an emitting dipole is suppressed. This is implemented in the CDM by only allowing a fraction of the remnant to take part in emissions, this suppression of emission has no analogy to the parton shower approach.

One important extension required, especially at low x, is the inclusion of the BGF process. First order matrix elements for the process are used followed by the dipole emission. For technical reasons, this imposes a cutoff on the maximum k_T of gluon emission which is not inherent in the model. Furthermore, a dependence on y_{cut} is introduced. The inclusion of the BGF process into the CDM model results in what will be called the CDMBGF model. Both versions of ARIADNE used in the analyses simulate this model.

The CDMBGF model, as opposed to the MEPS model, does not explicitly use the DGLAP equations when calculating the parton showers beyond the matrix-element cutoff (y_{cut}). There is no consensus as to whether the CDMBGF approach is similar to that of BFKL-inspired calculations or that of the DGLAP or conventionallyinspired calculations. No generator currently exists which explicitly uses BFKL parton evolution. The CDMBGF model at least gives us an opportunity to look at the results of an approach which is not strictly conventional.

3.5 Hadronisation

Hadronisation describes the process of transforming partons into jet(s) of hadrons, in other words the transition from the short to the longer distance behaviour of QCD.

The process can be divided into the perturbative phase of gluon emission, as in the parton shower model, and the non-perturbative phase of hadronisation. Although this division seems clear by the definition, both phases are connected and cannot be viewed separately. Many different hadronisation models exist and the relative importance of the phases differs in each.

At present, there is no clear understanding of the process of hadronisation. Phenomenological models, containing many adjustable parameters, are used instead. In the physical models MEPS and CDMBGF simulated by LEPTO and ARIADNE respectively, the program JETSET version 7.4 [47] is added to simulate the hadronisation process.

The JETSET model is an implementation of the Lund String Model [59]. In this picture, a string is a narrow flux tube of colour force separating two coloured partons. If the particles separate, the string is stretched. This stretching requires energy since the colour force rises with increasing separation. At a high enough string energy, a $q\bar{q}$ pair can tunnel out of the vacuum. The string then breaks into two and the subsequent four particles can continue separating. Therefore the inital string will break up producing conventional hadrons. The splitting of the string is governed by the Lund symmetric fragmentation function (see equation 6.1); hadrons produced by the string splitting aquire some transverse momentum according to the parameters of this function.

In the Lund model, gluons are viewed as “kinks” on otherwise straight strings. Segments of the string will move due to the 4-momenta of these gluons and this directly affects the momenta distribution of the final state hadrons.

3.6 Summary

The hadronic final state of a DIS event has the following regions of interest in the laboratory frame.

1. The current jet. This is a group of hadrons associated with the hadronisation of the struck quark in the QPM. The centre of the jet is located about a polar angle of θ_h degrees. (The angle of the struck parton in the QPM.) This region is also known as the photon fragmentation region.
2. The proton remnant. The hadronisation of the remaining partons within the proton after the collision. The small intrinsic transverse momentum (k_T) of these partons leads to a narrowly-confined hadron jet which is not seen in the **ZEUS** calorimeter.
3. The central region. A number of partons hadronises in the angular range between the current jet and the proton remnant. The momenta of these hadrons depends, amonst other things, on the evolution process which takes place along the gluon ladder.

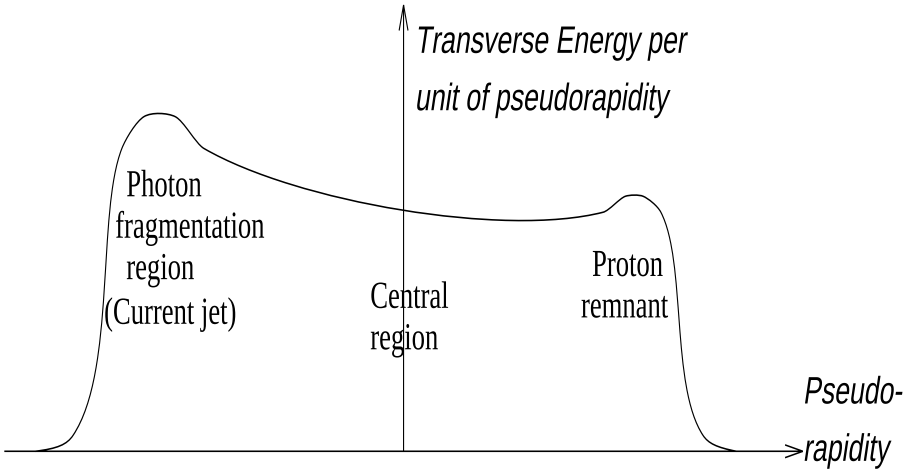

Figure 3.3: *A qualitative depiction of the shape and relative level of E_T flow in the three regions in the $\gamma^* p$ centre of mass.*

Final state hadrons in any one particular event are produced preferentially in one azimuthal region due to conservation of momentum with the scattered electron. Averaged over all events, the azimuthal production of hadrons is isotropic.

Chapter 4

Extraction of the Far-Forward $\mathbf{E}_T$ Flows

4.1 Introduction to energy flows

Energy flow is defined by the expression $\frac{1}{N}.\frac{dE}{d\eta}$ and can be pictured as the sum of hadronic energy flowing into one unit of pseudorapidity as a function of pseudorapidity. The N in the expression refers to the normalisation required when the energy flow is calculated for N events. Averaged over all events in a kinematic range, an energy flow is produced for the generalised DIS process. The conversion of energy flow to transverse energy flow is simply the substitution of E_T ($E \sin\theta$, where θ is the polar angle between the forward direction and the direction of particle travel) for E.

Indications of an enhanced transverse energy flow have been presented [48, 49]. However, the measurement of the energy flow is complicated since the $\gamma^* p$ central region in low-x events at **HERA** maps to the very forward region $\eta_{lab} > 2(\theta < 15^\circ)$ of the detectors in the laboratory.

In this region, the resolution in η degrades rapidly with increasing η, the amount of dead material in front of the calorimeter rises, boundary effects at the edge of the detector become important and high-energy particles well outside the geometric acceptance, interacting with beam pipe elements, spray into the calorimeter. All of these effects are compounded with the fact that currently no reliable models for the proton remnant fragmentation exist.

The analysis presented in this thesis is the first time that the energy flow has been measured at $\eta > 2.5$ in **ZEUS** with an understanding of the measurement error.

4.2 Principle of correcting detector observation

The energy flow is determined from all calorimeter cells with energies above 60MeV (EMC cells) and 110MeV (HAC cells). These values suppress calorimeter noise. The pseudorapidity, η, is calculated from the angle between the proton direction and a line connecting the measured NIP and the centre of the cell.

The distributions measured in this way are distorted with respect to the hadronic energy flows of the true final state. Trigger biases, event selection cuts and the finite acceptance and resolution of the detector all combine to cause this distortion.

To correct for these effects, trigger and detector simulation programs are used in conjunction with event samples generated from physics Monte Carlo programs.

For example, particles coming from the the primary interaction are stable hadrons by the time they reach the **ZEUS** calorimeter. Nearly all of the energy of these hadrons is contained and measured by the CAL. The efficiency of this detection, the dead material through which the particles must pass before depositing in the calorimeter and the way in which the deposited hadronic energy is converted into a signal must all be simulated. In this way, the signals appearing in the detector in real events can be traced back to the hadrons which cause them. This translates into information concerning the form of the partonic interaction.

The first stage of simulation is the creation of hadron 4-vectors using a physics model. Two such physics simulation programs, LEPTO and ARIADNE, described in the previous chapter, are used in this thesis for the correction of data. The **ZEUS** collaboration uses a detector simulation program based on GEANT [6] to estimate the trajectory and energy deposit of these hadrons through matter. A further stage of simulation evaluates the triggering effect of these deposits. The results of this event simulation are passed through the same reconstruction package, ZEPHYR [31], as real events.

In principle, the simplest form of correcting these distortions is as follows:

$$f(had) = \frac{f(obs) \times f(sim.had)}{f(sim.obs)} \tag{4.1}$$

where $f(obs)$ is the uncorrected transverse energy flow which is observed in the detector, $f(sim.had)$ is the flow from the set of hadron 4-vectors produced by the physics model, $f(sim.obs)$ is the flow after taking these 4-vectors through the detector simulation and $f(had)$ is the measured hadronic transverse energy flow.

This correction method is also known as the *bin-by-bin* method since each measured range within the raw distribution (bin) is independently corrected back to the undistorted value by the corresponding bin from the correction formula.

For the purposes of the analyses presented in this thesis, the observed transverse energy flow is corrected back to the E_T flow in the hadronic final state (HFS), also called the hadron-level E_T flow. The HFS is defined as those hadrons which are stable by the time they reach the calorimeter. This includes the decay products of weakly-decaying particles [32].

4.3 Measuring energy flow in the forward region.

4.3.1 The observed energy flow.

The starting point for understanding the forward energy flow is the analysis of energy deposition in individual calorimeter cells, without any further clustering.

The observed transverse energy flow is calculated using the position of the geometric cell-centres and calculating their angles with respect to the measured vertex of the events. The source of this information is a table of data which is filled by the **ZEUS** data aquisition system. It contains a list of calorimeter cells and the energy deposited in them for each event after calibration constants and online noise suppression have been applied [51].

The result of this calculation is shown in figure 4.2.

There are two main features of the observed energy flow:

1. The energy flow distribution exhibits “bumps” and “holes”. It seems they are modelled in the Monte Carlo but at a lower energy value. What is their origin?

2. There is an excess of transverse energy, which increases with increasing η (decreasing polar angle), found in the data over that predicted by ARIADNE4.03. Is this excess an effect of inadequate detector simulation? If not, what does it represent in terms of hadron energies?

Two preclustering algorithms, the **condensate** and **island** algorithms, can be used to predict the angles of particles incident to the calorimeter in the middle of the detector ($|\eta_{lab}| \leq 2.0$). To calculate these angles, both algorithms use an energy weighting of calorimeter cells by assuming that these cells are the result of one particle's interaction with the calorimeter.

In the very forward region, there is a high angular density of particles compared with that of cells. In other words, single cells may contain the energy deposits of more than one particle (figure 4.3a). Thus, neither condensates nor islands result from single particles in the forward region of **ZEUS** (figure 4.3b).

Since the position information cannot be extracted using the condensate or island algorithms, there is no advantage gained by using them in the forward region in this analysis.

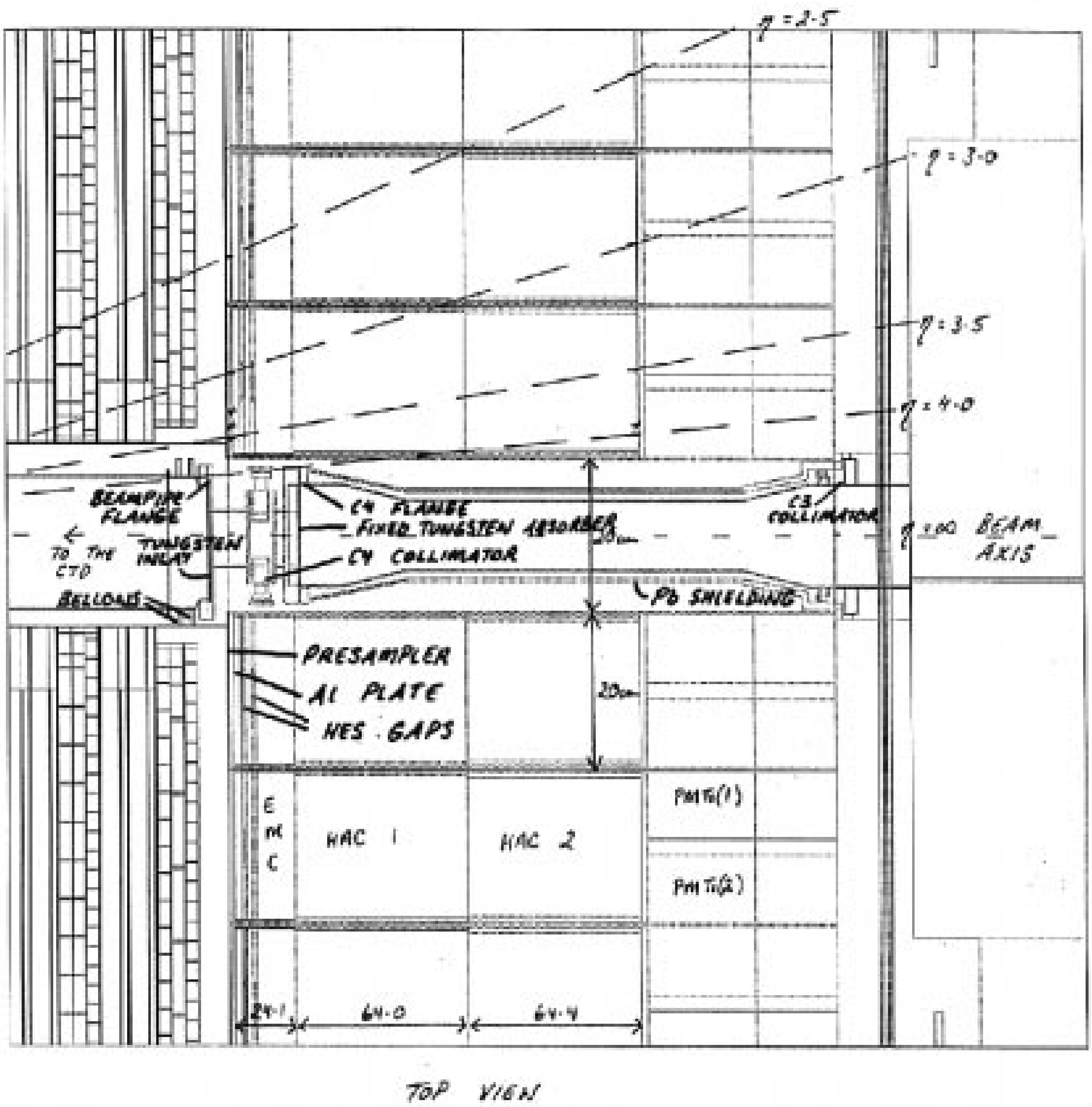

Figure 4.1: *The top view of* **ZEUS** *in the forward region as drawn by* GEANT *with* **ZEUS** *geometry description version* NUM12V1.

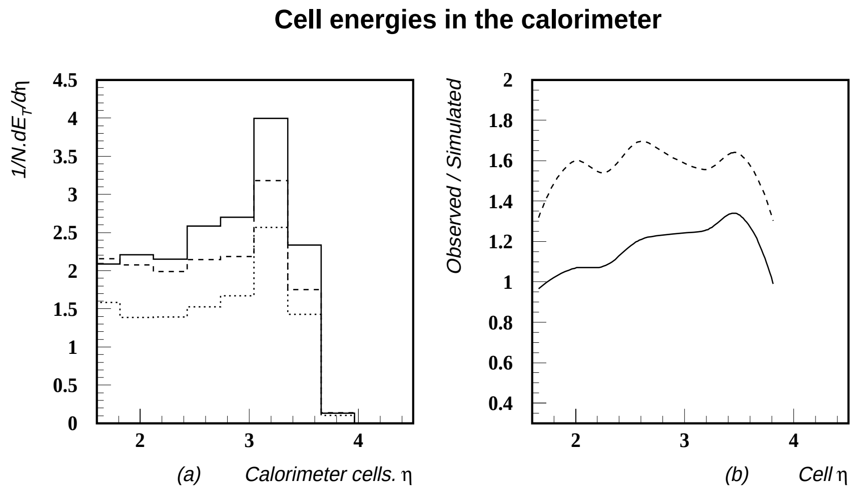

Figure 4.2: *(a) The normalised transverse energy flow from uncorrected cell energies. The solid histogram corresponds to 1993 DIS data, the dashed histogram to* NUM12V1 *Monte Carlo using* ARIADNE4.03 *(CDMBGF) and the dotted histogram to* NUM12V1 *Monte Carlo using* LEPTO6.1 *(MEPS). The statistical errors on the plots are* $< 1\%$. *The solid curve in (b) is the ratio of uncorrected observed flow from the data to the uncorrected flow from* ARIADNE4.03, *the dashed curve is the ratio of the uncorrected observed flow to the uncorrected flow from* LEPTO6.1.

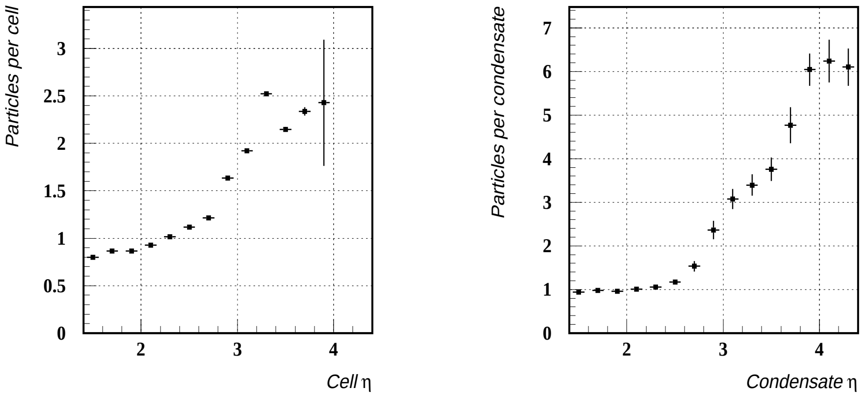

(a) (b)

Figure 4.3: *Mean number of particles per cell (a) and condensate (b) as a function of angle. The source of this plot is* NUM12V1 *Monte Carlo using* ARIADNE4.03. *The islands algorithm, not shown here, produces a very similar distribution to (b).*

4.4 Detector simulation at angles $\theta < 10^\circ$

A proper simulation of the detector response at polar angles $\theta < 10^\circ$, i.e. in the very forward region, is difficult. The difficulties arise for several reasons:

- the particle multiplicity is large and the average energy per particle is high;
- the geometrical acceptance of the calorimeter on the face of the FCAL ends near 44mrad ($\eta = 3.8$). This corresponds to a distance of 10cm from the beamaxis and is only 30cm away from the impact point of a 10°–particle ($\eta = 2.4$). This range, $44 < \theta < 174$mrad, corresponds to less than 2 FCAL towers so the angular resolution is degraded;
- the amount of dead material in front of the calorimeter in this angular range, measured in units of radiation length ($X_\circ$), may be as large as 4. The distribution of the dead material is only approximately known and is not azimuthally symmetric;
- there is a large amount of material at angles below the geometrical acceptance of the calorimeter. Examples are the beampipe flange near Z=214cm, directly in front of the FCAL, and the C4 collimater just inside the beampipe hole of the FCAL. Particles interact in this material and secondaries from these interactions reach the calorimeter resulting in the acceptance of the calorimeter reaching as far as 6 units in pseudorapidity (angles as small as 5mrad). The processes leading to these effects are complicated since the calorimeter "sees" only the tails of highly energetic showers which may not be adequately described;
- the physics processes that deposit energy in this region are not well understood adding the complication of "uncertain physics" to a complicated detector simulation problem.

If one could reverse the polarity of **HERA** one could investigate the response of the detector in this region using the kinematic peak electron test beam. The kinematic peak electron test beam is a way of calculating the dead material in front of the RCAL using data. Scattered electrons whose energy is known via other kinematic variables deposit a fraction of their energy in the calorimeter. This fraction is position dependent and the amount of dead material at any scattered electron angle from the interaction point can be mapped. Although scattered electrons in high Q^2 events can deposit in the FCAL, too few events exist. If such electrons were available in any numbers, the dead material in front of the FCAL could be mapped. Until this is possible, one has to make do with the Monte Carlo simulation, try to understand its shortcomings and correspondingly improve it as one goes along.

4.4.1 Geometry description

Figures 4.4, 4.5 and 4.6 show cuts through the detector perpendicular to the X, Y and Z axes as it is seen by GEANT with the **ZEUS** geometry description NUM12V1. Refer also to figure 4.1 for labelling.

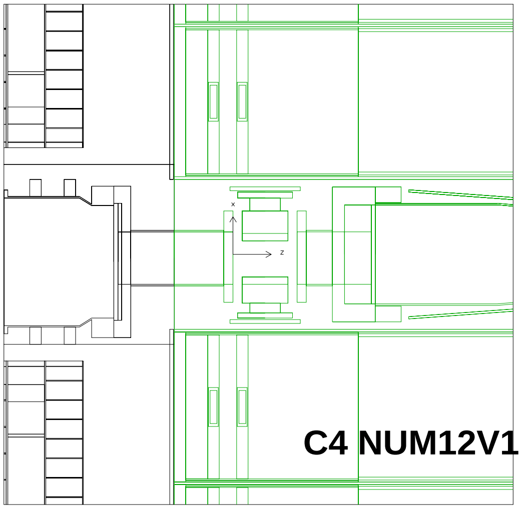

Figure 4.4: *Top view of the forward region in* **ZEUS** *according to the* NUM12V1 *geometry description. The coordinate axes are centered at* Z=*230cm and are 5cm long.*

The large beampipe flange just in front of the FCAL and the C4 collimator just inside the beampipe hole of the FCAL are very important: the flange is made from stainless steel with a thin inlay of tungsten and the outer part is steel with a thickness of 5cm. The jaws of C4 are made from tungsten.

The large flange inside the FCAL beampipe hole at larger values of Z is made from steel; inserted into this is a fixed tungsten absorber which is 4cm thick.

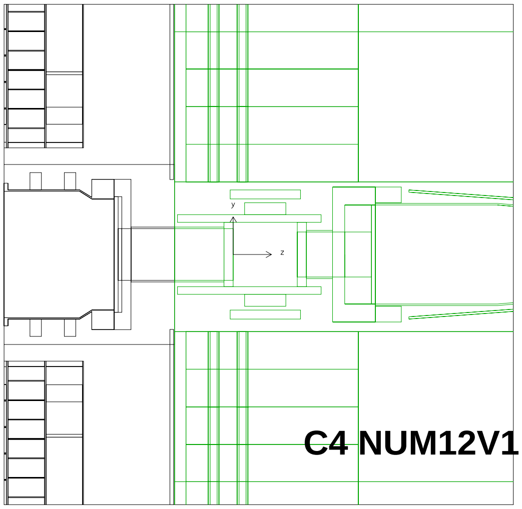

Figure 4.5: *Side view of the forward region in* **ZEUS** *according to the* NUM12V1 *geometry description. The coordinate axes are centered at* Z*=230cm and are 5cm long.*

In front of the FCAL, visible both in figures 4.4 and 4.5, there is 5mm of scintillator for the presampler followed by a 15mm thick aluminium plate. Inside the FCAL one sees the two HES gaps at 3 and 6 X_0.

Note that the central part of the beampipe is offset by -1cm in the horizontal plane (X coordinate), i.e. towards the outside of the **HERA** ring and that the FCAL is shifted by -3mm in the vertical plane, i.e. downwards with respect to the **HERA** ring. Note also the two rings around the central part of the beampipe which model the bellows installed here. The photograph in figure 4.7 shows the actual forward part of the central beampipe with the flange which is also visible in the detector simulation (figures 4.4 and 4.5). Note also the asymmetric arrangement of the nitrogen cooling pipes. Underneath these pipes, only partially visible, there are watercooling pipes which are welded to the beampipe. None of these asymmetrically arranged pipes are modelled in the Monte Carlo.

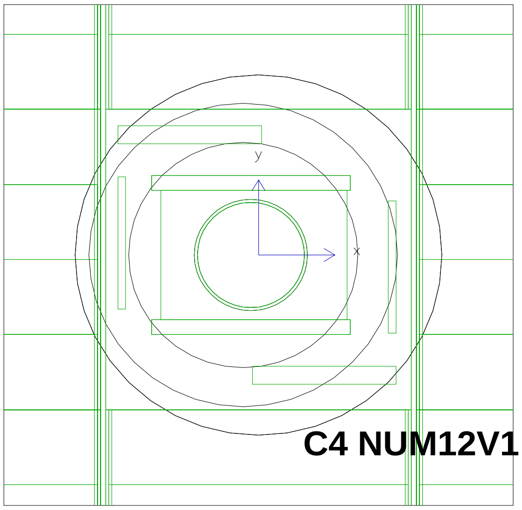

Figure 4.6: *End view of the region around the forward beampipe in* **ZEUS** *according to the* `NUM12V1` *geometry description. The coordinate axes are centered at* Z*=230cm and are 5cm long. (The proton beam direction is out of the page.) Cross-sectional views at* Z*=213,216,223 and 230cm are superimposed.*

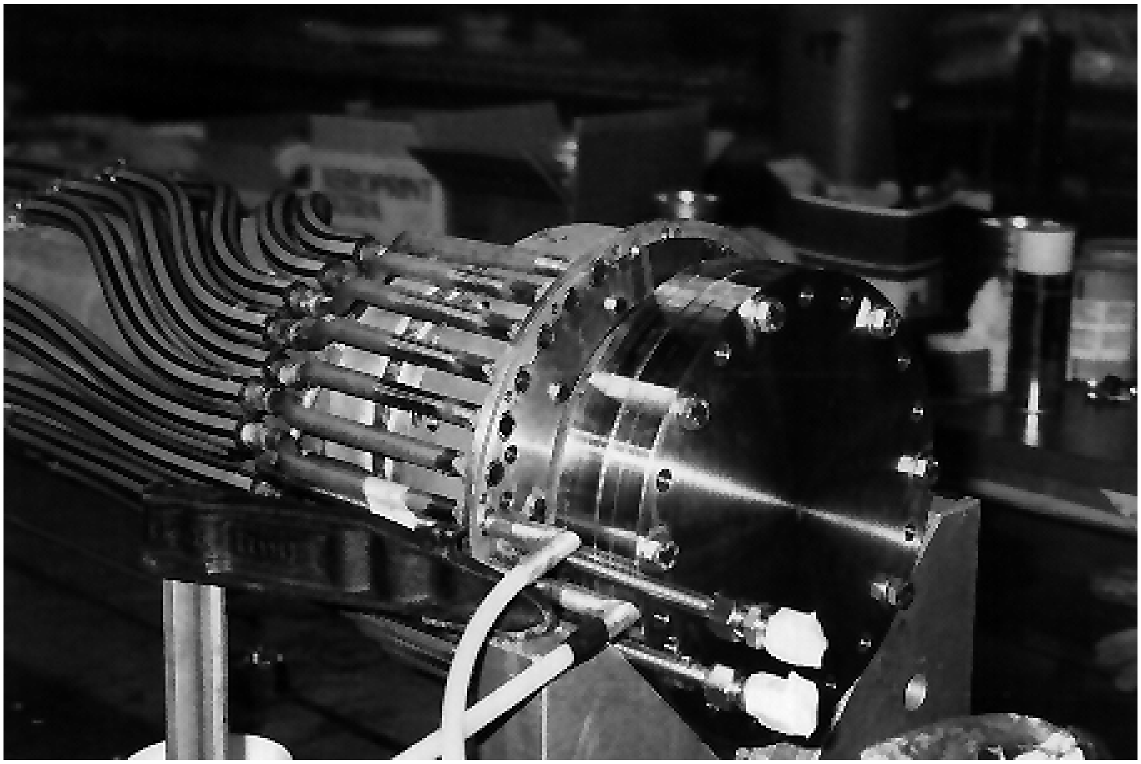

Figure 4.7: *Forward part of the new central beampipe installed during the 1994/95 shutdown. The pipes are used for nitrogen cooling and the arrangement of the pipes is asymmetric. This arrangement is similar in the old beampipe which was installed during the running periods from 1992 through 1994.*

4.4.2 Interactions in dead material

Figures 4.8, 4.9, 4.10, 4.11, 4.12 and 4.13 show the locations in the forward region where particles start showering as calculated in the Monte Carlo. Physics generator ARIADNE4.03 has been used in conjunction with **ZEUS** geometry description NUM12V1.

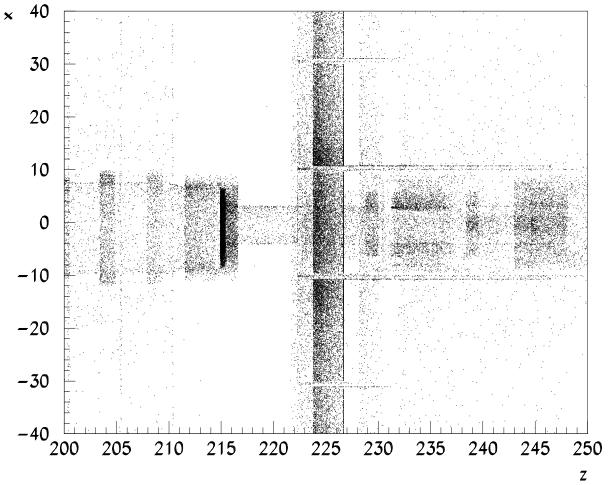

Figure 4.8: *Position in the X, Z plane where primary particles interact as calculated by the Monte Carlo.*

Figure 4.8 identifies the prominent role of the beampipe flange near Z=214cm and the C4 collimator. Quite a large number of particles start showering in this flange and secondaries from these showers may reach the calorimeter even though the primary particles are emitted at angles well outside the geometrical acceptance of the calorimeter.

This flange, the central part of the beampipe and a part of the C4 collimator are offset with respect to the beam axis by 1cm in the negative X direction. The effect of this offset is immediately visible as a shadowing effect in figures 4.10 and 4.13: more hits are seen at positive values of X near the beampipe flange near Z=214cm (the shadowing object) and less hits at positive values of X inside the beampipe wall between 270cm and 370cm (where the shadow "falls"). This effect results in an asymmetry of the energy measured on the left and on the right side of the beampipe hole in the FCAL as shall be discussed later on.

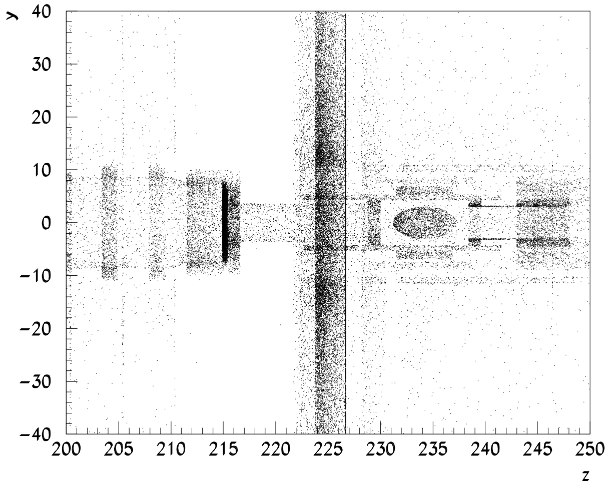

Figure 4.9: *Position in the Y, Z plane where primary particles interact as calculated by the Monte Carlo.*

4.4.3 Response to particles outside the geometrical acceptance

As indicated in the previous section, the acceptance of the calorimeter extends well beyond the geometrical aperture. This is illustrated by figure 4.14.

In the range $0.5 < \eta < 2.5$, which is completely inside the detector, about 87% of the energy of a pion (π^+, π^-) is seen with a resolution of 33% (integrated over the nominal energy spectrum). For photons, 89% of the energy is seen with a resolution of 17%.

In the range $4.5 < \eta < 5.0$, which is already strictly outside the detector aperture, only a very small fraction of the photons deposit energy in the calorimeter but pions typically deposit 33% of their energy.

At $\eta > 5$, the acceptance dies out very rapidly but tails exist up to pseudorapidities as large as 6.

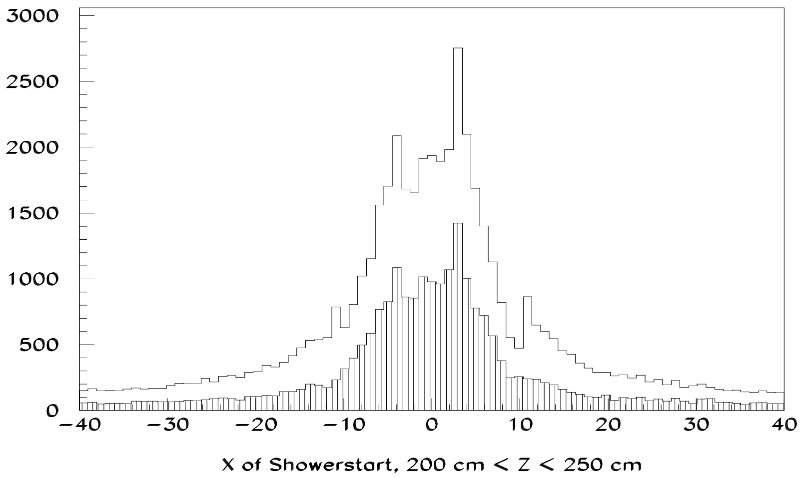

Figure 4.10: *X position in the range $200 < Z < 250cm$ where primary particles interact as calculated by the Monte Carlo. The shaded histogram is the contribution from photons.*

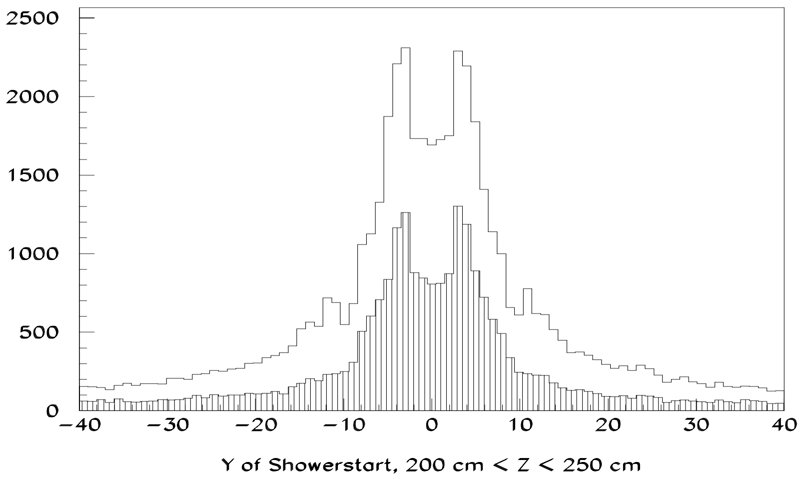

Figure 4.11: *Y position in the range $200 < Z < 250cm$ where primary particles interact as calculated by the Monte Carlo. The shaded histogram is the contribution from photons.*

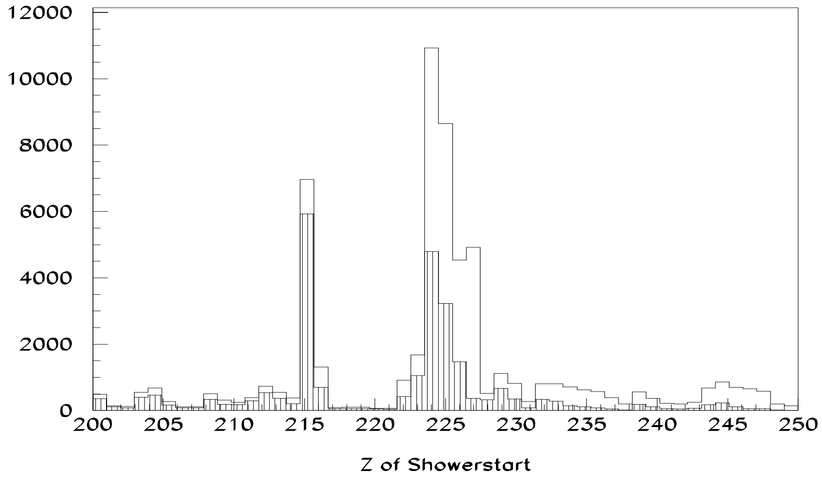

Figure 4.12: *Z position in the range* $200 < Z < 250\,cm$ *where primary particles interact as calculated by the Monte Carlo. The shaded histogram is the contribution from photons.*

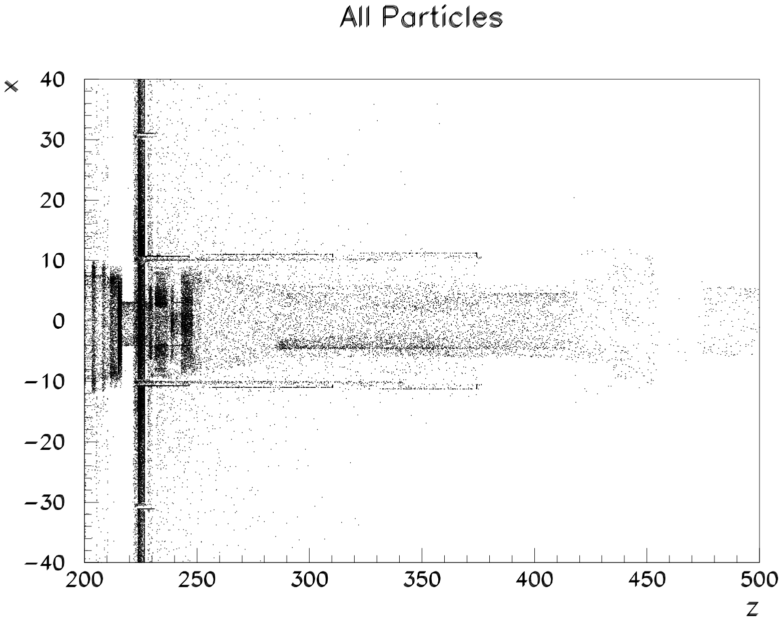

Figure 4.13: *Position in the X,Z plane where primary particles interact as calculated by the Monte Carlo. Note the excess of hits in the range* $270 < Z < 370\,cm$ *for negative values of* X*.*

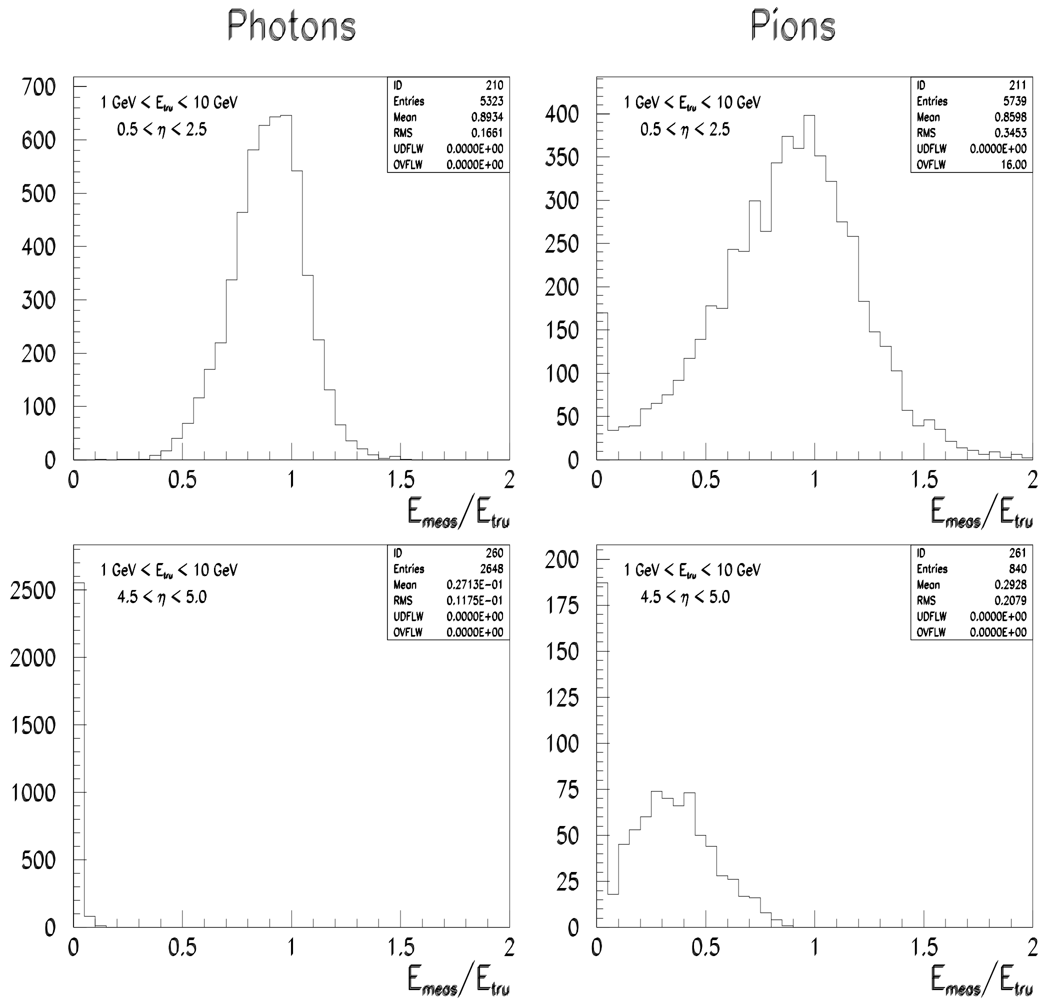

Figure 4.14: *The ratio of measured over generated energy for photons and pions (π^+, π^-) in two different η ranges. The two top plots show E_{meas}/E_{tru} for $0.5 < \eta < 2.5$ and the two bottom plots show the same quantity for $4.5 < \eta < 5.0$.*

4.5 Corrections to the observed energy.

As shown in a previous paper [48], the Monte Carlo produces an adequate simulation of the hadronic energy flow at $\eta_{lab} < 2.0$ i.e. $\theta_{lab} > 7°$. What new effects in the very forward region are simulated and to what extent? What effect does this have on the corrections from observed to measured energy flow? The observed E_T flow (figure 4.2) exceeds the simulated E_T flow from ARIADNE4.03 in 1993 DIS events in the range $Q^2 > 10\text{GeV}^2$ and $x < 10^{-3}$. Certain features of the data such as the "dip" near $\eta = 2.8$ and the "bump" near $\eta = 3.2$ are modelled but at a lower E_T level.

4.5.1 Low energy background.

A low energy background, for instance from proton beam halo, which is not modelled in the Monte Carlo may be investigated by varying the low energy cutoff in the energy flow calculation. If such a background were present in the data, the agreement between Monte Carlo and data should improve as the cutoff increases.

In fact, as can be seen in figure 4.15, the opposite happens (to a small extent). If the energy distributions of cells in the data and the Monte Carlo are similar in shape, but the mean of the data distribution is greater than the mean of the Monte Carlo distribution, the agreement between the plots will worsen as the cutoff increases. It is likely that this is the cause of the slight divergence observed.

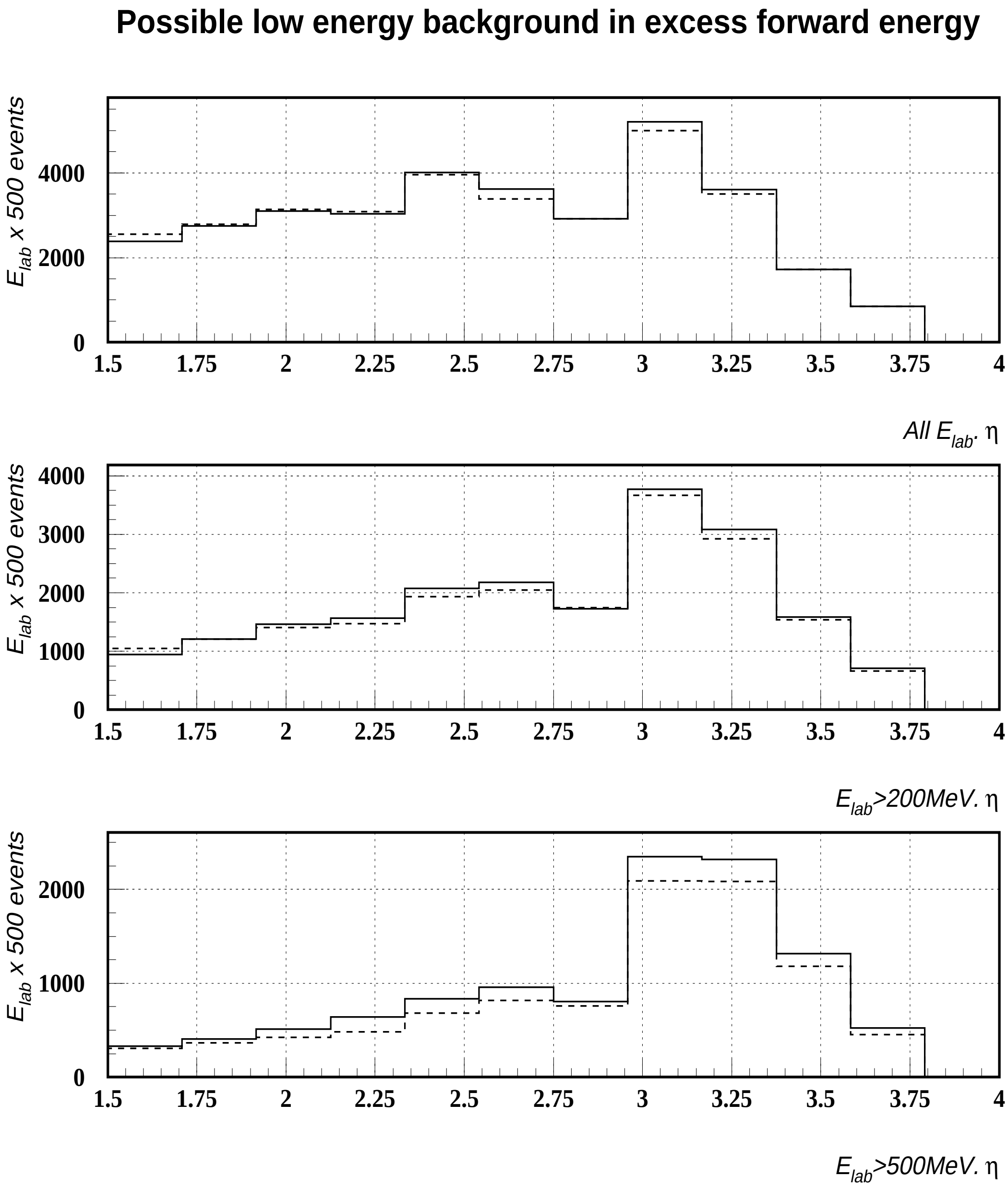

Figure 4.15: *Observed and simulated energy flow (1993 DIS data and* ARIADNE4.03 *using* NUM12V1 *geometry) for three values of low energy cutoff. The figures are not normalised, only relative differences should be considered. Solid histograms represent data, dashed represent Monte Carlo.*

Source	1993 DIS	NUM12V1	NUM10V3
$\bar{E}$(HAC1) (inner)	3.10	2.46	2.59
$\bar{E}$(HAC2) (inner)	2.12	1.59	1.75
$\bar{E}$(HAC1) (outer)	0.65	0.57	0.60
$\bar{E}$(HAC2) (outer)	0.42	0.35	0.37
$\bar{E}$(EMC)	0.98	0.94	1.05
E_{right}/E_{left}(HAC1) (inner)	1.09	0.96	1.01
E_{right}/E_{left}(HAC2) (inner)	1.17	1.09	1.09
E_{up}/E_{down}(HAC1) (inner)	1.15	1.06	1.07
E_{up}/E_{down}(HAC2) (inner)	1.12	1.05	1.01
E_{right}/E_{left}(HAC1) (outer)	1.00	0.97	0.98
E_{right}/E_{left}(HAC2) (outer)	1.05	0.92	1.03
E_{up}/E_{down}(HAC1) (outer)	1.03	1.02	0.95
E_{up}/E_{down}(HAC2) (outer)	1.02	0.97	0.97
E_{right}/E_{left}(EMC)	0.90	0.95	0.95
E_{up}/E_{down}(EMC)	1.08	1.00	1.05

Table 4.1: *Summary of the energy measurement features in beam pipe cells. Energies quoted are the mean values (not the transverse component) measured in the centres of the cells (in* GeV*). "Inner" refers to cells adjacent the beam pipe, "outer" to cells one module further away. (The statistical errors on entries in this table are negligible.)*

4.5.2 Energy asymmetry.

An energy asymmetry is observed in FCAL HAC cells nearest the beam pipe. Since the azimuthal energy flow is ϕ-symmetric, azimuthal asymmetries in the flow must come from detector effects.

Shown in figure 4.16 are the mean energies measured in the eight FCAL HAC cells adjacent the beam pipe and the eight cells one module further away. Shown also are the mean energies from the EMC cells in the first tower adjacent the beam pipe. In this region of the FCAL, there are four EMC cells (20 x 5cm (width x height) each) for every HAC cell (20 x 20cm each). The energies quoted for the EMC cells are the mean energy of each block of four cells. (The timing and imbalance cuts which are applied to the data (section 4.5.4) have a small effect on the mean beam pipe cell energies ($\sim \pm 1\%$) and a negligible effect on the energy asymmetries.) There are several important points to note (see also table 4.1):

- More energy is observed in all cells immediately above the beam pipe than in those immediately below both in the data and the Monte Carlo. One of the origins of this asymmetry is the fact that the **FCAL** position is shifted by 3mm downwards with respect to the beam axis.

- More energy is observed in the **HAC** cells immediately to the right of the beam pipe than in those immediately to the left. Version **NUM10V3** of the Monte Carlo reproduces this effect but at a lower level. Version **NUM12V1** actually reverses the asymmetry in the **HAC1** cells.
- More energy is observed in the **EMC** cells immediately to the left of the beam pipe than in those immediately to the right. Both Monte Carlo versions reproduce this asymmetry but at a lower level.

One of the reasons for the right/left asymmetry may be the off-centred positioning of the beam pipe flange (near $Z = 214$cm) with respect to the **FCAL** and the **C4** collimator inside the beam hole of the **FCAL** (see section 4.4). The level of this effect appears not to be modelled either in **NUM10V3** or in **NUM12V1**. These two detector descriptions of the forward beam pipe region are shown in figure 4.17. Note that although version **NUM12V1** contains a more detailed description of the forward region, it does no better than version **NUM10V3** in the prediction of the energy asymmetries.

The discrepancy between data and Monte Carlo with regard to these asymmetries is used in estimating the systematic errors.

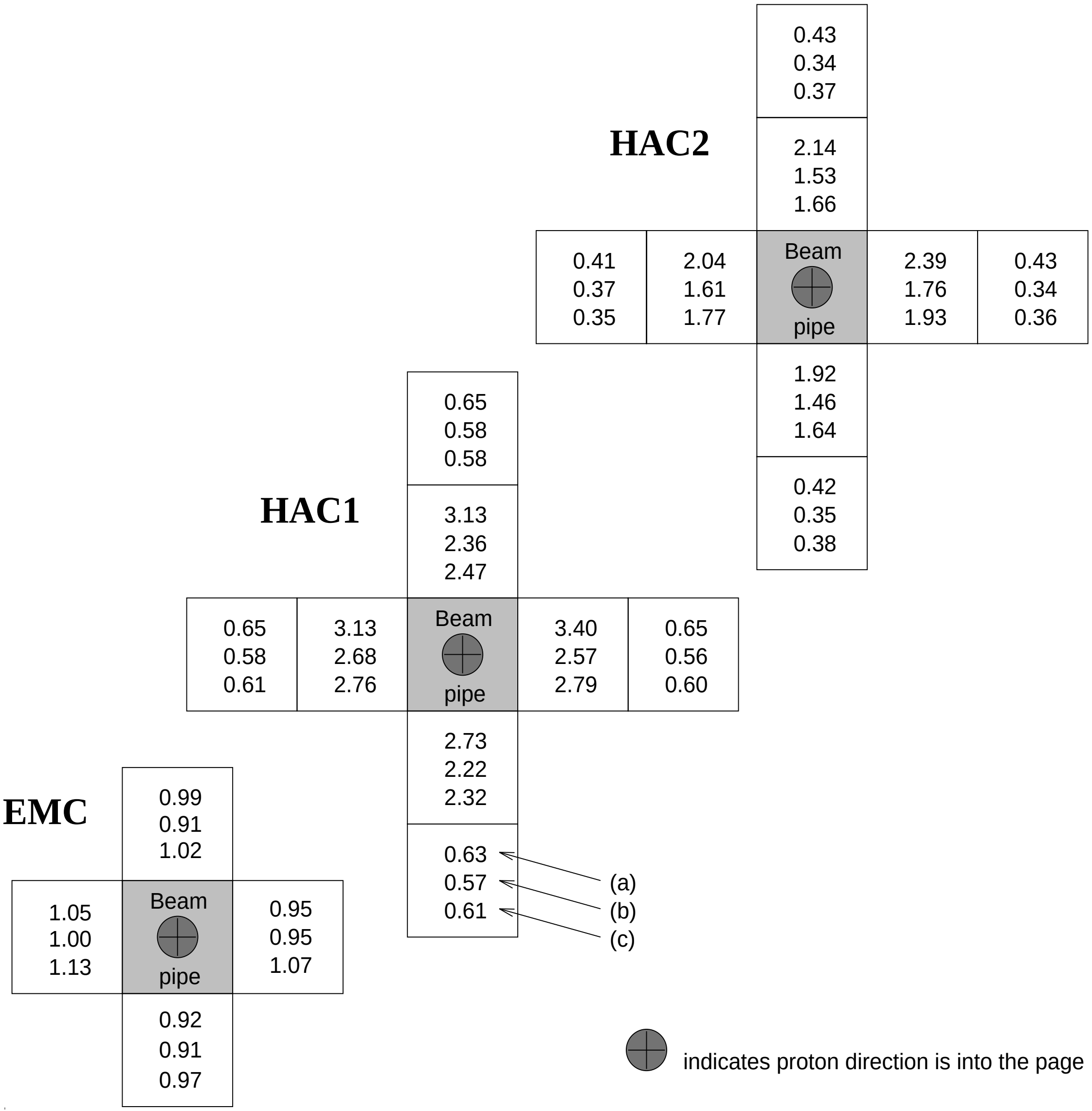

Figure 4.16: *The mean energy (not transverse), in* GeV, *observed and simulated in the* FCAL *cells nearest the beam pipe. 1993 DIS data with timing and imbalance cuts applied (see text) is observed in row (a). Monte Carlo with* NUM12V1 *geometry using* ARIADNE4.03 *is simulated in row (b). Monte Carlo with* NUM10V3 *geometry for the same model is simulated in row (c). Imbalance cuts have also been applied to the Monte Carlo.*

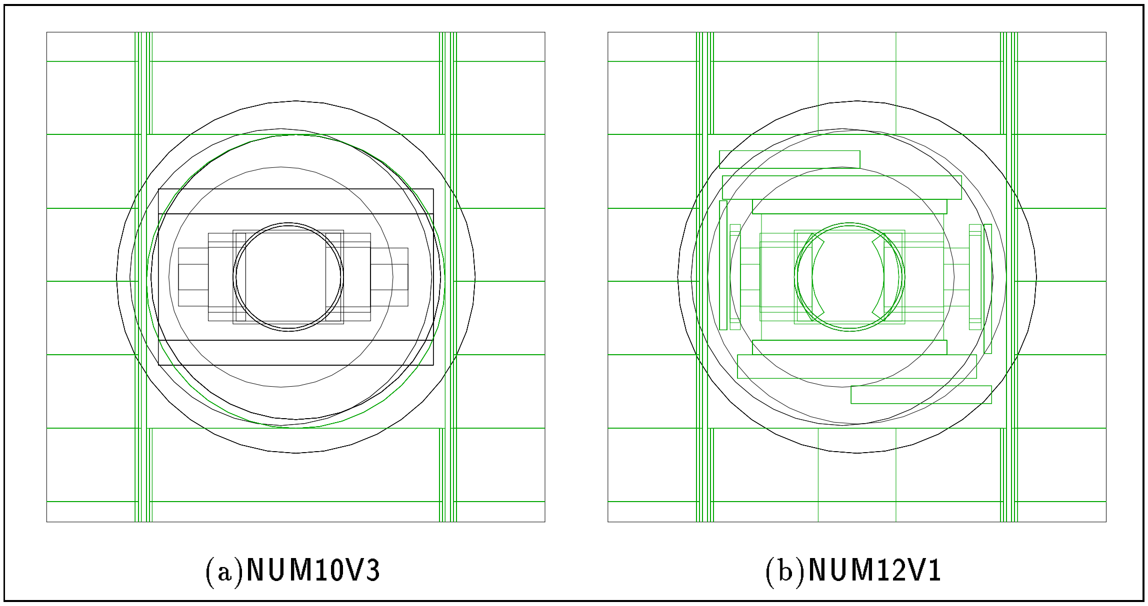

(a)NUM10V3 (b)NUM12V1

Figure 4.17: *End views of the* FCAL *beam pipe region as described by the two simulation versions indicated. The proton direction is out of the page.*

4.5.3 Cerenkov effect in wavelength shifter bars.

Most particles deposit their energy inside the depleted Uranium scintillator sandwich. Some of this energy leaks into the wavelength shifter bars (there are two of these for each cell, one for each photomultiplier tube (PMT)). The energy of the deposit is known via a standard signal-to-energy conversion and this effect is modelled in the Monte Carlo. The calorimeter timing is calibrated in such a way that particles from the nominal interaction point (NIP) generate a signal at $time = 0$ if they interact in this way.

Some particles that hit the wavelength shifters directly at small angles (< 40mrad) may travel a large distance inside the wavelength shifter bars and produce a large signal by the emission of Cerenkov light (figure 4.18b) [5, 50].

This effect is not simulated in the Monte Carlo and is more likely to occur around the beam-pipe cells for two reasons:

1. The sides of the wavelength shifters on the left and right beam-pipe cells are adjacent the beam-pipe and therefore more exposed to particles from the beam-pipe region. They do not have the protection of the Uranium sandwich.

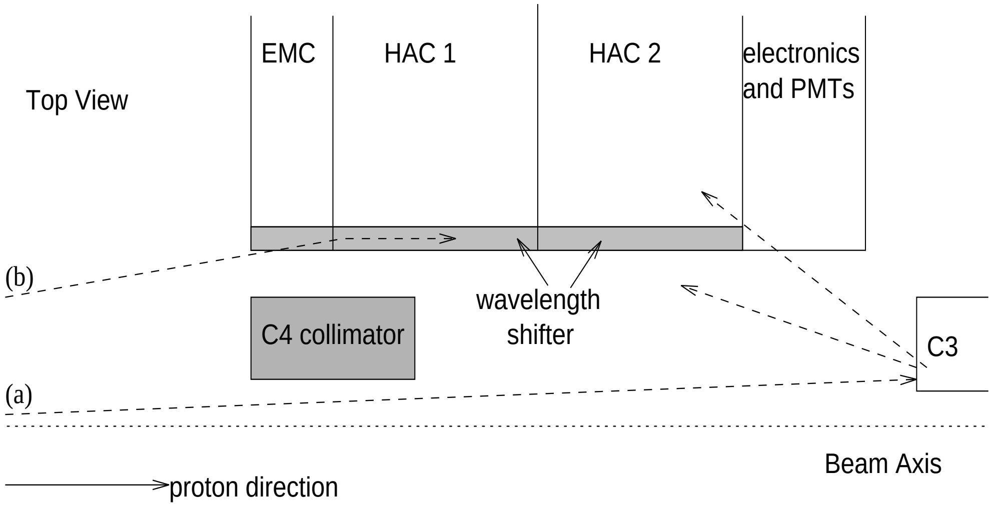

Figure 4.18: *A schematic top view (not to scale) of the* FCAL *cells nearest to the beam pipe. (Only one side of the calorimeter is shown.) Particles travelling along (a) may shower far from the* FCAL *and scattered secondaries can enter the calorimeter with a wide range of incident angles (see section 4.4). Particles within a certain incident polar angle to the* FCAL*, (b), may travel a long way down a wavelength shifter causing Cerenkov light to hit the* PMT *[5, 50].*

2. The range of angles of the wavelength shifter bars in the beam pipe cells (30–50mrad measured from the NIP) is a range still susceptible to particles travelling a large distance down the bars and producing Cerenkov light.

This effect is characterised by large imbalances of the energy measurement between the two PMTs in the hit cell. Imbalance is defined as

$$I_{cell} = \frac{(E_{left} - E_{right})}{(E_{left} + E_{right})} \tag{4.2}$$

<u>Note:</u> The convention here is that "right" and "left" are defined as the positions of the PMTs as viewed from the NIP.

If both wavelength shifters associated with a cell are hit in such a way that Cerenkov light is produced, the value I_{cell} is not predictable. However, the timing signal in the PMTs generated by these hits is somewhat earlier than the showering signals. Figure 4.19a shows the relative difference in PMT times versus cell imbalance for the 1993 DIS data. Figure 4.19b is the same plot taken from [50] for a sample with a much higher beam-gas background where the effect is strongly enhanced.

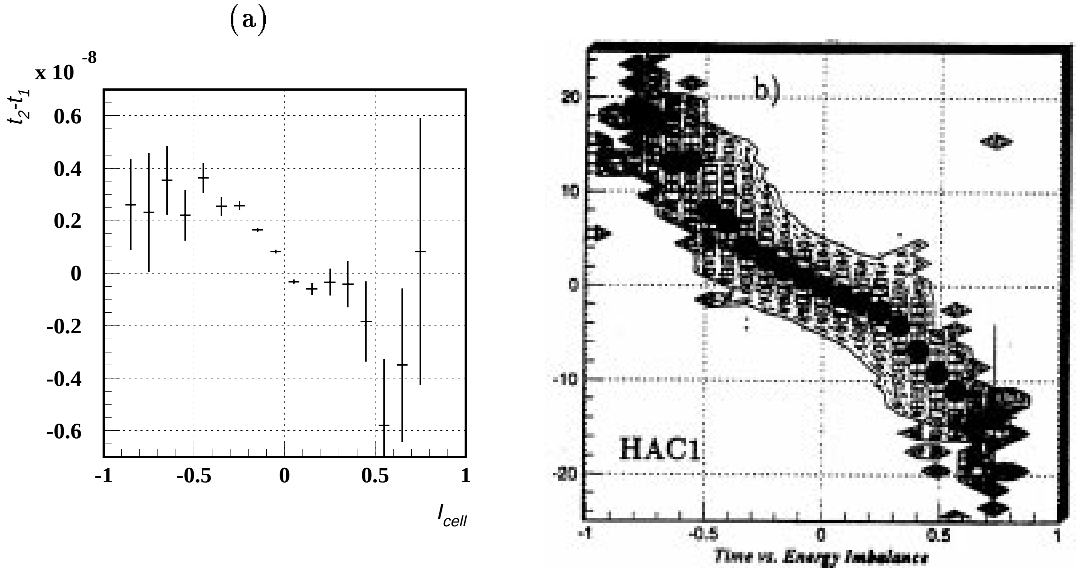

Figure 4.19: *The mean difference in the timings of the* PMT*s (units are* s *in plot (a) and* ns *in plot (b)) plotted against the cell imbalance (equation 4.2). The errors on the plots indicate the width of the mean difference. Plot (b) is taken from [50].*

4.5.4 Timing and imbalance cuts.

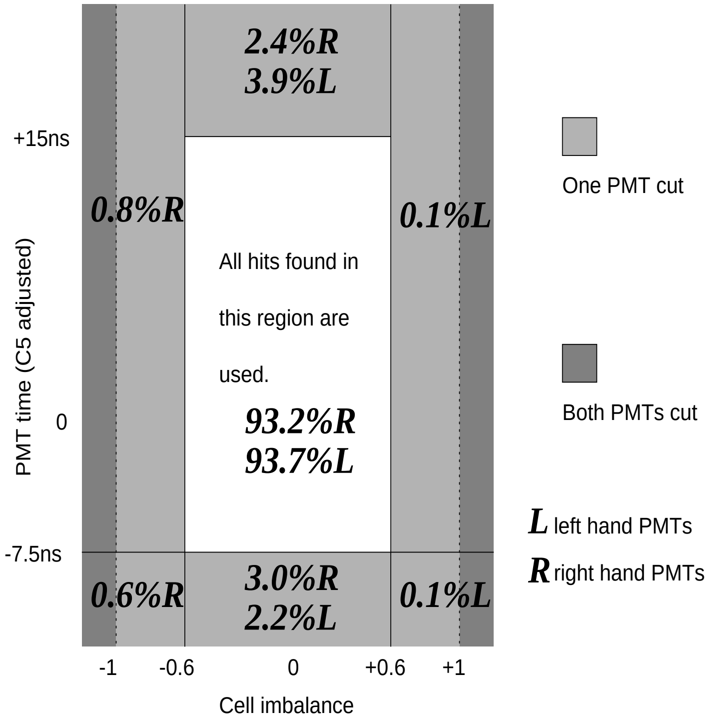

Figure 4.20: *The regions of* PMT *timing and cell imbalance indicating which hits are used in the energy flow analysis and which are not. The time axis is relative to each* PMT*'s mean time. (The timing cuts are not applied to the Monte Carlo but the imbalance cuts are applied.)*

Figure 4.21 shows the observed and simulated timing distributions for all cells in 1993 DIS data and Monte Carlo ARIADNE4.03 with NUM12V1 geometry. Note that the timing is not at all described in the Monte Carlo. An additional observation is the energy spectrum for very late and very early cell hits ($|t| \geq 64$ns) which is continuous in the data but has a discrete spectrum in the Monte Carlo.

Figure 4.22 shows the cell imbalances observed and simulated for the same event samples as above. Note the asymmetric imbalance distribution in the uncut data in (a) which is seen in (b) to come mainly from hits in the beam pipe EMC cells. When a 200MeV cut is placed on the cell energy, the asymmetry in the imbalance distribution disappears, as seen in (c), but the width of the distribution is still not completely modelled in the Monte Carlo.

Figures 4.23,4.24,4.25 and 4.26 show imbalance distributions for 1993 DIS data and Monte Carlo ARIADNE4.03 with NUM12V1 geometry for EMC and HAC cells adjacent the beam pipe. The positions of the tails in the data is simulated but the widths are not, especially in EMC cells. This is not too important, however, since the tails contribute a very small amount ($< 1\%$) to the observed transverse energy flow as can be seen in figure 4.22c,d and also table 4.2.

Timing and imbalance information is used to identify and remove energy deposits in the data which are not modelled in the Monte Carlo.

PMT timing adjustment using the C5 detector

Before the PMT signal times are used in the timing cuts, an adjustment for the position of the vertex and the lateness of the colliding beams is made. Using the method described in detail in [51]:

$$t_{corr} = t + \left[\left(\frac{C_v}{30} - C_l \right) \times 10^{-9} \right] \qquad (4.3)$$

- t_{corr}, t = corrected, observed PMT hit times (s)
- C_v, C_l = vertex Z (cm) and beam lateness (ns) as calculated from the C5 detector timings

(The corrections for 1993 DIS data are typically 2–3ns.)

Note: the polar angle correction to the time of flight is ignored since, in the very forward region, this is negligible.

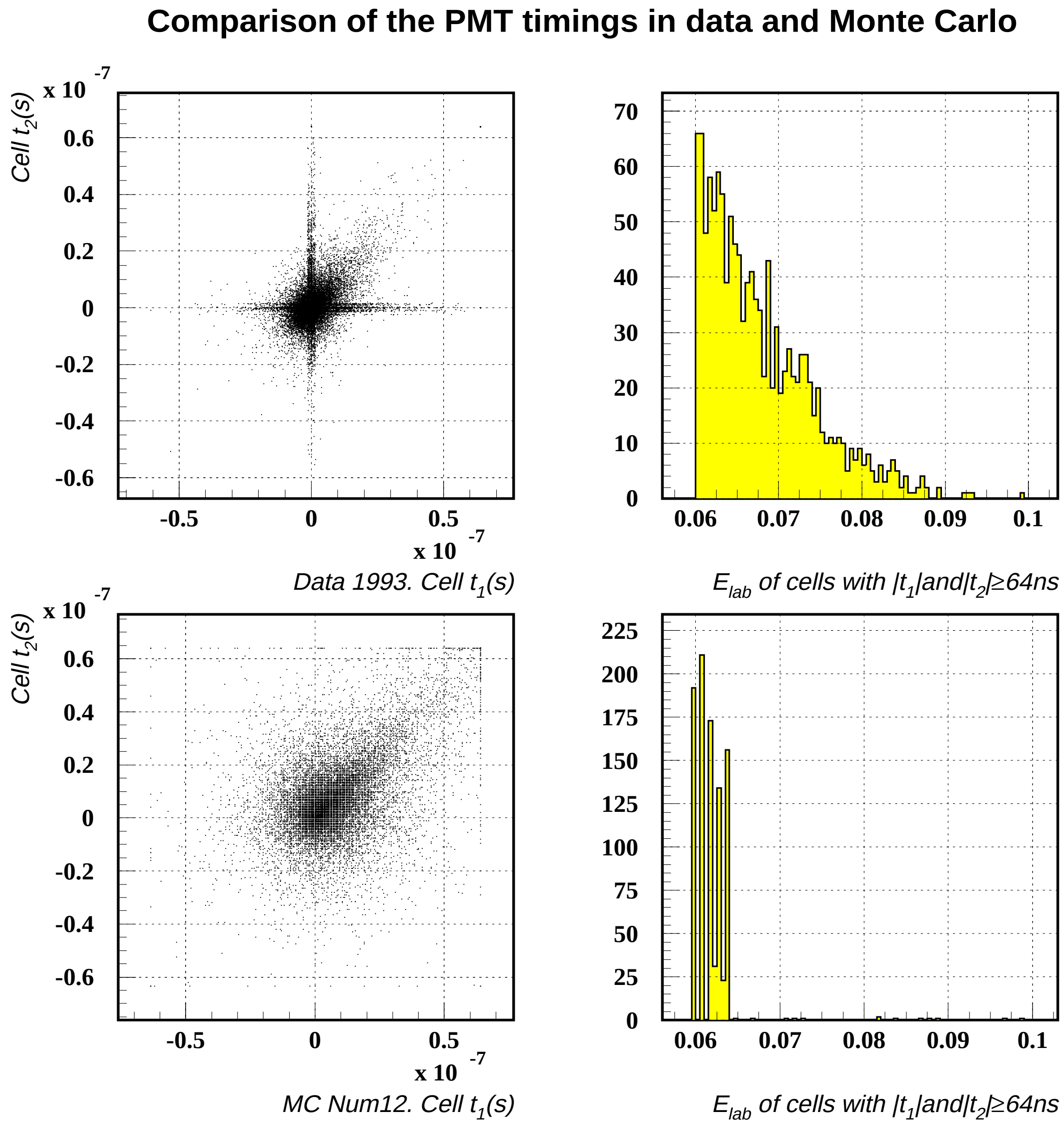

Figure 4.21: *The left–hand plots show the* PMT *timing spectra for 1993 DIS data (top) and* ARIADNE4.03 *Monte Carlo with* NUM12V1 *geometry (bottom). The right–hand plots are the energy spectra of cells whose* PMT *timings are very late or very early (*$|t| \geq 64$ ns*)*

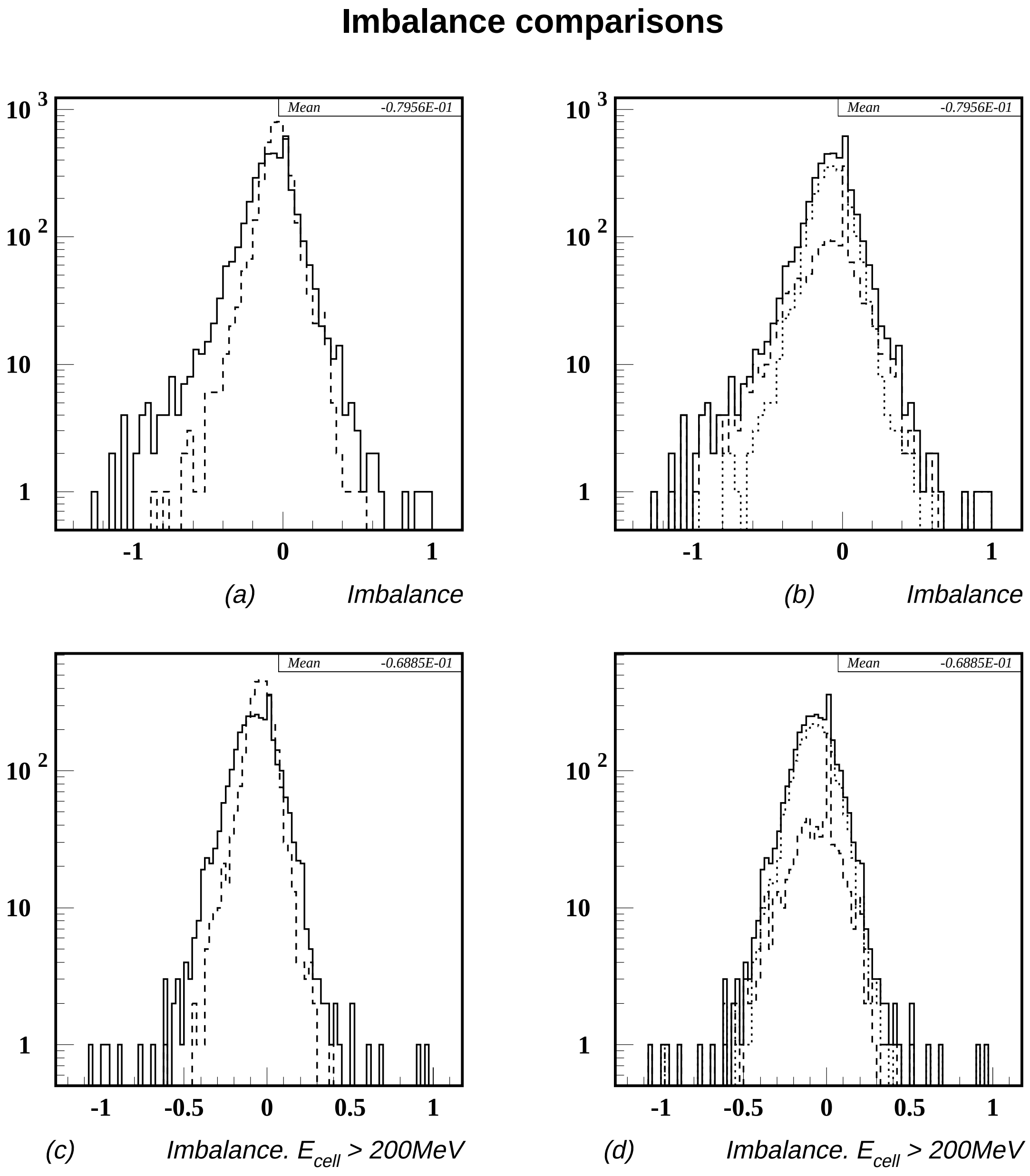

Figure 4.22: *The cell imbalance (equation 4.2) distribution for* FCAL *cells adjacent the beam pipe. The solid histogram in (a) represents the imbalance distribution of all beam pipe cells observed in 800 events from 1993 DIS data. The dashed histogram represents all beam pipe cells simulated in 800 events using* ARIADNE4.03 *with geometry version* NUM12V1*. The plots in (b) are all taken from the observed 1993 DIS data. The solid histogram is (the same as the solid histogram in (a)) for all beam pipe cells, the dashed for* EMC *cells only and the dotted for* HAC *cells only. Plots (c) and (d) correspond to (a) and (b) respectively but with a low energy cutoff ($E_{cell} >$ 200MeV). The contribution of high imbalance hits to the observed energy flow is shown in table 4.2.*

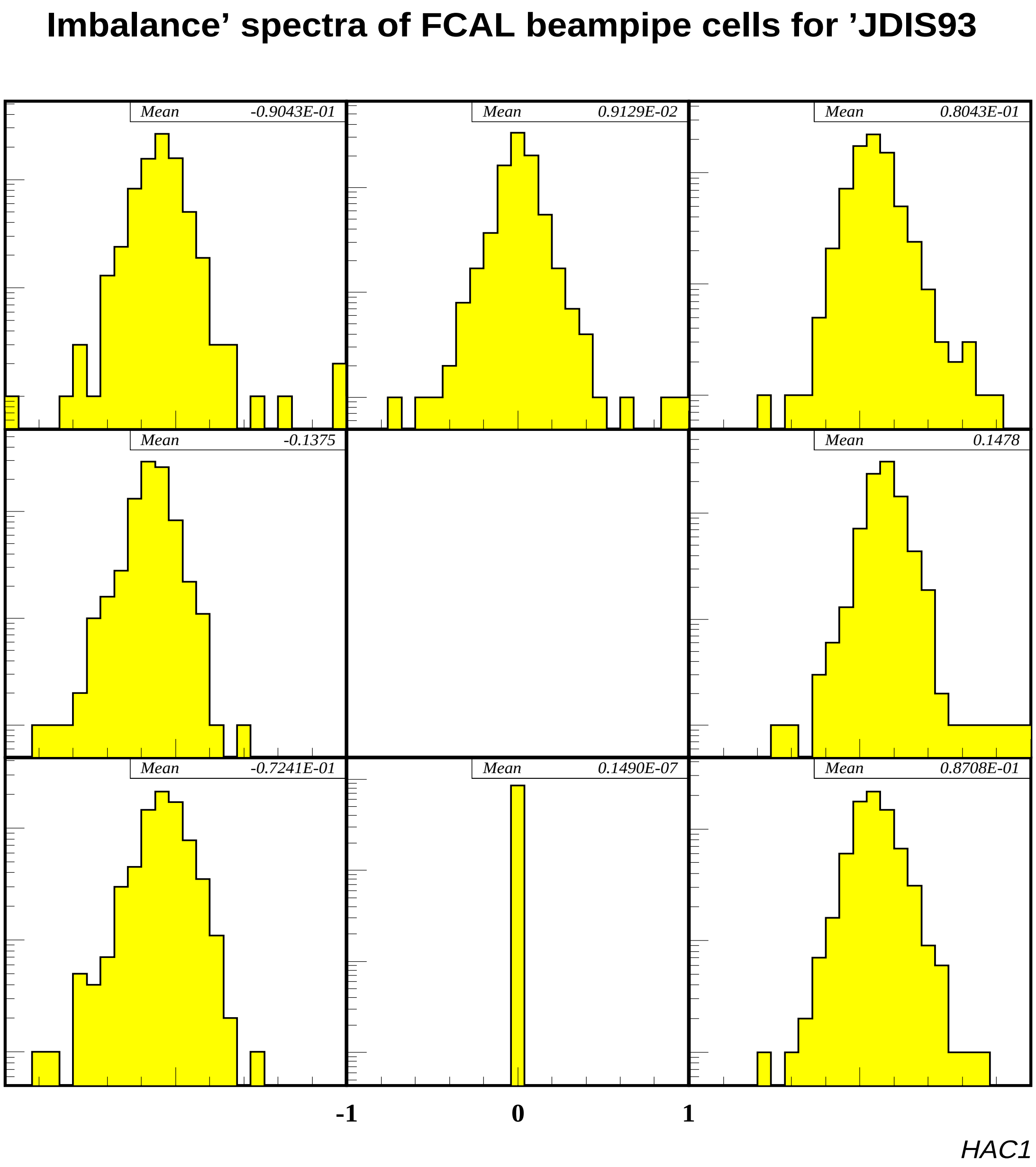

Figure 4.23: *The cell imbalance distribution for all* FCAL HAC1 *cells adjacent the beam pipe observed in 1993 DIS data. The plot for* HAC2 *cells (not shown) is similar. The Y axis is a logarithmic scale. The proton direction is into the page. Note the position of the tails in the left–hand and right–hand plots. The cell below the beam pipe contains a dead* PMT.

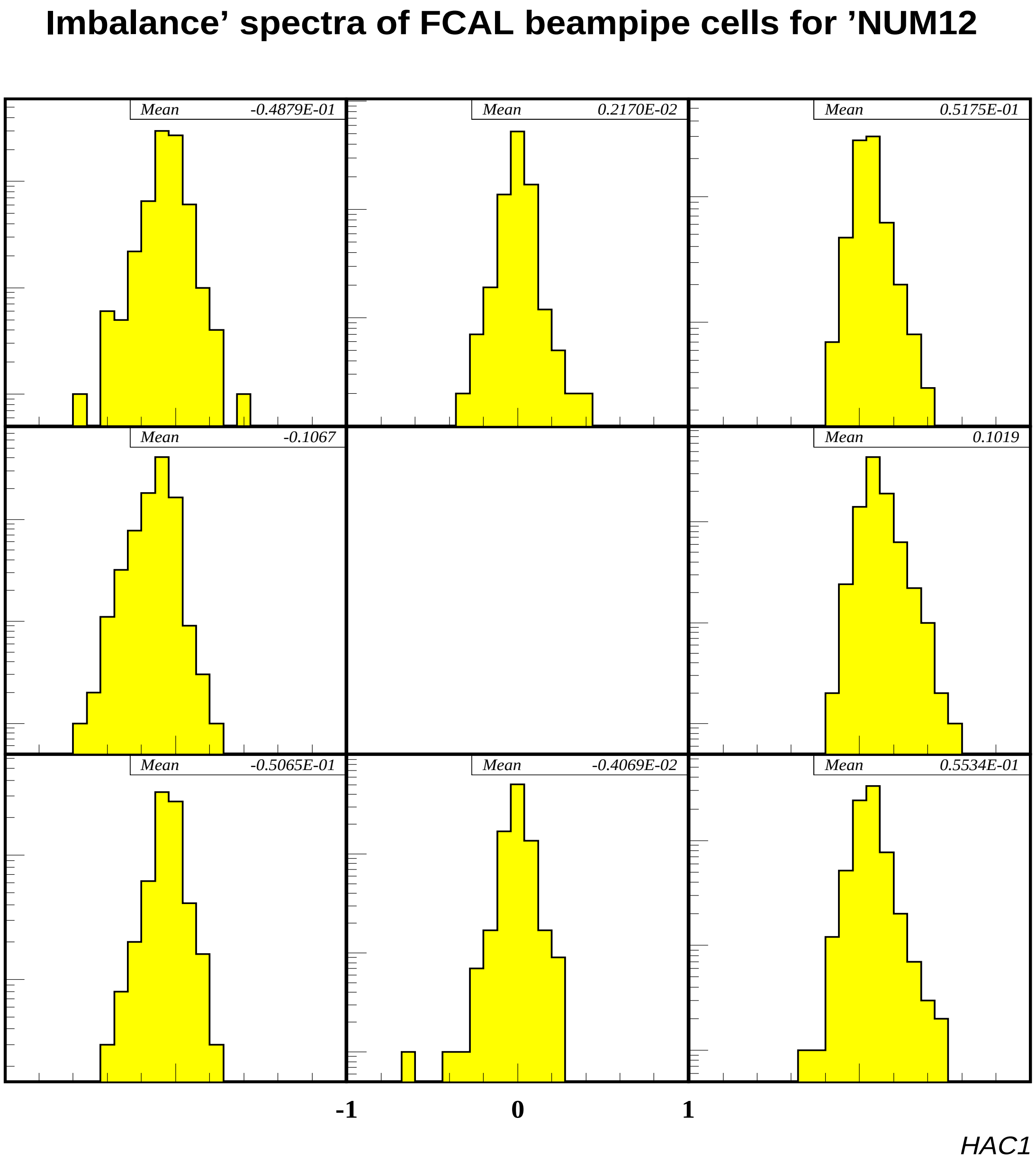

Figure 4.24: *The cell imbalance distribution for all* FCAL HAC1 *cells adjacent the beam pipe simulated in* ARIADNE4.03 *with* NUM12V1, *geometry. The plot for* HAC2 *cells (not shown) is similar. The Y axis is a logarithmic scale. The proton direction is into the page. Note that the positions of the tails in the plots is correctly modelled but the tails are somewhat smaller.*

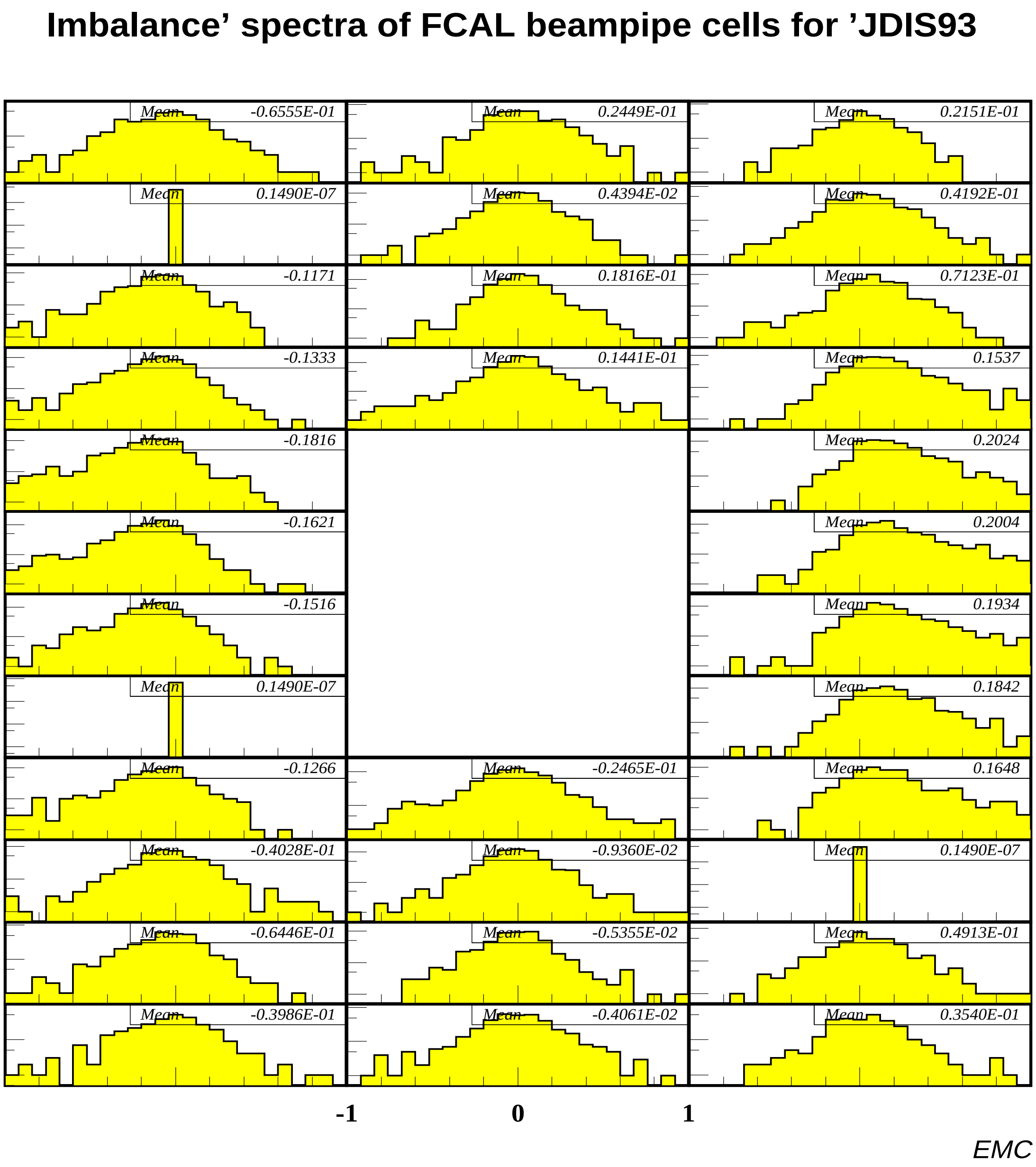

Figure 4.25: *The cell imbalance distribution for all* FCAL EMC *cells adjacent the beam pipe observed in 1993 DIS data. The Y axis is a logarithmic scale. The proton direction is into the page. Note the width and position of the tails in the distributions left and right of the beam pipe hole. The imbalance distribution of cells containing dead* PMT*s is seen as a spike at 0.*

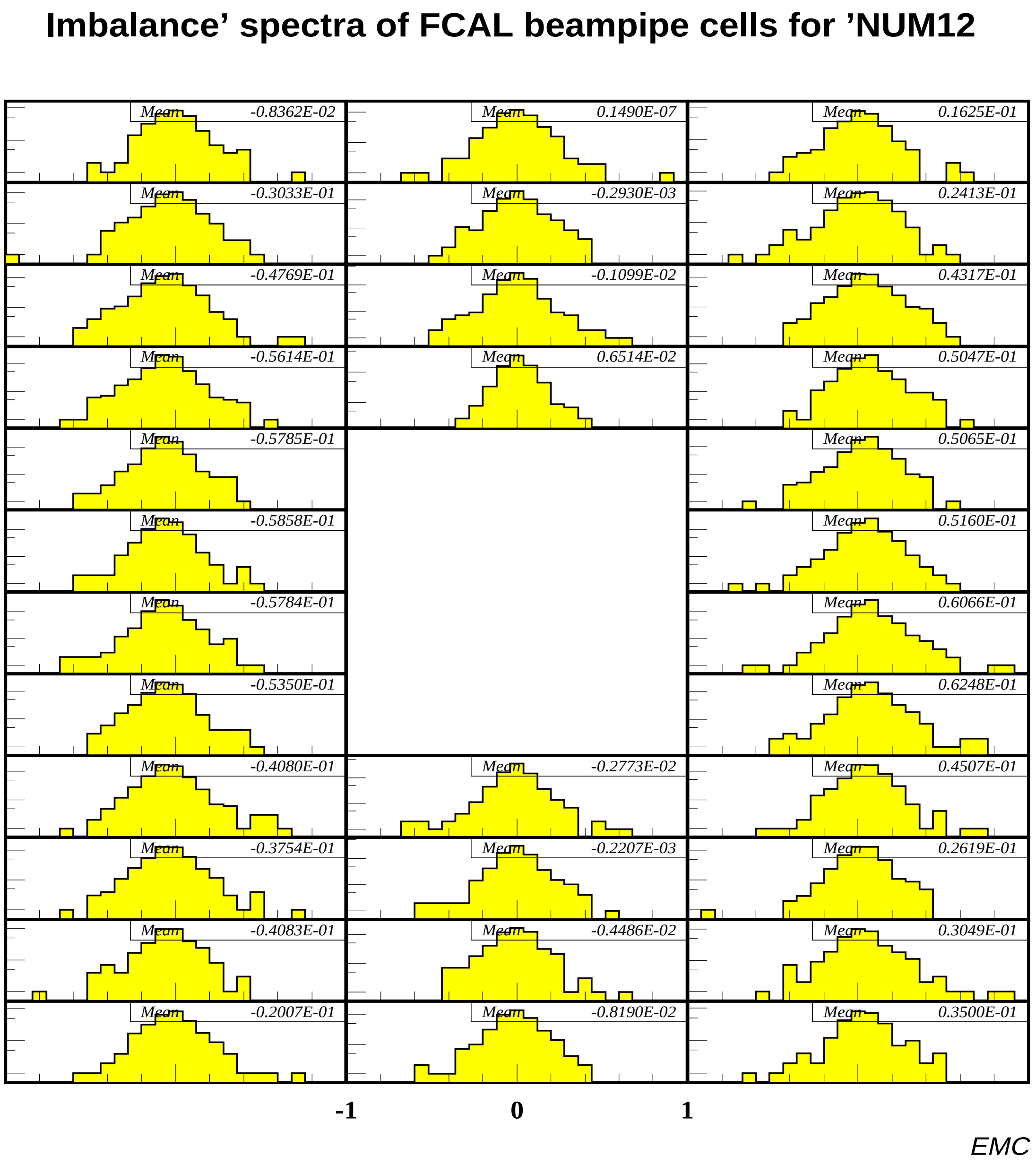

Figure 4.26: *The cell imbalance distribution for all* FCAL EMC *cells adjacent the beam pipe simulated in* ARIADNE4.03 *with* NUM12V1 *geometry. The Y axis is a logarithmic scale. The proton direction is into the page. The position of the tails is modelled but the tails of the distribution are much smaller than those found in the data.*

The position of the cuts

Usually, the energy in a cell is the sum of the energies measured in both PMTs. On an event-by-event basis, some PMTs are excluded from the analysis if any of the following occurs:

1. The recorded hit time in a PMT is more than 7.5ns earlier than the mean time for that PMT. (The mean timings for each PMT are extracted by making a Gaussian fit to the overall distribution of hits with $E_{cell} > 200$MeV. The right–hand PMT timing distributions, as seen from the NIP, in the FCAL EMC cells around the beam pipe are shown in figure 4.27. Note the non-Gaussian tails in the PMTs left of the beam pipe and above the beam pipe where the wavelength shifter bars are directly exposed to low-angle particles.)

   This cut eliminates out-of-time deposits which may stem from Cerenkov hits in the wavelength shifters.

2. The recorded time in a PMT is more than 15ns later than the mean time for that PMT. This cut is designed to exclude deposits from backscattered particles or out-of-time interactions.

3. If the cell imbalance (I_{cell}) is $> +0.6$ then the left–hand PMT is cut. If $I_{cell} < -0.6$ then the right–hand PMT is cut. If $I_{cell} \geq \pm 1.0$ (which can happen in a few cases[1]) then *both* PMTs are excluded from the event. Imbalances $> \pm 0.6$ cannot originate from a particle hitting the depleted Uranium scintillator sandwich but only if a particle hits only the wavelength shifter or a PMT sparks.

For all cells which have had either of their PMTs excluded, the cell energy is set to twice the energy of the remaining PMT. For cells where both PMTs are excluded, the cell energy is set to 0. The range of the above cuts is summarised in figure 4.20.

The result of the cuts

The effect of applying each of the above cuts to the beam pipe cells in the data is shown in table 4.2. Clearly, all the cuts affect only a small proportion of PMTs. The

---

[1] Imbalances$> \pm 1$ may occur. This happens when one of E_{left} or E_{right} becomes negative due to the subtraction of the average calorimeter Uranium noise pedestal from a cell with a very small signal.

Hit selection	%PMTs (right)	$\bar{E}_{right}$	%PMTs (left)	$\bar{E}_{left}$
All hits	100.0	1.10	100.0	1.00
$\lvert I_{cell}\rvert > \pm 0.6$ and $t < -7.5$ns	0.6	0.19	0.1	0.52
$\lvert I_{cell}\rvert < \pm 0.6$ and $t < -7.5$ns	3.0	0.18	2.2	0.18
$\lvert I_{cell}\rvert > \pm 0.6$ and $t > -7.5$ns	0.8	0.09	0.1	0.08
$\lvert I_{cell}\rvert < \pm 0.6$ and $t > 15$ns	2.4	0.06	3.9	0.05
All cuts	93.2	1.14	93.7	1.03

Table 4.2: *A summary of the effect on the* PMT*s in cells adjacent the beampipe in 1993 DIS data when timing and imbalance cuts are applied to these cells. Energy quoted is the mean energy (not transverse) in* GeV *of the* PMT*s.*

energies deposited outside the cut boundaries are small compared to those within.

The candidates for Cerenkov hits which result in high imbalances and/or early timings seem to be at low energies; this is in contrast to earlier findings [50] but note that the event sample in [50] was chosen specifically to enhance this effect. We conclude that Cerenkov hits only contribute a small amount to the observed energy flow.

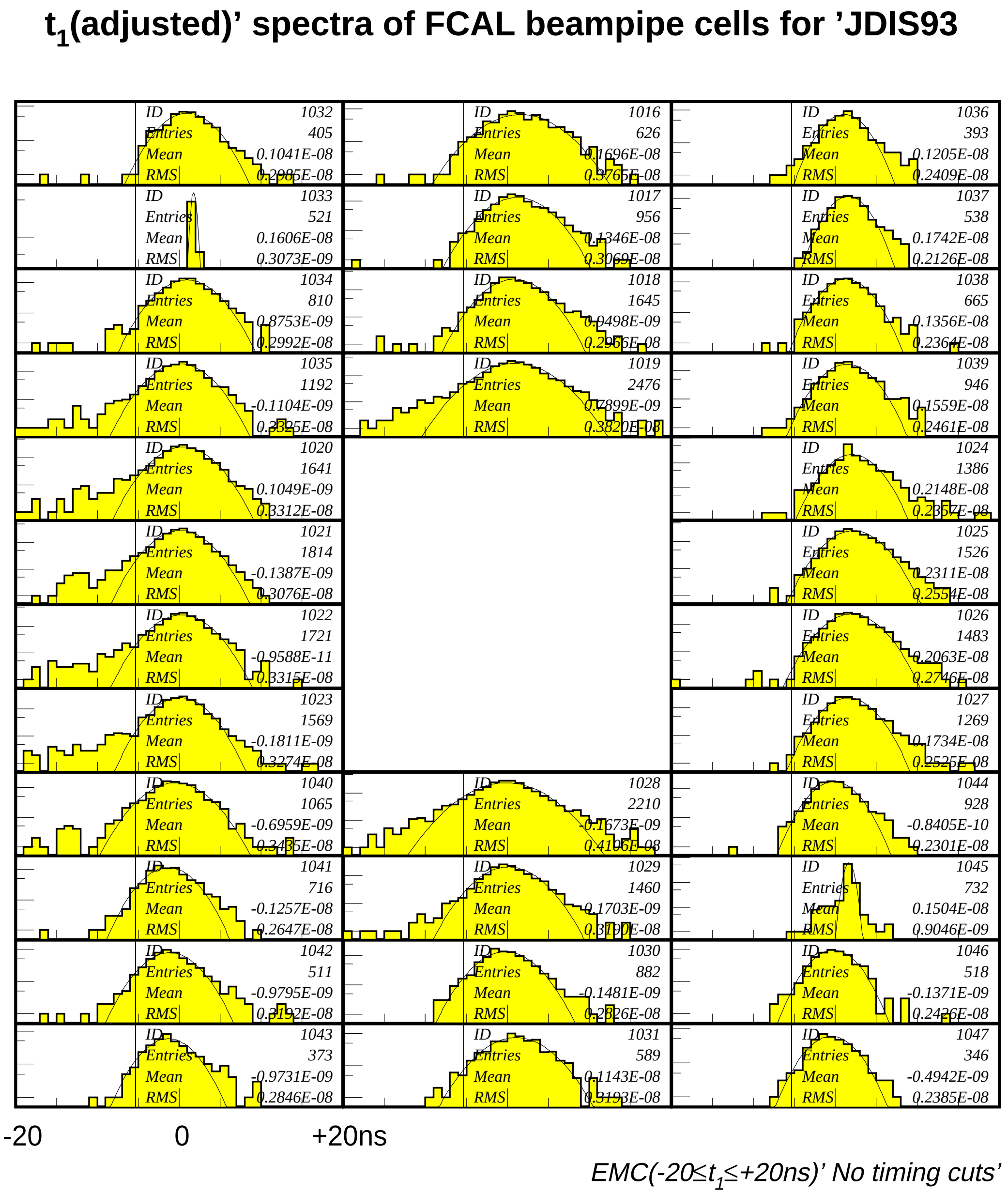

Figure 4.27: *The hit times measured in 1993 DIS data by the right–hand* PMT*s of* FCAL EMC *cells adjacent the beam pipe. Only hits with* $E_{PMT} > 200 MeV$ *and* $|I_{cell}| < 0.6$ *are plotted; the timing for these hits is considered to be well–detemined. The times have been adjusted by the* C5 *vertex and lateness (see text). The* Y*-axis scale is logarithmic. The proton direction is into the page and the view is from the* NIP*.*

4.6 Geometric unfolding.

After discussing the contributions to the observed energy flow which are not modelled by the Monte Carlo, we use the Monte Carlo to unfold the purely geometric effects which *are* modelled.

The geometric correction to the measured energy flow can be separated from the energy losses. In this way, the systematic errors can be isolated and understood more easily.

Due to energy leakage into the calorimeter from particles showering on dead material nearby and due to the degradation of angular resolution in the region $\eta > 2$, a bin-by-bin correction method for the energy flow is not sufficient (see section 5.1). A more general procedure to unfold the geometric effects has been designed for this analysis.

We define the **dispersal coefficients**

$$f^{i,j} = \frac{\epsilon^{i,j}}{\phi^i} \tag{4.4}$$

where ϕ^i is the simulated energy in the ith η bin from the Monte Carlo and $\epsilon^{i,j}$ is the amount of energy which particles generated in bin j have deposited in bin i. (N_i bins $= N_j$ bins). By construction, $f^{i,j}$ is normalised to 1, i.e.

$$\sum_j f^{i,j} = 1 \tag{4.5}$$

$f^{i,j}$ can be interpreted as the probability that energy reconstructed in bin i has been generated at bin j.

In order to unfold back to the hadronic energy flow we fold the dispersal coefficients with the observed energy, τ^i, in each bin i:

$$E^i = \sum_j f^{j,i}.\tau^j \tag{4.6}$$

- E^i is the geometrically-unfolded energy flow in the ith η bin.

In other words, we take each observed energy bin, i, and re-distribute it to the likely true bins, j, from which it originates. This is extended over all observed bins.

In practical terms the procedure works as follows:

1. The simulated energy flow from a standard Monte Carlo sample is extracted (Figure 4.28a). The standard for the 1993 data analysis is the NUM12V1 description of **ZEUS** through which particles from the ARIADNE4.03 generator are tracked from a vertex whose distribution is based on data taken in the summer of 1993. (In the 1994 analysis, ARIADNE4.06 is used with the summer 1994 sampled vertex distribution.)

2. The energy deposited in all cells within a fixed η range is summed. (The assignment of cells to a bin of η is dependent on the vertex which varies from event to event. The overall event vertex distribution must therefore be similar for the data and the Monte Carlo.)

3. Those particles which have hit cells in this η range are found by a navigation through the Monte Carlo data. The 4-vectors of these final state hadrons are now available.

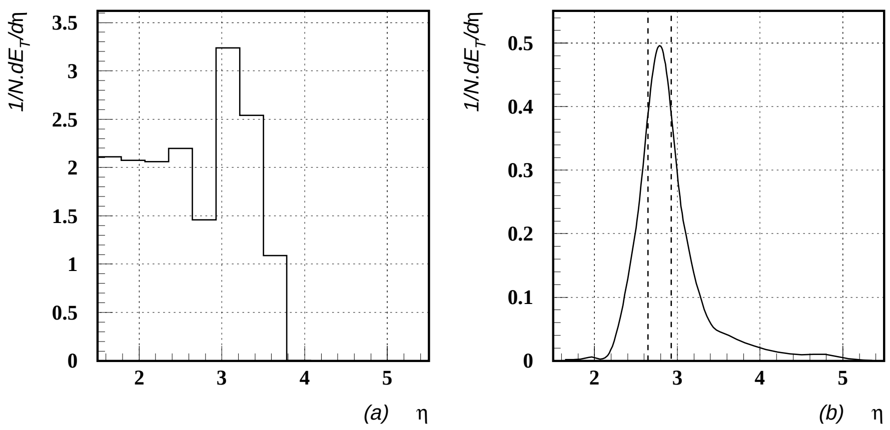

Figure 4.28: *(a) is the simulated energy flow from the* ARIADNE4.03 *Monte Carlo sample using* NUM12V1 *geometry. The solid histogram in (b) is the (not normalised) dispersal function for the range* $2.63 < \eta < 2.92$ *i.e. the energy–weighted angular distribution of particles which have been reconstructed in the range denoted by the dashed lines. Note that this function extends to* η*-values greater than 5 units of pseudorapidity.*

4. The generated η distribution of particles weighted with the transverse energy which each particle deposits in the fixed η range is calculated. Figure 4.28(b) shows an example distribution for a fixed η bin. Figure 4.29(a) shows these distributions for all fixed bins.

5. The distributions are normalised to 1. These are now called the **dispersal functions** and can be envisaged as the probability of the energy measured in a fixed η bin being generated at a second (the same or different) η bin.

6. The geometrically corrected energy flow is obtained by summing the dispersal functions weighted with the observed energy in each respective η bin. The result of this unfolding is shown in figure 4.29(b).

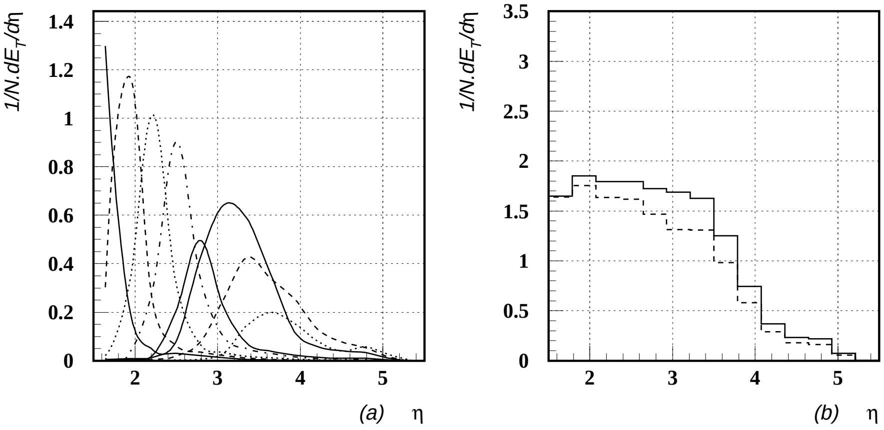

Figure 4.29: *(a) shows the dispersal functions for all fixed η bins. The solid plot in (b) represents the geometrically unfolded energy distribution for the 1993 DIS data sample. The dashed plot in (b) represents the geometrically unfolded distribution for the* ARIADNE4.03 *Monte Carlo sample with* NUM12V1 *geometry.*

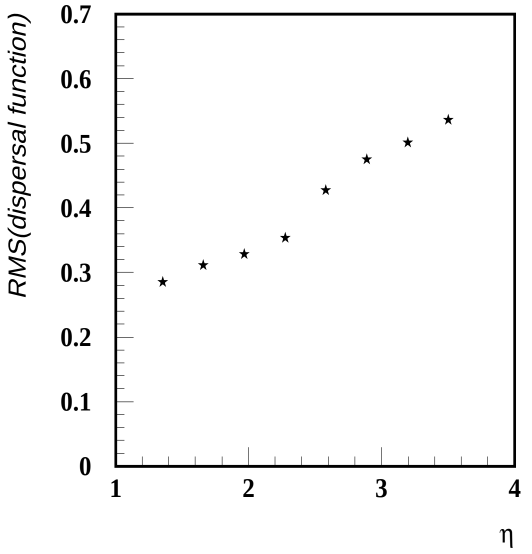

Figure 4.30: *The* RMS *of the dispersal functions which give the effective η resolution for each bin.*

4.7 Systematic errors.

4.7.1 Errors on the observed energies.

Cuts made to the 1993 data are varied and the transverse energy flows from cells re-calculated. The errors shown in table 4.3 indicate the approximate percentage error on the observed energy across the entire η range.

All of the errors (except the statistical one) are considered to be asymmetric when calculating the resultant error values i.e. all positive variations and all negative variations are summed independently in quadrature to yield the final positive and negative variations on the central values. The resultant errors are the quadrature sum of those in the table. The observed energy flow from the data is replotted with the resultant error bars in figure 4.31. Note that the dominant error is the choice of electron finder indicating the different levels of background in the two samples.

Source of error	%error
Statistical	$< \pm 0.5$
Tight timing cuts ($\lvert I_{cell}\rvert < \pm 0.6$ and $-6.75 < t < 15$ns)	< -1
No timing cuts (all I_{cell} and t)	$+1$
Allowing events with $\delta > 33$GeV	$< \pm 0.5$
Only allowing events with $\delta > 40$GeV	$< \pm 1$
Electron finder changed from EEXOTIC→SINISTRA	± 3

Table 4.3: *Effect of the alterations made to the event selection and* PMT *timing on the observed transverse energy flow in the 1993 DIS data.*

4.7.2 Errors on the geometric unfolding.

The energy correction factors and angular dispersal functions are derived from ARIADNE4.03 Monte Carlo geometry version NUM12V1 with the 1993 summer vertex distribution. Those cuts which are relevant to Monte Carlo are applied in the same way as they are applied to the data.

Cuts and event parameters are systematically altered in the Monte Carlo to estimate the resultant systematic error on the angular dispersal functions. The factors are re-calculated and applied to the observed, standard-cut data. To account for the systematic errors on the observed energy flow, the standard Monte Carlo geometric unfolding is applied to the high and low errors found in 4.7.1. These are included in the resultant calculation. Table 4.4 lists the approximate error on the geometrically-unfolded transverse energy flow resulting from each of the checks.

Since the geometric unfolding of the transverse energy flow relies upon the description of the forward region in the Monte Carlo, it is not surprising that the error resulting from the change NUM12V1→NUM10V3 is large (see figure 4.17). Another variation which results in equally-sized errors is the change of input model CDMBGF→MEPS; generator ARIADNE4.03→LEPTO6.1.

The resultant error on the geometrically-unfolded transverse energy flow is the quadrature sum of those checks listed in the table (and the resultant error found in

Description of alteration	What the check determines	%error
vertex $Z \to Z - 1.0$cm vertex $Z \to Z + 1.0$cm	a mismeasurement of the primary vertex	± 1.5 ± 1.5
$E_{cells} \to E_{cells} - 5\%$ $E_{cells} \to E_{cells} + 5\%$	an inconsistent FCAL energy scale in data and Monte Carlo	± 2 ± 2
EEXOTIC→SINISTRA e^- finder $\delta > 33$GeV $\delta > 40$GeV	effect of different event selection	± 2.5 $< \pm 0.5$ $< \pm 1$
Adjust beam pipe cell energies	the effect due to the level of ϕ-asymmetry found in the data	$+2$
NUM12V1→NUM10V3 geometry ARIADNE4.03→LEPTO6.1 generator	the stability of unfolding to a change of forward region description or lower energy flow	± 10 ± 9

Table 4.4: *Approximate systematic errors on the geometrically-unfolded transverse energy flow.*

The Monte Carlo event acceptance with standard cuts in the kinematic range of the 1993 analysis is $\sim 80\%$. Acceptance is defined as accepted events/produced events.

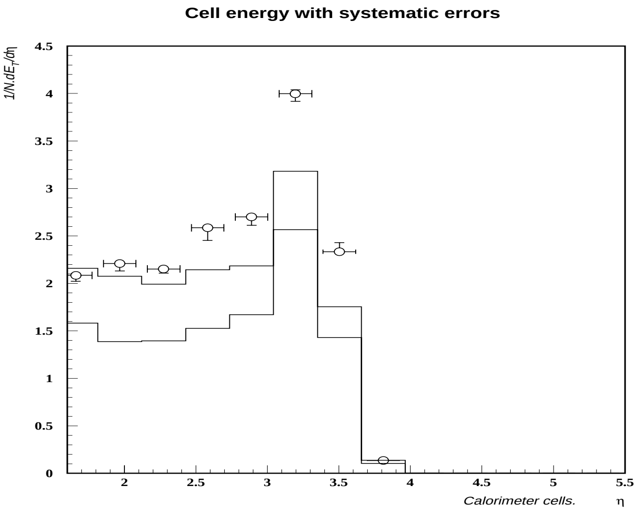

Figure 4.31: *The normalised observed transverse energy flow from calorimeter cells with resultant systematic error bars on the 1993* **DIS** *data points. Simulated Monte Carlo transverse energy flows using* NUM12V1 *geometry for the* ARIADNE4.03 *(CDMBGF, larger histogram) and* LEPTO6.1 *(MEPS, smaller histogram) models are shown for comparison.*

4.7.1). The unfolded transverse energy flow for data with the resultant error bars is shown in figure 4.32.

4.7.3 Energy correction factors.

The energy correction factors are estimated (using the Monte Carlo) by dividing the true transverse energy flow by the geometrically-unfolded transverse energy flow. In practical terms, this is identical to dividing the transverse energy flow as given by the angles and energies contained in the Monte Carlo table of hadron 4-vectors by that calculated by taking energies from the hadronic energy deposited by particles in the calorimeter as predicted by GEANT and angles from the 4-vector table.

The hadronic transverse energy flow in the data is obtained by multiplying the geometrically-unfolded flow by the energy correction factors for each of the checks made in 4.7.2. The acceptance curves for all the checks are obtained independently from the geometric unfolding. These curves are plotted in figure 4.33, superimposed for each systematic check. Note that the Monte Carlo predicts some acceptance in the $\eta > 4.3$ range which is outside the angular coverage of the FCAL as measured

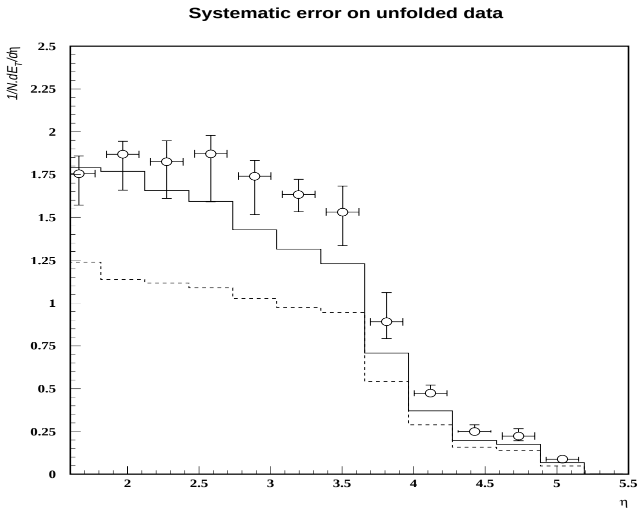

Figure 4.32: *The normalised geometrically-unfolded transverse energy flow with resultant systematic error bars on the 1993 DIS data points. Geometrically corrected Monte Carlo energy flows using* **NUM12V1** *geometry for the* **ARIADNE4.03** *(CDM-BGF, solid histogram) and* **LEPTO6.1** *(MEPS, dashed histogram) models are shown for comparison.*

from the **NIP**. This is due to hadrons showering in dead material in front of the **FCAL** such as the beam pipe flange and the **C4** collimator (see section 4.4).

The error on the hadronic transverse energy flow averaged over all η, from each of these checks, is displayed in table 4.5.

The resultant errors on the hadronic flow are the quadrature sum of the errors from 4.7.2 and the errors on the energy correction factors.

To verify the validity of the unfolding and energy correction procedure, when the calorimeter deposits simulated by **ARIADNE4.03** are unfolded and corrected, the resultant transverse energy distribution is *exactly* the same as the "true" hadronic transverse energy distribution predicted by the Monte Carlo.

Alteration	%error
vertex $Z \to Z - 1.0$cm	±1.5
vertex $Z \to Z + 1.0$cm	±1.5
$E_{cells} \to E_{cells} - 5\%$	+5
$E_{cells} \to E_{cells} + 5\%$	-5
EEXOTIC→SINISTRA e^- finder	±1
$\delta > 33$GeV	< ±1
$\delta > 40$GeV	< ±1
NUM12V1→NUM10V3 geometry	±5
ARIADNE4.03→LEPTO6.1 generator	±5

Table 4.5: *Average systematic errors over the η range of the E_T flow on the energy correction factors.*

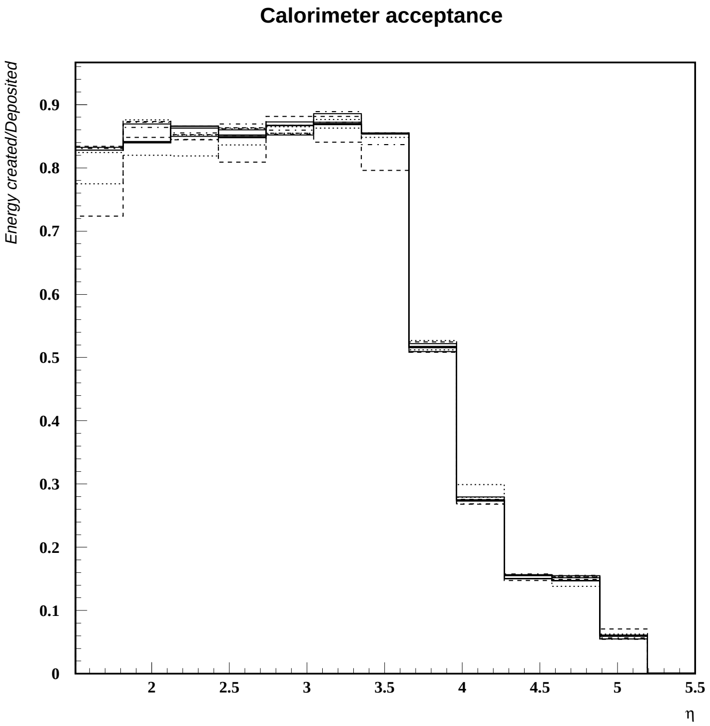

Figure 4.33: *The calorimeter energy acceptance curves (inverse energy correction factors) for the Monte Carlo systematic checks. The largest deviations (dotted and dashed histograms) are seen for* NUM12V1 →NUM10V3 *and* ARIADNE4.03→LEPTO6.1.

4.8 Hadronic E_T flow measured in 1993 DIS data.

BIN	$\bar{\eta}$	RMS(η)	E_T	E_T high	E_T low	% err(high)	% err(low)
1	1.66	0.31	2.12	2.48	1.90	17.07	-10.51
2	1.97	0.33	2.22	2.33	1.92	4.82	-13.60
3	2.28	0.35	2.11	2.32	1.86	10.14	-11.77
4	2.58	0.43	2.20	2.37	1.86	8.00	-15.37
5	2.89	0.48	2.01	2.13	1.74	6.21	-13.09
6	3.20	0.50	1.88	2.00	1.75	6.49	-6.90
7	3.50	0.54	1.79	2.02	1.56	12.43	-12.85
8	3.81	0.60*	1.72	2.05	1.53	19.39	-11.11
9	4.12		1.73	1.91	1.56	10.41	-9.70
10	4.43		1.66	1.91	1.49	15.40	-10.07
11	4.73		1.51	1.83	1.27	20.81	-16.19
12	5.04		1.47	1.87	1.09	27.65	-25.44
13	5.35		1.31	2.19	0.51	67.55	-60.59

The measured transverse energy flow is given in the table and the result is plotted in figure 4.34.

The η resolution comes from the RMS width of the dispersal function for that η bin. These are plotted in figure 4.30. In the bin marked "*", the RMS is not a good measure for the resolution since the dispersal function no longer has a simple, one-peak structure. The resolution quoted in this bin is an estimate from extrapolating an exponential fit to the previous bins.

In bins 9–13 (not plotted), the η resolution is not known and the energy acceptance is small. We choose the final displayed measurement to be at $\eta \approx 4.1$ (η_{high} of bin 8) where the energy acceptance is $\sim 30\%$.

It must be noted that the shape and level of the unfolded and corrected data is dependent upon that of the "true" Monte Carlo distribution which unfolds it. This can be seen from the level of error introduced by using a completely different "true" distribution. The results presented can certainly be used to compare to Monte Carlo to show inconsistencies *but* they do not necessarily represent the *true* transverse energy spectrum.

Care must be taken when comparing to any other theoretical description where an analysis of the data must be iterated using the new description as a "true" distribution.

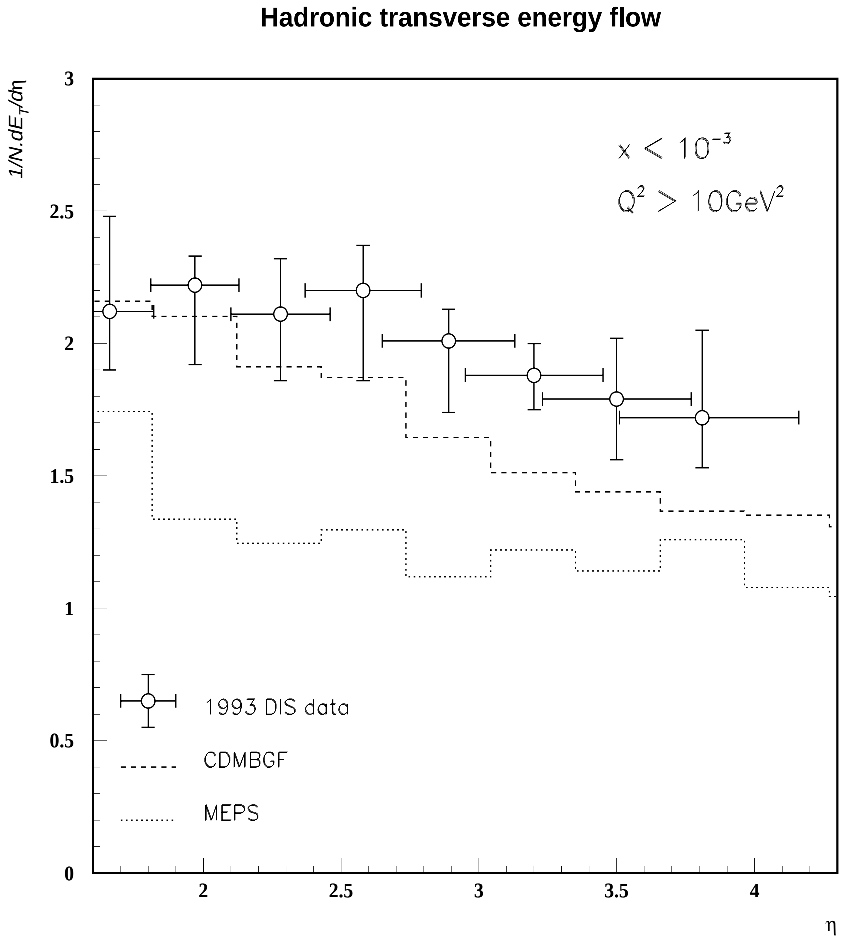

Figure 4.34: *The transverse hadronic energy flow measured in the 1993 DIS data in the kinematic range indicated. The vertical error bars indicate the total systematic error. The horizontal error bars correspond to the η resolution. The statistical error on the points is negligible. Hadronic transverse energy flows from the* ARIADNE4.03 *(CDMBGF, dashed histogram) and* LEPTO6.1 *(MEPS, dotted histogram) generators are shown for comparison.*

Chapter 5

Energy flows throughout phase space.

5.1 Motivation and method

In the previous chapter, it was seen that the statistical error on the transverse energy flow measurement in the central region for 1993 data was negligible.

It was decided that, with the six-fold increase in the number of events which **ZEUS** collected in 1994, the analysis should extend to cover all of the kinematic phase-space available at **HERA** and to cover the entire angular range of the detector.

With the full implementation of the SRTD in 1994, DIS analyses can extend to lower Q^2 with higher accuracy in the determination of the angle and energy of the scattered electron [30].

The kinematic range of a portion of DIS events collected in 1994 is shown in figure 5.1. The data is divided into 24 bins in y and Q^2 represented by the solid lines on the figure. In addition, the kinematic bin used for the 1993 analysis is also included in the 1994 analysis for comparison purposes. The statistical error on the energy flow measurement becomes unimportant when more than a couple of thousand events occupy a bin. An event selection technique is used which stops filling a bin if, say, 2000 events already occupy it. In this way, needless analysis of events is avoided. The structure of the kinematic dispersal of events in figure 5.1 shows the effect of using this method.

In order to correct the energy deposits back to the hadronic final state, the Monte Carlos have been generated from $Q^2 = 4\mathrm{GeV}^2$. This Q^2 is lower than the

Q^2 minimum of the data to correct for migrations due to kinematic reconstruction errors.

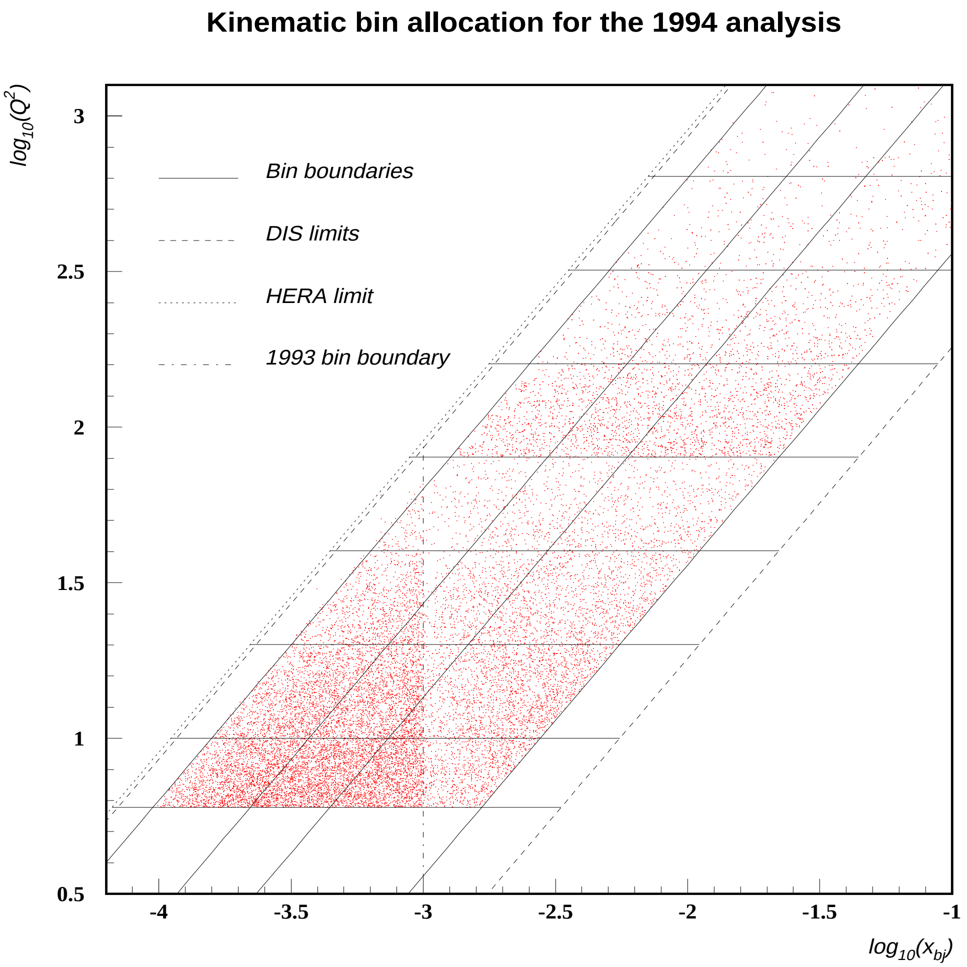

Figure 5.1: *Kinematic distribution of accepted 1994 DIS events.*

Bin	$\bar{x}$	Q^2 range (GeV^2)	$\bar{Q}^2$ (GeV^2)	y range	$\bar{y}$	Accep(%)
1	0.00095	6.0 to 10.0	7.6	0.04 to 0.15	0.089	88.9
2	0.0004	6.0 to 10.0	7.6	0.15 to 0.30	0.213	91.4
3	0.0002	6.0 to 10.0	7.6	0.30 to 0.70	0.415	75.5
4	0.002	10.0 to 20.0	13.7	0.04 to 0.15	0.076	93.7
5	0.0007	10.0 to 20.0	13.5	0.15 to 0.30	0.215	94.8
6	0.0004	10.0 to 20.0	13.7	0.30 to 0.70	0.421	82.4
7	0.004	20.0 to 40.0	27.2	0.04 to 0.15	0.078	96.4
8	0.0014	20.0 to 40.0	27.0	0.15 to 0.30	0.215	98.0
9	0.0007	20.0 to 40.0	26.8	0.30 to 0.70	0.434	81.9
10	0.008	40.0 to 80.0	54.2	0.04 to 0.15	0.077	97.7
11	0.003	40.0 to 80.0	54.3	0.15 to 0.30	0.212	96.4
12	0.0014	40.0 to 80.0	55.1	0.30 to 0.70	0.446	82.1
13	0.015	80.0 to 160.0	107.4	0.04 to 0.15	0.078	96.6
14	0.006	80.0 to 160.0	110.0	0.15 to 0.30	0.212	96.8
15	0.003	80.0 to 160.0	109.2	0.30 to 0.70	0.428	81.9
16	0.029	160.0 to 320.0	211.2	0.04 to 0.15	0.081	95.1
17	0.011	160.0 to 320.0	216.2	0.15 to 0.30	0.209	96.9
18	0.006	160.0 to 320.0	218.8	0.30 to 0.70	0.419	84.3
19	0.062	320.0 to 640.0	450.0	0.04 to 0.15	0.081	94.8
20	0.021	320.0 to 640.0	422.7	0.15 to 0.30	0.218	95.4
21	0.011	320.0 to 640.0	427.5	0.30 to 0.70	0.439	90.9
22	0.10	>640.0	993.1	0.04 to 0.15	0.107	94.9
23	0.06	>640.0	1098.3	0.15 to 0.30	0.211	94.3
24	0.03	>640.0	1250.8	0.30 to 0.70	0.469	92.4

Table 5.1: *The kinematic ranges and means measured in the 1994 analysis bins. Also shown are the event acceptances calculated using* ARIADNE4.06 *with the* NUM12V1 *geometry description.*

The calorimeter cell timing and imbalance cuts are calculated independently and in exactly the same way for the 1994 data as for the 1993 data. The magnitude and position of these cuts (not shown) is almost exactly the same as for the 1993 analysis.

Considering the success of the geometric unfolding method described in the previous chapter, this method is extended to cover the entire η range of **ZEUS** (figure 5.1a). The method is principally the same as for the 1993 analysis.

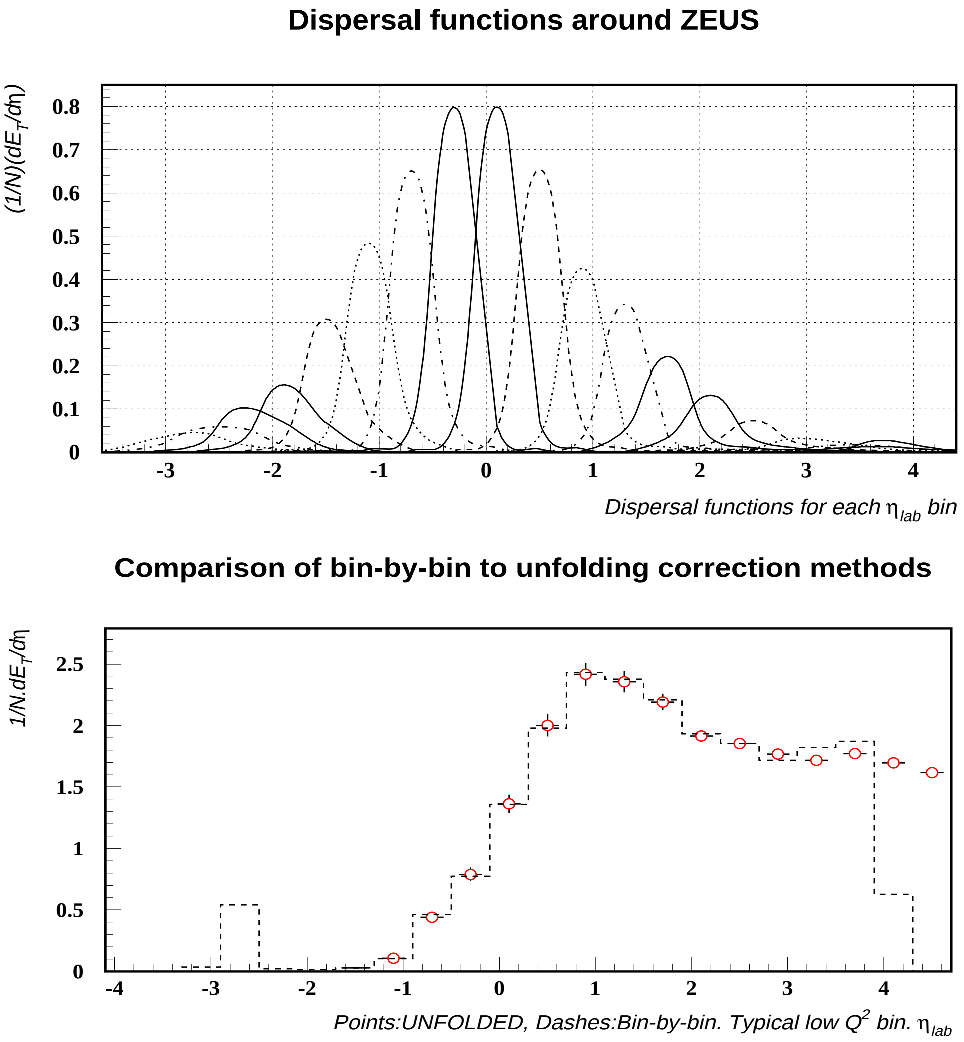

Figure 5.2: *Top plot: dispersal functions for the entire angular coverage of* **ZEUS** *used to correct 1994 data. Bottom plot: comparison of the unfolding method with a standard bin-by-bin correction method in a typical kinematic bin. Note the instability of the standard method in the far-forward region of* **ZEUS**.

5.1.1 Systematic error checking

One conclusion of the 1993 analysis is that there are only a few important sources of error in the measurement of E_T flow. In consequence, a number of error checks can be discounted since their contribution to the overall error is small.

In contrast to the 1993 analysis, the 1994 E_T flows are corrected back to the hadron level with ARIADNE4.06, an updated version of ARIADNE4.03. In addition, the default electron finder is chosen to be SINISTRA as opposed to EEXOTIC since updates in the code have increased its finding purity.

One of the important sources of error is the change in the geometrical description of **ZEUS** used by the Monte Carlo simulation in the far-forward region of the detector (notably the change in the description of the C4 collimator). This type of alteration, used in the 1993 analysis, is not available for 1994 data since there is presently only one version of simulation with the correct vertex distribution (version NUM12V1). An estimate of the magnitude of this error is made for the 1994 data. At $\eta > 2$, $\delta E_T = 10\%$ which becomes $\delta E_T = 15\%$ for $\eta > 4$.

Due to this estimation and the exclusion of the smaller sources of error, the overall error is calculated symmetrically. That is to say, the magnitude of a deviation from the central measured value due to an error check is added in quadrature with the others to produce the overall error. In the 1993 analysis, the positive and negative deviations were considered separately.

The following table is a list of the magnitude of error found by each of the checks made on the 1994 data:

Source of error	Error at high Q^2	Error at lowQ^2
Geometric	as above	as above
Model ARIADNE4.06 → LEPTO6.1	±5%	±8%
Event selection, $E_e'(10 \rightarrow 8\text{GeV})$	±1%	±7%
Event selection, $\delta(35 \rightarrow 33)$	±1%	±7%
E_e' finder SINISTRA → EEXOTIC	±3%	±12%
Overall	±10%	±20%

As can be seen clearly, the background contribution of photoproduction events becomes important at low Q^2.

5.2 Diffractive events

5.2.1 Description

In the data, we observe a substantial fraction of events which have a very low energy in the **FCAL** (figure 5.3a). They are not observed in the prediction of the LEPTO simulation. The events are clearly classifiable as DIS but lack energy in the $\gamma^* p$ central region.

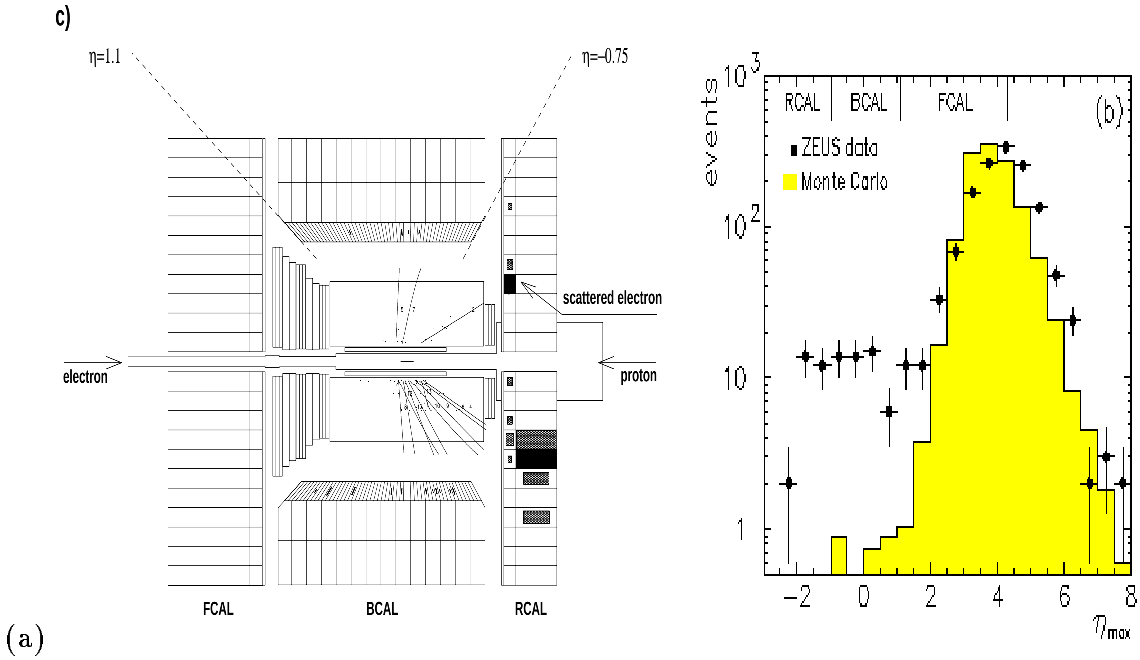

Figure 5.3: *(a) A large-rapidity gap event seen in* **ZEUS**. *(b) The* η_{max} *distribution for data and* LEPTO *Monte Carlo. Both plots come from [52].*

We can define the variable η_{max} as the pseudorapidity of the hadronic cluster closest to the proton beam axis in the forward region. To eliminate noise, this cluster is required to have an energy of at least 400MeV. A cut on this variable makes some distinction between the normal DIS events and these other, large-rapidity gap or *diffractive*, events [52].

The LEPTO generator produces a negligible number of events with $\eta_{max} < 1.5$ (figure 5.3b) unlike the distribution observed in the data. This cut, used in the 1993 E_T flow analysis, strongly reduces the diffractive events' contribution to the energy flows.

More useful than simply disregarding diffractive events is their extraction and analysis. It is thought that diffractive scattering is caused by the exchange of a colourless object, the *pomeron* (denoted $\mathcal{P}$), between the incident proton and the hard-scattering ($\gamma^* q/\bar{q}$) vertex. There is no consensus as to what partonic constitution of the pomeron is but its structure function has been measured [53]. A diffractive process is represented in figure 5.4b. The scattered proton can either break apart or not (since the pomeron is a colourless object, the proton can simply lose momentum and remain stable by its exchange).

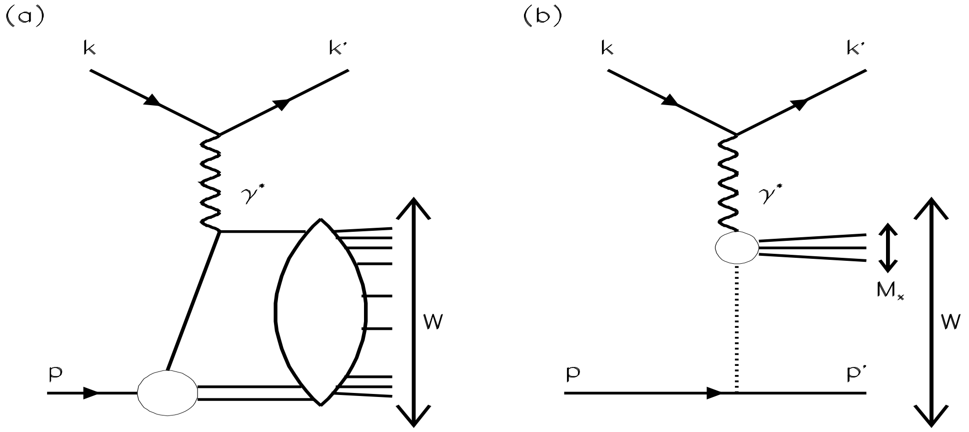

Figure 5.4: *A schematic representation of the normal DIS process, (a), and the diffractive DIS process, (b). The pomeron exchange is denoted by the dotted line.*

In diffractive events, the visible invariant mass in the detector, M_x, is equal to the mass of the $\gamma^* \mathcal{P}$ system. This is small compared with the invariant mass of the $\gamma^* p$ system, W.

It is useful to separate diffractive events according to the variable $x_{\mathcal{P}}$ (x_{pom}). $x_{\mathcal{P}}$, defined similarly to x_{bj}, is the 4-momentum of the proton carried by the pomeron. It can be evaluated using the expression

$$x_{\mathcal{P}} = \frac{(M_x^2 + Q^2)}{(W^2 + Q^2)} \tag{5.1}$$

and it is easy to see that diffractive events will have small values of $x_{\mathcal{P}}$.

Figure 5.2.1a shows the proportionality between $x_{\mathcal{P}}$ and η_{max}. In the following investigation, the dependence of the transverse energy flow is studied as a function of $x_{\mathcal{P}}$.

Unlike **LEPTO**, **ARIADNE** contains a simulation of diffractive events. Figure 5.2.1b shows the distributions of $x_{\mathcal{P}}$ as seen in the data and as predicted by **ARIADNE4.06**. Clearly, the model does not describe the number of diffractive events adequately[1]. Quantitatively, the proportion of diffractive events measured as a function of event kinematics is shown in table 5.2.

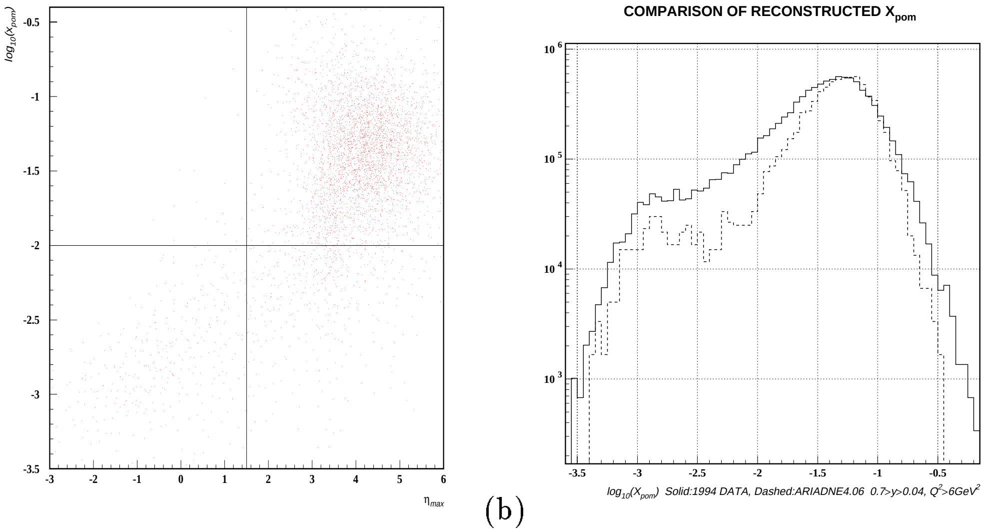

(a) (b)

Figure 5.5: *(a) The proportionality between* $x_{\mathcal{P}}$ *and* η_{max} *measured in 1994 DIS data. The top right-hand corner contains normal DIS events. The two lines show the cutoffs for 1993 data* ($\eta_{max} > 1.5$) *and 1994 data* ($x_{\mathcal{P}} > 0.01$). *(b) The* $x_{\mathcal{P}}$ *distribution measured in 1994 data and predicted by* **ARIADNE4.06**. *The peaks of these plots are normalised to compare the relative proportions of diffractive events. Note that the scale is logarithmic.*

5.2.2 Diffractive energy flows

The correction method to obtain the hadron-level E_T flows for diffractive events is exactly the same as for other DIS events. Figure 5.6 shows the E_T flows in two different kinematic regions. 1994 data and **ARIADNE4.06** are compared. Note that, as well as the poor description of the relative number of diffractive events to normal DIS events, the peak positions and shapes of the flows are different.

---

[1] There exist some dedicated diffractive event generators such as NIKZAK[63] and POMPYT[62]. These describe the diffractive component of ep scattering much more adequately.

As mentioned earlier, the lack of transverse energy flow in the $\gamma^* p$ central region is confirmed. Only the current jet remains visible. The pomeron exchange picture of diffractive events predicts that this jet contains three regions analogous to the $\gamma^* p$ interaction: the struck quark jet, the $\gamma^* \mathcal{P}$ central region and the $\mathcal{P}$ remnant. Since $x_{\mathcal{P}} < 0.01$, there is insufficient energy to resolve these regions [55].

The level of E_T flow in the central region is raised by the same proportion of diffractive events excluded from the full sample.

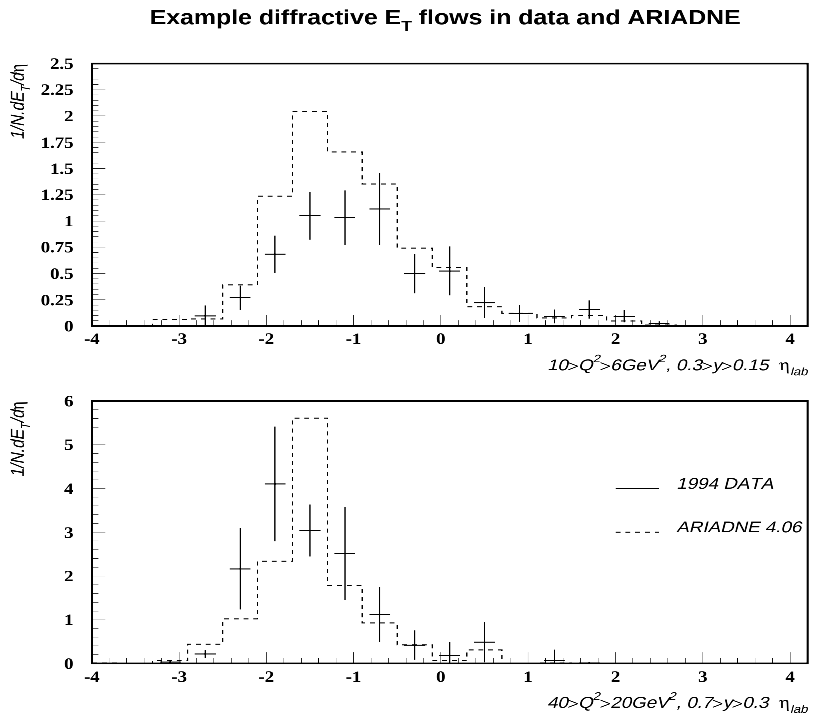

Figure 5.6: *Hadron-level E_T flows in two kinematic bins for diffractive events (events with $x_{\mathcal{P}} < 0.01$). The systematic and statistical error, added in quadrature, is shown on the data plot.*

Bin	1994	ARIADNE	Bin	1994	ARIADNE	Bin	1994	ARIADNE	
1	20.0	12.7	2	30.3	13.7	3	26.3	9.2	$\Downarrow$ Increasing Q^2 $\Downarrow$
4	13.3	8.7	5	22.1	9.9	6	21.1	9.6	
7	5.5	7.8	8	12.1	7.9	9	16.6	8.0	
10	1.9	6.2	11	7.6	8.0	12	14.1	7.8	
13	$\sim$0	2.5	14	2.6	5.3	15	7.0	3.6	
16	$\sim$0	1.8	17	$\sim$0	1.6	18	4.9	3.7	
19	$\sim$0	$\sim$0	20	$\sim$0	$\sim$0	21	1.7	3.3	
22	$\sim$0	$\sim$0	23	$\sim$0	$\sim$0	24	$\sim$0	$\sim$0	

$\Longrightarrow$ Increasing y $\Longrightarrow$

Table 5.2: *The % of events with* $x_{\mathcal{P}} < 0.01$*: the measured diffractive component. The statistical errors on the data measured in 1994 are* $\approx 0.1\%$ *and those on* ARIADNE4.06 *are* $\approx 0.2\%$*. In the 1993 bin (*$x < 10^{-3}, Q^2 > 10 GeV^2$*), the 1994 data diffractive component is measured at* 21.0% *and the* ARIADNE *component at* 9.5%*.*

5.3 Results of the 1994 analysis

Figure 5.7 shows the measurements obtained for the 1994 data E_T flow analysis. The top plot indicates the effect of two different cuts on $x_{\mathcal{P}}$. As expected, a cut at $x_{\mathcal{P}} > 0.01$ increases the average energy in the $\gamma^* p$ central region as diffractive events are excluded. The cut at $x_{\mathcal{P}} > 0.02$ starts to remove normal DIS events which causes the unpredicted drop in E_T flow. This comparison confirms the lower cut on $x_{\mathcal{P}}$ as the more useful diffractive event discriminator.

Included in the lower two plots of figure 5.7 are the comparisons of E_T flows from three physics generators. Two of the generators have been described earlier and the third, HERWIG5.8, is described fully in the manual produced by its author [56]. In basic terms, HERWIG is a general-purpose event generator for high energy processes with particular emphasis on the detailed simulation of parton showers. Colour coherence between inital and final state partons is included as is soft gluon interference within jets. The hadronisation model used by HERWIG differs from the stretched-string approach used by LEPTO and ARIADNE: the HERWIG model involves clustering together partons below a threshold energy which then form hadrons. The default settings of the HERWIG program, without the incorporation of a special "soft underlying event" feature, have generated events whose energy flow is shown in the figure.

At high-Q^2, all the generators describe the position and height of the current jet region. HERWIG5.8 and LEPTO6.1 fail to reproduce the level of E_T flow further forward in **ZEUS** whilst ARIADNE4.06 predicts the level of the far-forward flow but not the level immediately forward of the current jet region.

At low-Q^2, the level of the current jet region measured in the data is almost predicted by LEPTO6.1. Neither ARIADNE4.06 nor HERWIG5.8 predict this level. ARIADNE4.06 again over-estimates the E_T level and HERWIG5.8 predicts a much lower level. Further forward, only ARIADNE4.06 reproduces the E_T flow level measured in the data. The other two models lack transverse energy in this region.

Figures 5.8 and 5.9 show the non-diffractive E_T flows ($x_{\mathcal{P}} > 0.01$) in all 1994 kinematic bins. The data points show the systematic and statistical error added in quadrature. The horizontal η axis ranges from -4.1 to 5.5. Since the detector acceptance is very low at $\eta > 4.5$, points further forward are only useful as a guide.

Note how the prediction of the CDMBGF model is much closer to the data, except in the region slightly further forward of the current jet. The MEPS model does not describe the data at all well in the γ^*p central region, especially at low-Q and low-x.

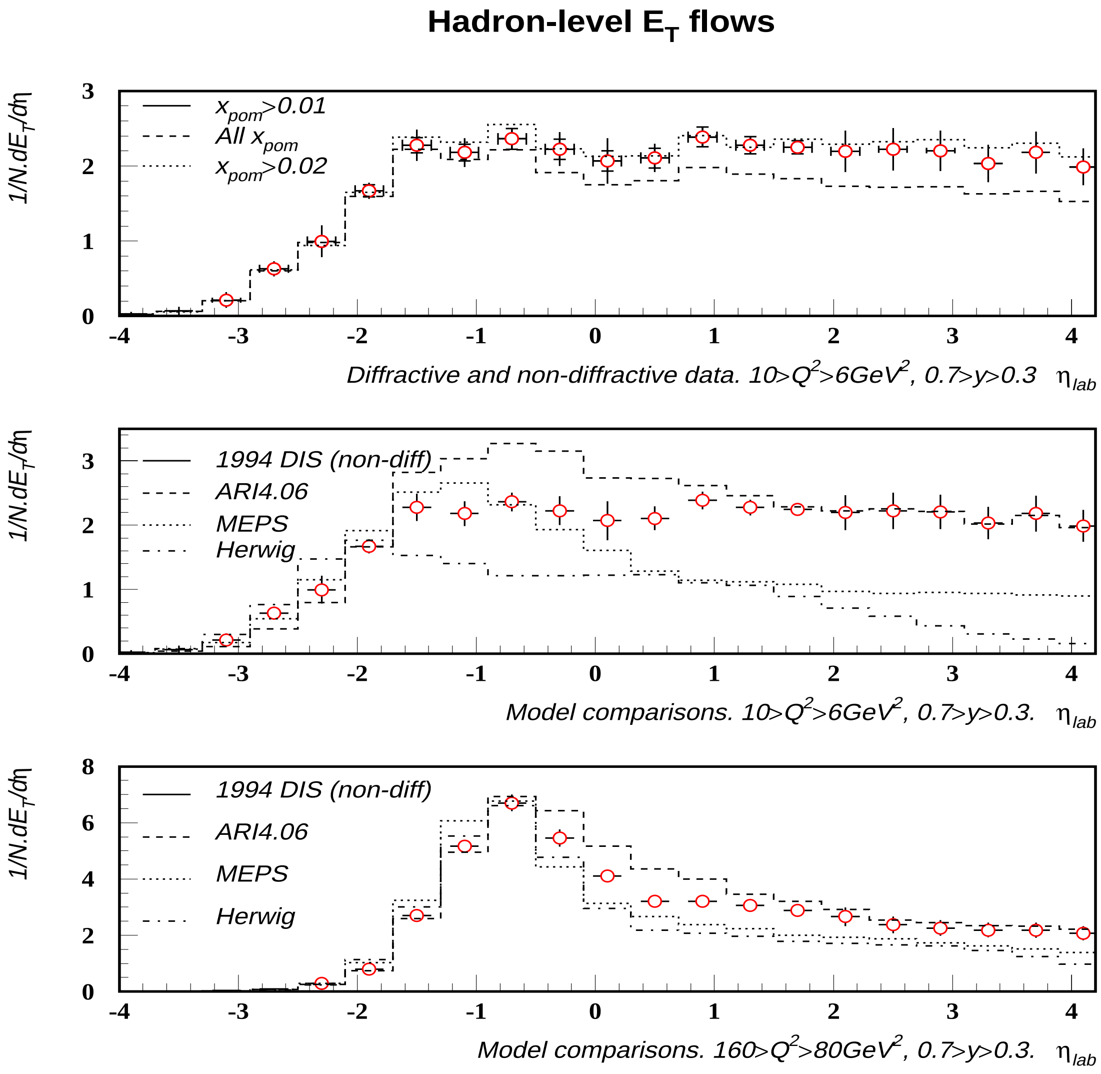

Figure 5.7: *The top plot shows the effect, in a particular kinematic bin, of two cuts in* $x_{\mathcal{P}}$ *on the hadron-level* E_T *flow measured in 1994 data. The two lower plots give a comparison of the data with non-diffractive* E_T *flows predicted by three popular physics generators. Statistical errors are shown as horizontal bars in the top plot. Full errors are shown in all plots as error bars.*

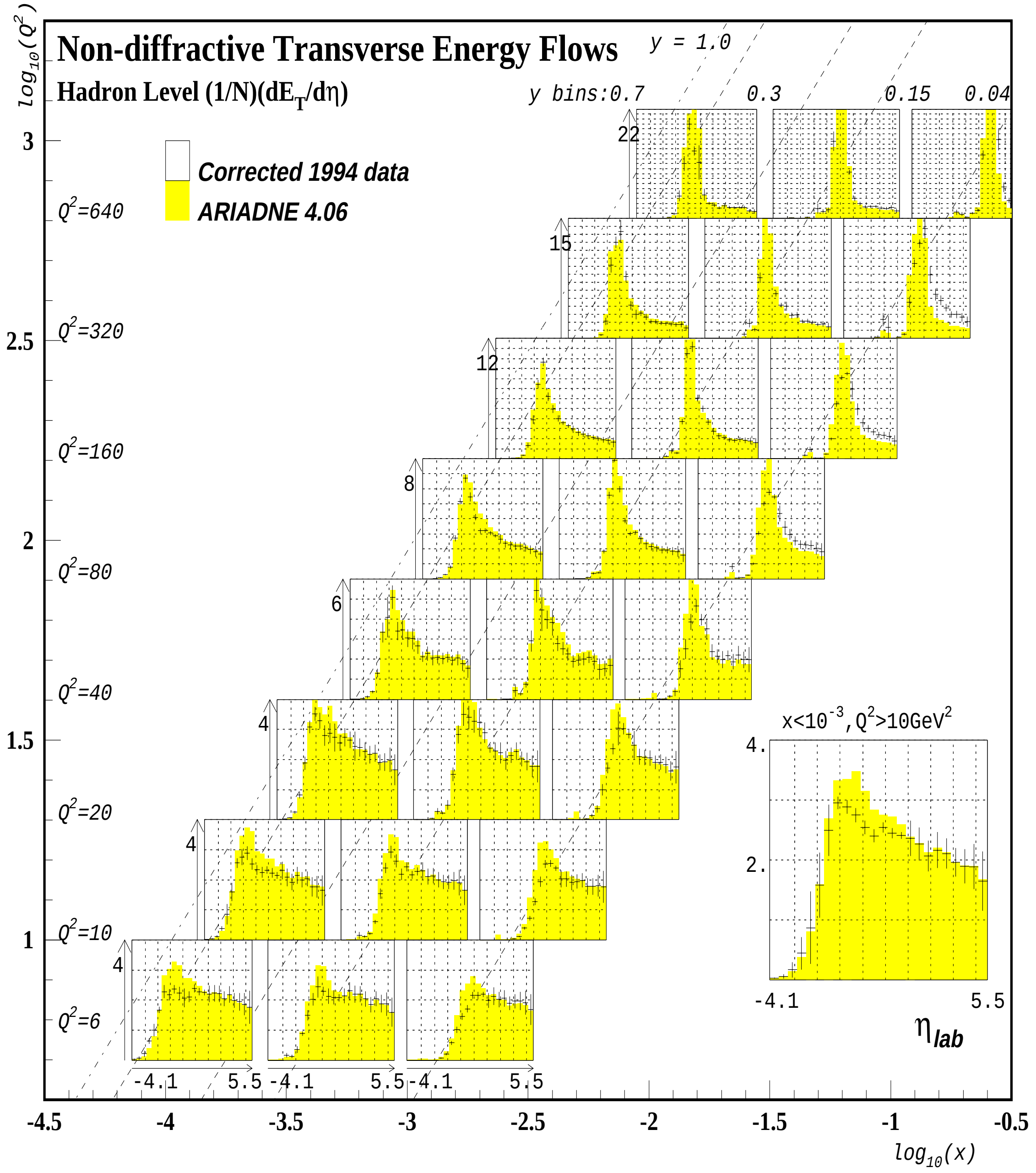

Figure 5.8: *1994 data versus the* ARIADNE 4.06 *prediction. The lower right-hand plot is the kinematic bin used in the 1993 analysis.*

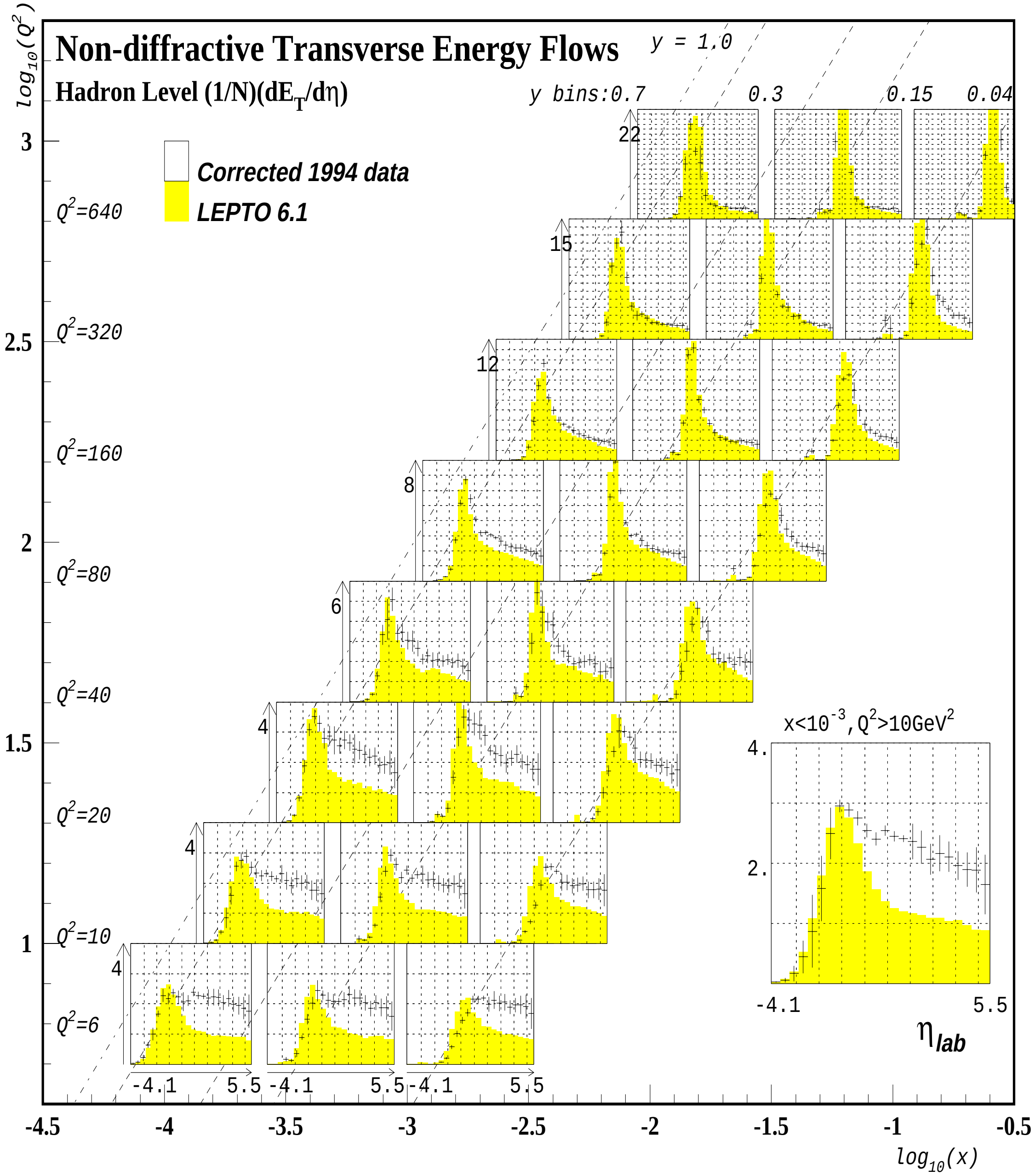

Figure 5.9: *1994 data versus the* LEPTO 6.1 *prediction.*

5.4 Comparison of 1993 and 1994 results

As a useful check, a subset of the 1994 analysis is equivalent to the kinematic and angular region of the 1993 analysis. Figure 5.10 shows the stability of the transverse energy flow measurement taken from the two different years' running periods. The two flows are in good agreement in the forward region even though the event selection criteria are different for both. This indicates that the stability of the measurement of the E_T flows in the forward detector region.

The partonic level E_T flow calculated using BFKL dynamics is shown in the plot. No hadron level calculation is yet available. The effect on the level of the flow of the hadronization of the partons is not analytically calculable but most predictions estimate an increase in the level of the flow of around 400-500MeV [46]. This brings the BFKL prediction and our measurement into good agreement.

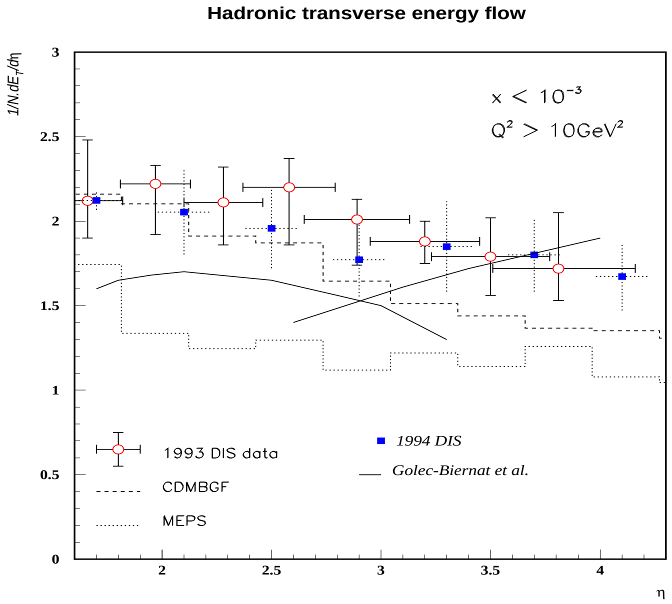

Figure 5.10: *Corrected 1993 and 1994 non-diffractive E_T flows in the 1993 kinematic bin. CDMBGF (*ARIADNE 4.03*) and MEPS (*LEPTO 6.1*) predictions are shown for comparison. Also shown is the parton-level E_T flow prediction from Golec-Biernat et al.[46]*

5.5 Energy flows versus x

One of the predictions of BFKL dynamics is a rising transverse energy flow in the γ^*p central region with decreasing x_{bj} [46]. Conventional dynamics predicts a falling flow with decreasing x_{bj} as can be seen later in figure 5.11. We can extract, for small fixed ranges of Q^2, a transverse energy flow versus x plot. The three y-bins in each Q^2 interval in the 1994 analysis are equivalent to having three x-bins.

To compare the transverse energy flow level in the central region for each of these bins requires a boost to the hadronic centre of mass system (HCM). Each individual hadron should be boosted. However, since the multiplicity of hadrons cannot be measured in the far-forward region due to the degradation of angular resolution, an accurate boost of hadrons cannot be achieved.

However, at low values of Q^2, the transverse component of the boost can be neglected (within errors) and a suitable approximation can be made by a purely longitudinal boost. By neglecting the hadron masses, this is equivalent to a simple translation of the pseudorapidity axis [48]. This translation is made using

$$\Delta\eta(=\eta_{hcm}-\eta_{lab}) \approx \frac{1}{2}\ln\left(\frac{4xE_p^2}{Q^2}\right) \tag{5.2}$$

Which further simplifies, at low-x, to a dependency on y alone.

Mean y	$\eta_{lab}(\eta_{hcm}=0)$
0.08	≈ 3.0
0.21	≈ 2.5
0.42	≈ 2.1

Taking all 9 of the x-bins in the lowest 3 Q^2 intervals, the boost translations are calculated. The transverse energy flow at $\eta_{hcm}=0$ is extracted from the laboratory frame measurements and displayed in figure 5.11.

The pseudorapidity interval between the proton remnant and the current jet is $\approx (\ln W)$ in the QPM from equation 5.2. As y $(\propto W^2)$ decreases, the width of this central region decreases. The contribution of energy associated with the current jet but measured at $\eta_{hcm}=0$ will become more significant in the measurement of transverse energy flow in the central region at low y. Due to this effect, at lower x the measurement may be artificially high and not, for example, a signature of BFKL dynamics.

To determine whether this is the case, a measurement is made further away from the current jet. The acceptance of the detector is $\approx 40\%$ at $\eta = 4.2$. This allows us to measure the transverse energy flow in all y bins at $\eta_{hcm} = 1.2$. The result of this measurement is shown in figure 5.12. No significant difference in the shape of the two distributions can be seen.

The errors displayed on the plots are statistical (bars) and full systematics (lines). There is certainly some correlation between the systematic error on these points, e.g. an event selection cut can affect all the points in the same way. The quantative correlation has not been calculated since the boost to the hadronic centre of mass system will be much more effective using information obtained with the **FDET** (after the 1995 running period).

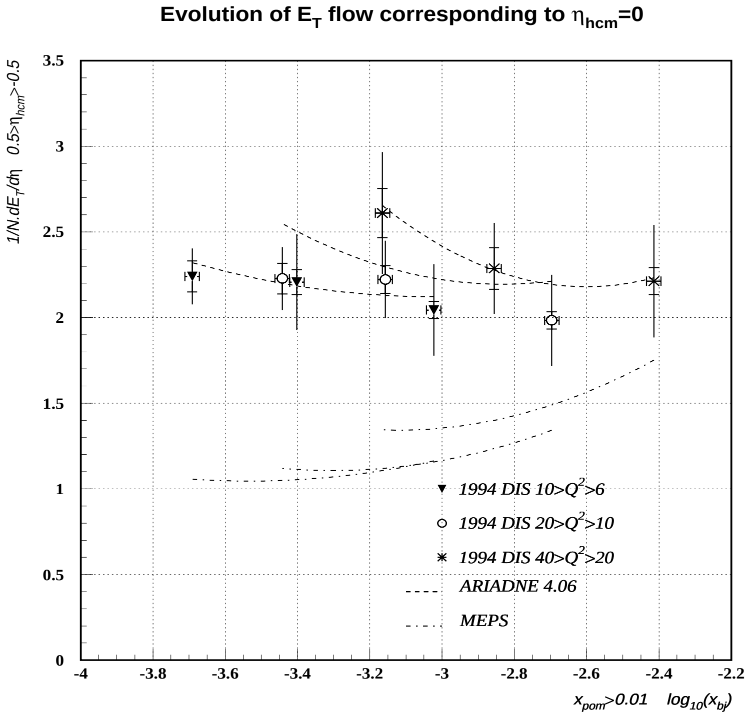

Figure 5.11: *Evolution in* x_{bj} *of the non-diffractive transverse energy flow at* $-0.5 < \eta_{hcm} < +0.5$

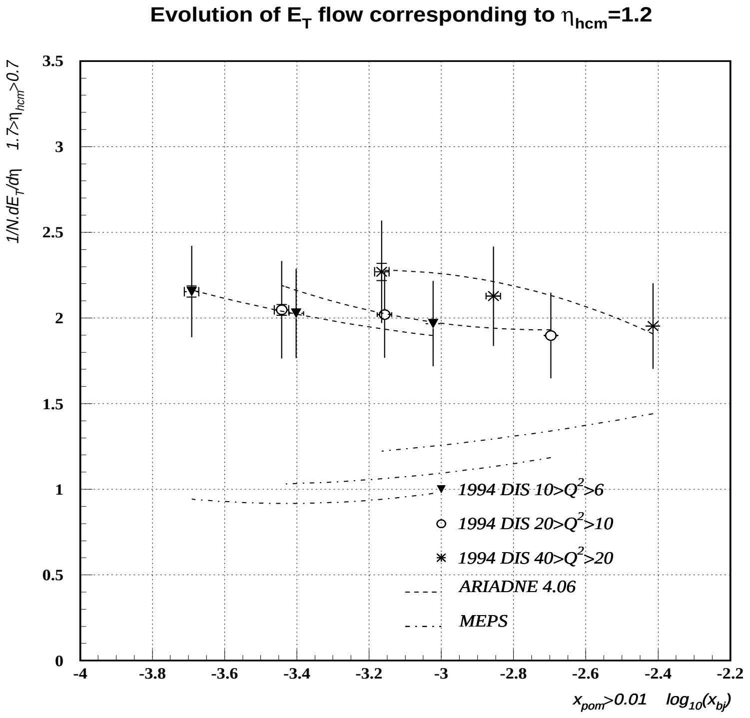

Figure 5.12: *Evolution in* x_{bj} *of the non-diffractive transverse energy flow at* $+0.7 < \eta_{hcm} < +1.7$

Chapter 6

Altering the conventional model

It is clear that the MEPS model as simulated by LEPTO6.1, which explicitly uses conventional (DGLAP) dynamics to describe all stages of the partonic DIS process, does not describe the transverse energy flows found in **ZEUS**. This does not in itself imply the presence of BFKL dynamics.

The MEPS model has been simulated by the default version of LEPTO6.1 with the exception of the default value of y_{cut}. This has recently been updated, from experimental results from jet rate studies, to $y_{cut} = 0.005$ from the earlier default $y_{cut} = 0.015$. Fragmentation and hadronisation in the predictions of the MEPS model have used the default settings of the JETSET7.4 simulation program. Are there parameters which can be altered to make the model describe the data?

There are many parameters to both LEPTO and JETSET which the user can freely change. LEPTO parameters affect purely partonic processes whilst JETSET parameters affect the hadronisation process. Although not an exhaustive list, the following alterations have been made to either LEPTO or JETSET to try to reproduce the level and shape of the E_T flow measured in the data:

- The variable y_{cut} determines how soft parton emissions become before the matrix element calculations give way to the approximate parton shower model. The LEPTO parameter PARL(8) redefines the value of y_{cut}. A lowering of this parameter to $y_{cut} = 0.0001$, seen in figure 6.1, has a dramatic effect on the level of transverse energy flow in the $\gamma^* p$ central region. By lowering y_{cut}, the hard scattering amplitude is calculated to lower values of parton emission energy than the default (more ME, less PS). Although this alteration may not be physically motivated, it is interesting to note the sensitivity of the E_T flow to the parameter.

- The default scheme for fragmentation implemented by JETSET7.4 is the Lund string fragmentation model. The JETSET parameter MSTJ(1)=1 invokes this scheme.

  Another interesting fragmentation model, although one not widely used nowadays, is one developed by Field and Feynman called *independent* fragmentation [60]. This is used by JETSET when MSJT(1)=2. The effect of this is shown in figure 6.2 where it is clear that independent fragmentation gives a worse description of the data than the string model.

- The longitudinal fragmentation function describes how large a fraction of the energy available is taken by a newly-created hadron. Its form can be chosen independently of the fragmentation scheme and is defined in terms of z. If, for example, a $q\bar{q}$ pair is considered to separate in the $+z$ and $-z$ directions along a straight line, the z variable is selected as the fraction of the $E + p_z$ taken by the created hadron from the $E + p_z$ available.

  By default, JETSET uses the Lund symmetric longitudinal fragmentation function. Default parameters give the function the form

  $$f(z) \propto \frac{1}{z}(1-z)^{0.5} \exp\left(\frac{-0.9m_{\perp}^2}{z}\right) \tag{6.1}$$

  A number of other functions are available by altering JETSET parameters, namely MSTJ(11) and PARJ(51-59). After making a selection of mainly arbitrary changes, on function in particular gives an enhanced transverse energy flow level in the $\gamma^* p$ central region. I have termed it *custom* fragmentation and it has the form

  $$f(z) = (1-z)^{1.8} \tag{6.2}$$

  which can be seen in figure 6.1. Although, again, this alteration may not be physically motivated, the sensitivity E_T flow to the form of longitudinal fragmentation function is an interesting observation.

- A less arbitrary approach to the alteration of longitudinal fragmentation function is found from looking at the limits placed on the functions by other HEP experiments. Results from measurements designed to place such limits are shown in figure 6.3. These come from TASSO[66], L3[67], DELPHI[65], OPAL in 1990[68] and two different forms of function from OPAL in 1994[69]. The details of the parameter changes are discussed in the references.

  Compared to the arbitrary function mentioned above, there is much more constraint on the range of level of the E_T flow level. This range indicates a sensitivity of E_T flow level in the $\gamma^* p$ central region on the longitudinal fragmentation function to a few hundred MeV.

- The LEPTO parameter PARL(3) (default=0.44GeV) gives the width, σ, of the Gaussian of transverse momenta of the primordial partons within the proton. The parameter PARL(14) (default=0.44GeV) gives the width, σ, of the Gaussian of transverse momenta when the non-trivial target remnant is split into a particle and a jet. An increase of both of these parameters to 2.0GeV and a decrease to 0.1GeV results in no noticeable difference in the shape and level of the E_T flow seen.

- Parton showering can be turned off using the LEPTO parameter LST(8)=2. This results in a suppression of the E_T flow level at all angles.

- The QCD corrections to the QPM can be switched off using LEPTO parameter LST(8)=0. This results in a large suppression in the level of the E_T flow in the $\gamma^* p$ central region and an enhancement of the level of the current jet peak i.e. less descriptive of the data.

- The inclusion of electromagnetic and weak corrections to the Born cross section is made with the default setting of the LEPTO parameter LPARIN(2)=1. Turning off these corrections (LPARIN(2)=0) has no noticeable effect on the shape or level of the E_T flow.

- The default parton density function used for the MEPS simulation is the MRSA[57] scheme. Changing this to MRSD$^-$[58] has no noticeable effect on the shape or level of the E_T flow.

- The JETSET parameter MSTJ(13) gives E_T to endpoint quarks in a single jet system. The default value is 0 and any change up to 1GeV has no noticeable effect on the shape or level of the E_T flow.

- The inclusion of the calculation of Bose-Einstein effects is not made in the default version of JETSET (MSTJ(51)=0). An inclusion of these effects has no noticeable effect on the shape or level of the E_T flow.

- The JETSET parameter PARJ(33) is used, together with the quark masses, to define the remaining energy below which the fragmentation of a jet system is stopped and the final two hadrons are formed. The default value of 0.8GeV is lowered to 0.15GeV but this has no noticeable effect on the shape or level of the E_T flow.

- An invariant mass cutoff m_{min} of parton showers, below which partons are assumed not to radiate further partons, is altered by the JETSET parameter PARJ(82) (in conjunction with PARJ(81) and MSTJ(44)). The default value of 1GeV is lowered to 0.6GeV with no noticeable effect on the shape or level of the E_T flow.

- The JETSET parameter MSTJ(49) allows the user to select probabilities of branchings in parton emission which are not inspired by conventional QCD (the default). A scalar gluon toy model is selected for comparison (MSTJ(49)=1). This suppresses the E_T flow in the $\gamma^* p$ central region by a few hundred MeV i.e. even lower than the level measured in the data.

- The branching mode for time-like showers is selectable in JETSET parameter MSTJ(42). The default mode, MSTJ(42)=2, uses coherent branching which is explicitly angular ordered. By changing MSTJ(42) to 1, the conventional branching mode is used which does not use angular ordering in the parton emission. No noticeable effect on the shape or level of the resulting E_T flow is seen.

- An override of the normal Q^2 definition is provided by JETSET parameter MSTP(22). This is used to obtain the maximum of parton shower evolution. No available change to this definition results in a noticeable change in the shape or level of the E_T flow.

- The parameter PARP(62) (default = 1.0GeV) defines in JETSET an effective cut-off Q or k_T value, below which space-like partons are not evolved. A lowering of this parameter to 0.44GeV has no noticeable effect on the shape or level of the resultant E_T flow.

- The width, σ, of the p_x and p_y transverse momenta distribution for primary hadrons can be selected with PARJ(21) of JETSET. The default value of 0.36GeV is increased to 2.0GeV with no noticeable effect on the shape or level of the resultant E_T flow.

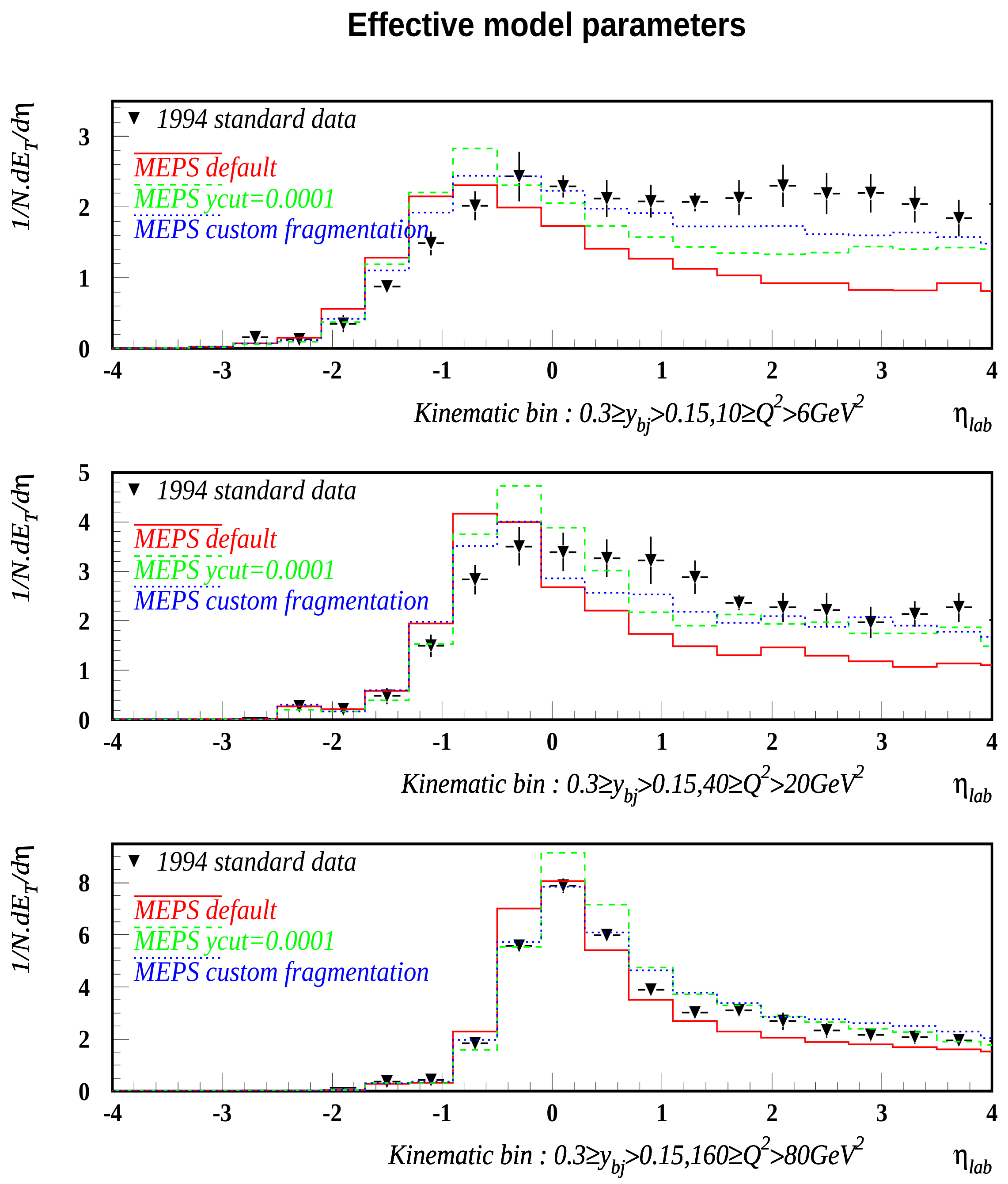

Figure 6.1: *The effect on the transverse energy flow of changing* y_{cut} *and the longitudinal fragmentation function to the function described in the text. The non-diffractive 1994* E_T *flows are shown for comparison.*

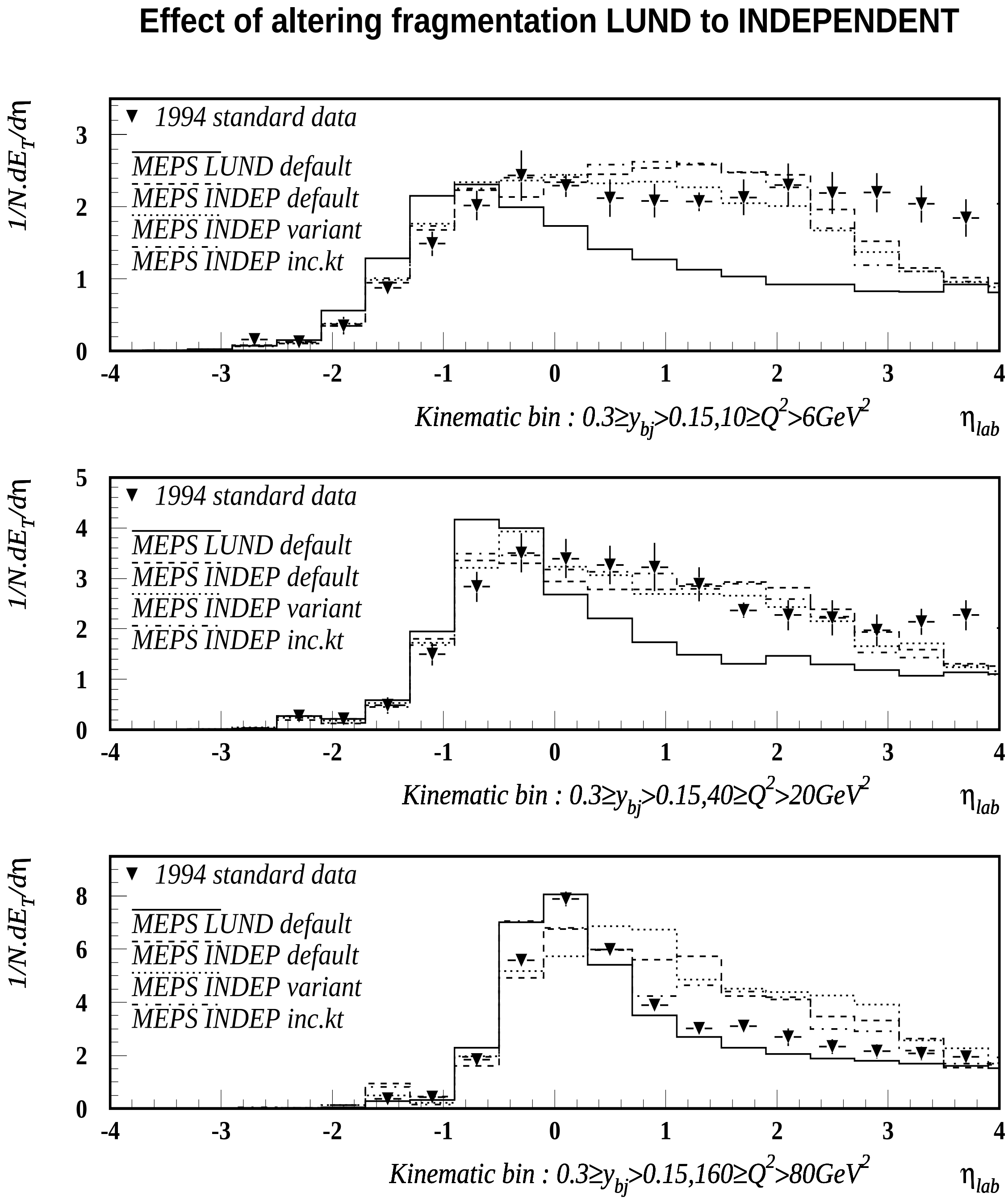

Figure 6.2: *The effect on the E_T flow of altering the default Lund string fragmentation scheme to independent fragmentation. Two variants of independent fragmentation are shown, one with a variation of gluon jet fragmentation "INDEP variant" and the other with increased gluon jet k_T "INDEP inc.kt". The non-diffractive 1994 E_T flows are shown for comparison.*

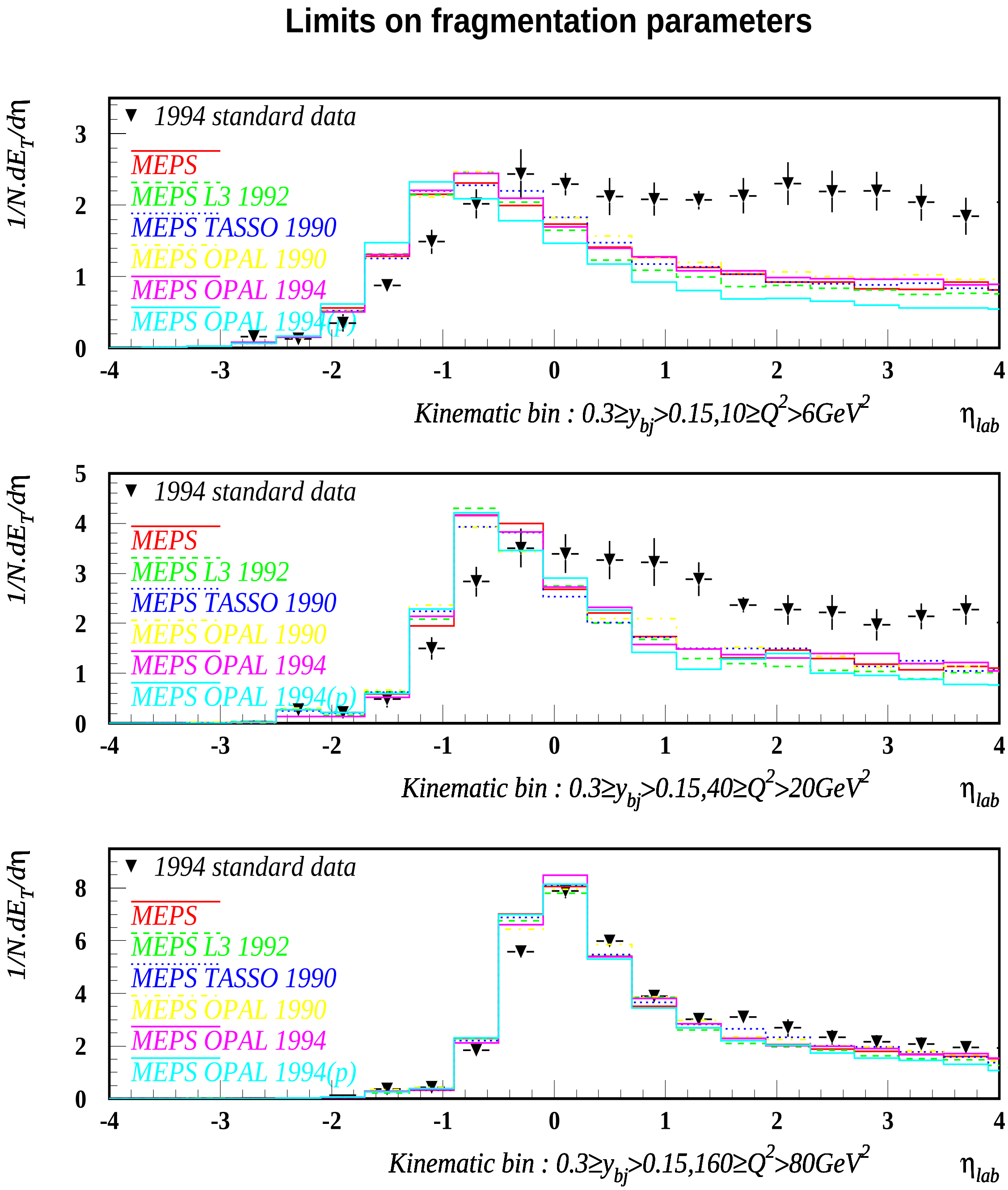

Figure 6.3: E_T *flows from various limits set on the parameters of the Lund symmetric longitudinal fragmentation function. (OPAL1994(p) uses the Petersen fragmentation function [64]). The default* LEPTO6.1 *(MEPS default) and non-diffractive 1994* E_T *flows are shown for comparison.*

Chapter 7

Conclusions

The transverse energy flows from deep inelastic scattering events collected by **ZEUS** in the 1993 and 1994 running periods have been measured by correcting **ZEUS** calorimeter cell energies back to hadronic final state particles.

Similar event selection procedures were adopted for both years' data; the main exception being that in 1994 the addition of the SRTD component enabled more accurate event reconstruction.

For the analysis of the event data collected in 1993, an η_{max} cut was placed on events to allow only non-diffractive DIS events to pass through the analysis. For those events collected in 1994, an $x_{\mathcal{P}}$ (roughly proportional to η_{max}) cut was placed on events to separate and independently analyse diffractive DIS events.

In the kinematic range $x_{bj} < 10^{-3}, Q^2 > 10\mathrm{GeV}^2$, up to the **HERA** kinematic limit, the transverse energy flows in the $\gamma^* p$ frame central region transform to the very forward region of the **ZEUS** detector. The errors on the measurement of calorimeter cell energies in this region have never been well-understood until now. It is found that the main sources of these errors are caused firstly by the inadequate description of this part of the detector in the Monte Carlo simulation and, secondly, the large disparity between the predictions of the two physics generators which are used to correct back the cell energies to the hadronic final state. Both of these error sources independently contribute approximately 10% to the overall error which is in the region of 15%.

The transverse energy flow in the $\gamma^* p$ central region in this kinematic range is flat (or slightly sloping in the proton direction) at a level of $\approx 2\mathrm{GeV}/\mathrm{unit}$ of rapidity. This level is well-described by the colour dipole model (CDM) whereas the matrix element parton shower model (MEPS) predicts too-little E_T flow by as much as 1GeV/unit of rapidity.

Looking at a large part of the kinematic range available at **HERA** with the events collected in 1994 the following conclusions can be drawn:

- The level of the E_T flow found in data in the $\gamma^* p$ central region in all kinematic ranges is predicted by the CDM. The MEPS model fails to predict this level at lower values of Q^2.
- Both of the models fail to predict the level and shape of the E_T flow in the *current* region at low Q^2 and low x_{bj} (high W). The "peaked" shape of the current jet E_T flow predicted by the models is not reproduced in the data.
- In the $\gamma^* p$ centre of mass system, the average E_T flow level per unit of rapidity is flat or seems to rise slightly as x_{bj} decreases. However, this rise cannot be confirmed using the currently available measurement since the systematic errors encountered are presently far too high. A fuller understanding of **ZEUS** in the Monte Carlo in the future should reduce these errors.

  The CDM predicts this rising trend in the data fairly well whereas the MEPS model predicts the opposite: a slight fall in E_T flow level as x_{bj} decreases.
- The current default version of the HERWIG physics generator, used for comparison purposes in this thesis, fails to predict the shape and flow of E_T found in the data, especially at low Q^2 and low x_{bj}.
- *None of the models in their default form completely describes the measured transverse energy flow throughout phase-space.*

There are many different parameters which govern the generation of events by the MEPS model. The testing of the sensitivity of the E_T flow to alterations in these parameters ascertains the predictivity and stability of the model. Importantly, since the MEPS model explicitly uses the conventional DGLAP approach to parton evolution at every stage of generation, the alteration of these parameters indicates how close the prediction of this approach can be to the result found from the data.

Although not all of these parameters were changed, all of those which were considered as having a possible effect on the level of the E_T flow were independently altered. Only two of these parameter changes had any significant effect in making the E_T flow level rise.

1. The first is the reduction of the y_{cut} which increases the component of the matrix element calculation with respect to the parton shower approximation in the overall calculation. Since the change of this parameter is roughly 2 orders of magnitude for the resulting E_T flow to rise significantly, it is likely that the change has no theoretical justification.

2. The second is the alteration of the fragmentation parameters which, of course, would also affect the hadronisation of the CDM particles if altered in that generator. The uncertainties in the level of E_T flow resulting from "reasonable" changes in the fragmentation parameters are 200-300MeV. A rather more drastic change of parameters and type of fragmentation function result in uncertainties of 1GeV and more. Although, again, this sort of alteration may not be theoretically justified when considering consistency with other measurements, the nature and dynamics of the hadronisation process are, at present, very poorly understood. The theoretical objections to changing the hadronisation process are much less well-defined.

The MEPS model cannot, for the most part, be made to reproduce the E_T flow shape and level found in the data without rather extreme parameter changes being made. In addtion, the CDM *does* reproduce the level of the E_T flow in the data in the $\gamma^* p$ central region; this model does not explicitly use conventional dynamics to evolve partons.

However, because of the uncertainties of the fragmentation process and because there is no definite answer to the question of whether the CDM exhibits BFKL-like behaviour, the effect of BFKL dynamics in parton evolution has not yet been conclusively seen at **ZEUS** even though there exists some circumstantial evidence for its presence.

Bibliography

[1] K. Piotrzkowski and M. Zachara, ZEUS-Note-94-167.

[2] K. Piotrzkowski and M. Zachara, ZEUS-Note-95-138.
"Determination of the ZEUS Luminosity in 1994"

[3] ZEUS secretariat, Author list 23.01.95. presented at
the beginning of all ZEUS papers.

[4] ZEUS Collab., "ZEUS, A detector for HERA", PRC 87-02, September 1987

[5] ZEUS Collab., Uwe Holm edt., "ZEUS - A detector for HERA. Status report 1993", February 1993

[6] F.Bruyant, M.Marie, R.Brun, F.Carena, F.G.deBilio, G.Tromba, G.N.Patrick, J.Allison, P.Zanarini, S.Giani, F.Carminati, W.Gebel, A.C.McPherson, T.Baroncelli, M.Hansroul, K.Lassila, A.Ferrari, P.Bregnant, H.C.Feserfeldt, D.Ward, J.J.Durmont, H.Boerner, W.Mitaroff, R.Hemingway, L.Urban, GEANT3.15 suite of programs, 27/01/93, CERN program library AAAA001

[7] N. Dyce, K. Long, J. Shulman, "The CTD Reconstruction Program User's Guide", ZEUS 94-011, February 1994.

[8] S. Schlenstedt. Documentation included in the ZEUS offline library routine PHANTOM. Version January 1994.

[9] W. Dorth, "LAZE, Logical Access to ZEUS events", ZEUS 91-069, 20/6/91

[10] A. Jamdagni, Imperial College London. Private communication.

[11] T. Jones, University College London. Private communication.

[12] K. Long, Imperial College London. Private communication.

[13] N. Harnew et al., “The Technique of z Coordinate Determination using a Time Difference Measurement for the ZEUS Central Tracking Detector”, ZEUS 89-038, 30/3/89

[14] J. del Peso and E. Ros, “Fast Simulation of Electromagnetic Showers in the ZEUS Calorimeter”, DESY 91-005. February 1991.

[15] T. Tymieniecka, “On Neutrons in Uranium- Scintillator Calorimeters”, DESY 91-012. March 1991.

[16] The ZEUS Calorimeter Group, “Response of a Uranium-Scintillator Calorimeter to Electrons, Pions and Protons in the Momentum Range 0.5-10 GeV/c”, DESY 89-149, November 1989.

[17] U. Behrens et al., “Calibration of the Forward and Rear ZEUS Calorimeter using Cosmic Ray Muons.”, DESY 93-121, August 1993.

[18] The ZEUS Calorimeter Group, “Test of the ZEUS Forward Calorimeter Prototype”, DESY 89-128, October 1989.

[19] The ZEUS Luminosity Group, “First Measurements of HERA Luminosity by ZEUS Lumi Monitor”, DESY 92-066, May 1992.

[20] The ZEUS Data Acquisition Group, “ZEUS Contributions to the Real-Time 93 Conference”, Vancouver, Canada. DESY 93-091, July 1993.

[21] R. Brun, Zebra4, CERN (1987)

[22] S. Fisher & P. Palazzi, The ADAMO data system, RAL (1990)

[23] HERA workshop, ed.W. Buckmuller& G. Ingelman; “Physics at HERA”.(October 29-30,1991)

[24] H. Abramowicz,A. Caldwell,R. Sinkus, “Neural Network Based Electron Identification in the ZEUS Calorimeter” DESY 95-054 (March 1995).

[25] M. Lancaster, Proceedings of the Durham Workshop on Proton, Photon and Pomeron structure (Sep 1995), to be published in Journal Phys.G.

[26] A. Caldwell. Documentation included in the ZEUS offline library routine PHANTOM. Version3.2 10/1/93.

[27] G. Wolf. "Deep Inelastic Structure Functions from HERA", DESY 94-178 (October 1994).

[28] H. Abramowicz. Documentation included in the ZEUS offline library routine PHANTOM. Version 21/1/93.

[29] P. Kaziewicz, M. Lancaster, "The Tracking Vertex Distribution of the ZEUS 93 data", ZEUS 93-127. 14/1/93.

[30] J. Ng, W. Verkerke, "An Overview of SRTD Analysis", ZEUS 95-037. 31/7/95.

[31] L. Koepke, "The ZEUS Primer", ZEUS collab., August 1994.

[32] N. Brook, University of Glasgow. Information contained in private FORTRAN program routine "ALLSTUD" and private communication. 05/95

[33] M. Virchaux, DAPNIA/SPP,C.E.Saclay,F-91191 Gif-sur-Yvette,France; "Nucleon Structure Functions"

[34] V. N. Gribov, L. N. Lipatov, Sov.J.Nucl.Phys. 15 (1972) 78

[35] G. Ingelman, "LEPTO version 6.1"; Proc. "Physics at HERA" Vol 3, p.1366; DESY, Hamburg 1992

[36] S. L. Adler,W. A. Bardeen, Phys.Rev. 182 (1969) 1517

[37] L. Lönnblad, DESY, Hamburg, "Ariadne Version 4. A Program for Simulation of QCD- Cascades Implementing the Colour Dipole Model"; DESY 92-046, February 1992.

[38] ZEUS Collab., M. Derrick et al., "Measurement of the Proton Structure Function F2 from the 1993 HERA data", DESY 94-143 (August 1994), acc. by Z. Physik;
ZEUS Collab., M. Derrick et al., "Measurement of the Proton Structure Function F2 in EP Scattering at HERA", Phys. Lett. B316 (1993).

[39] H1 Collab. I. Abt et al., “Measurement of the Proton Structure Function F2 in the low-x region at HERA”, Nucl. Phys. B407 (1993);
H1 Collab., T. Ahmed et al., “A Measurement of the Proton Structure Function F2”, DESY 95-006 (January 1995).

[40] ZEUS collab. M.Derrick et al., “Extraction of the gluon density of the proton at small x”, DESY 94-192 (October 1994)

[41] H1 collab. I.Abt et al., “The gluon density of the proton at low x from a QCD analysis of F_2”, DESY 95-081 (May 1995)

[42] F. Halzen, A. D. Martin, “Quarks and Leptons: An Introductory Course in Modern Particle Physics”; published by John Wiley and Sons, 1983

[43] E. A. Kuraev, L. N. Lipatov and V. S. Fadin, Sov. Phys. JETP45 (1977).

[44] A. J. Askew, J. Kwiecinski, A. D. Martin and P. J. Sutton, “Implications of Scaling Violations of F(2) at HERA for QCD”, Phys. Lett. B325 (1994).

[45] J. Kwiecinski, A. D. Martin, P. J. Sutton and K. Golec-Biernat, “QCD Predictions for the Transverse Energy Flow in Deep-Inelastic Scattering in the HERA small x regime”, Phys. Rev. D50 (1994).

[46] J. Kwiecinski, A. D. Martin, P. J. Sutton and K. Golec-Biernat, “Transverse Energy Flow at HERA”, Durham Preprint, DTP/94/30, May 1994; CERN Preprint HEP-PH-9405400.

[47] T. Sjöstrand, Theory division, CERN. “PYTHIA5.7 and JETSET7.4. Physics and manual.”; CERN-TH.7112/93. Revised August 1994.

[48] ZEUS Collab., M. Derrick et al., “Comparison of Energy Flows in Deep Inelastic Scattering With and Without a Large Rapidity Gap”, Phys. Lett. B338 (1994);
ZEUS Collab., M. Derrick et al., “Hadronic Energy Distributions in Deep Inelastic Scattering at HERA”, Z. Phys. C59 (1993).

[49] H1 Collab, I. Abt et al., “Energy Flow and Charged Particle Spectra in Deep Inelastic Scattering at HERA”, Z. Phys. C63 (1994).

[50] R. Schattevoy, ZEUS-Note-93-074 and Ph.D. thesis, Universität Bonn, 1994.

[51] Marc de Kamps, ZEUS-Note-94-014.

[52] ZEUS collab., M. Derrick et al., "Observation of Events with a Large Rapidity Gap in Deep Inelastic Scattering at HERA" ; DESY 93-093 (July 1993) Phys.Lett.B 315 (1993) 481-493

[53] ZEUS collaboration, "Measurement of the Diffractive Structure Function in Deep Inelastic Scattering at HERA"; DESY 95-093 (May 1995)

[54] A. Doyle, University of Glasgow. Private communication.

[55] T. Haas, DESY. Private communication.

[56] G.Marchesini, B.R.Webber, G.Abbiendi, I.G.Knowles, M.H.Seymour, and L.Stanco, Computer Physics Communications 67 (1992) 465.

[57] A.D.Martin, W.J.Stirling and R.G.Roberts, Durham Preprint DTP/94/34 (to be published in Phys.Rev.D50)

[58] A.D.Martin, W.J.Stirling and R.G.Roberts, Phys.Lett. B306(1993) 145.

[59] B.Andersson, G.Gustafson, B.Söderberg, Z.Phys. C20(1983) 317.

[60] R.D.Field, R.P.Feynman, Nucl.Phys. B136(1978) 1.

[61] G.Altarelli, G.Parisi, Nucl.Phys. B126(1977) 298.

[62] P.Bruni and G.Ingelman, DESY 93-187, "Proceedings of the Europhysics Conference on High Energy Physics", Marseille 1993, 595.

[63] N.N.Nikolaev and B.G.Zakharov, Z.Phys. C53(1992) 331; A.Solano, Ph.D. thesis, University of Torino (1993).

[64] C.Peterson, D.Schlatter, I.Schmitt and P.Zerwas, Phys.Rev. D27(1983) 1056.

[65] DELPHI collaboration, P.Aarnio et.al., "Study of Hadronic Decays of the Z0 Boson", Phys.Lett. B240(1990) 271, April 1990.

[66] TASSO collaboration, W.Braunschweig et.al., “Global jet properties at 14-44 GeV centre of mass energy in e+e- annihilation”, Z.Phys. C47(1990) 187, February 1990.

[67] L3 collaboration, B.Adeva et.al., “Studies of hadronic event structure and comparisons with QCD models at the Z0 resonance”, Z.Phys. C55(1992) 39, March 1992.

[68] OPAL collaboration, M.K.Akrawy et.al., “A Measurement of Global Event Shape Distributions in the Hadronic Decays of the Z0”, CERN preprint, CERN-EP/90-48, April 1990.

[69] OPAL collaboration,R.Akers et.al., “A Measurement of the Production of D*± Mesons on the Z0 resonance”, CERN preprint, CERN-PPE/94-217, December 1994.